Elastic and Proton-Dissociative ρ^0 Photoproduction at HERA

Dissertation

zur Erlangung des Doktorgrades
des Fachbereichs Physik
der Universität Hamburg

vorgelegt von

Kai Desler
aus Hamburg

Hamburg
Dezember 2000

Gutachter der Dissertation:	Prof. Dr. E. Lohrmann
	Prof. Dr. R. Klanner
Gutachter der Disputation:	Prof. Dr. E. Lohrmann
	Prof. Dr. G. Heinzelmann
Datum der Disputation:	22. Februar 2001
Dekan des Fachbereichs Physik und Vorsitzender des Promotionsausschusses:	Prof. Dr. F.-W. Büßer

Abstract

Elastic and proton-dissociative photoproduction of ρ^0 mesons has been studied in the reactions $\gamma p \to \rho^0 p$ and $\gamma p \to \rho^0 N$, where N is a proton-dissociative state. The average center of mass energy was 90 GeV. A set of scintillation counters was designed and installed close to the HERA beam pipe to detect the proton-dissociative state N in an angular range between 6 and 26 mrad in the outgoing proton direction. These counters allowed identification of proton-dissociative states N down to masses of about 1.5 GeV and the total measured mass range was $1.5 < M_N < 27$ GeV. The counters were also used to improve subtraction of proton-dissociative background from elastic ρ^0 photoproduction. The results are the following:

The differential cross section of elastic ρ^0 photoproduction, if fitted to an exponential function of the form $A\exp(-b_e|t| + c_e t^2)$, where t is the square of the four-momentum transfer at the proton vertex, yields the parameters $b_e = 11.7 \pm 0.3$ (stat.) $^{+1.8}_{-0.9}$ (syst.) GeV^{-2} and $c_e = 3.7 \pm 0.7$ (stat.) $^{+2.1}_{-0.2}$ (syst.) GeV^{-4}, in the fit range $0 < |t| < 0.5$ GeV^2. A fit to the proton-dissociative cross section in the same t-range to the form $A\exp(-b_i|t|)$ yields the slope $b_i = 4.3 \pm 0.2$ (stat.)$^{+0.7}_{-0.6}$ (syst.) GeV^{-2}. The proton-dissociative cross section has been measured in the interval $0 < |t| < 2$ GeV^2 and fitted to an exponential function of the form $A\exp(-b_i|t| + c_i t^2)$. The result is $b_i = 4.7 \pm 0.2$ (stat.) GeV^{-2} and $c_i = 1.0 \pm 0.1$ (stat.) GeV^{-4}. The ratio of the elastic to the proton-dissociative cross section in the range $0 < |t| < 0.5$ GeV^2 is 2.2 ± 0.1 (stat.) $^{+0.4}_{-0.1}$ (syst.), and in the whole t-range this ratio is 2.0 ± 0.1 (stat.) $^{+0.4}_{-0.1}$ (syst.). Using the published elastic ρ^0 cross section of 11.2 μb at a center of mass energy of 71.7 GeV, this leads to a total cross section of the proton-dissociative reaction at 90 GeV center of mass energy of $\sigma_{\rm pdiss} = 6.0 \pm 0.4$ (stat.) $^{+0.7}_{-1.3}$ (syst.) μb.

The data have been compared with elastic and proton-dissociative reactions of protons and antiprotons at high energies at the ISR and the proton-antiproton storage ring at CERN and at the TEVATRON at Fermilab. Factorization of diffractive reactions has been tested and a fair agreement was found.

Zusammenfassung

Es wurde die elastische und Proton-dissoziative Photoproduktion von ρ^0–Mesonen in den Reaktionen $\gamma p \to \rho^0 p$ und $\gamma p \to \rho^0 N$ untersucht, wobei N einen Proton-dissoziativen Zustand bezeichnet. Die mittlere Schwerpunktsenergie war 90 GeV. Szintillationszähler wurden konstruiert und in der Nähe des Strahlrohrs aufgestellt, um den Proton-dissoziativen Zustand N in einem Winkelbereich von 6 bis 26 mrad in Richtung des auslaufenden Protons nachzuweisen. Diese Zähler ermöglichen den Nachweis des Proton-dissoziativen Zustands N hinab zu Massen von etwa 1.5 GeV und in dem Massenbereich $1.5 < M_N < 27$ GeV. Außerdem dienten die Zähler dazu, die Messung der elastischen ρ^0–Photoproduktion zu verbessern. Die Ergebnisse sind die folgenden:

Der differentielle Wirkungsquerschnitt der elastischen ρ^0–Photoproduktion, angepaßt durch eine Funktion der Form $A\exp(-b_e|t| + c_e t^2)$, wobei t das Quadrat des Viererimpulsübertrags am Protonvertex ist, ergibt im Bereich $0 < |t| < 0.5$ GeV^2 die Fitparameter $b_e = 11.7 \pm 0.3\,(\text{stat.})\,^{+1.8}_{-0.9}\,(\text{syst.})$ GeV^{-2} und $c_e = 3.7 \pm 0.7\,(\text{stat.})\,^{+2.1}_{-0.2}\,(\text{syst.})$ GeV^{-4}. Die Anpassung einer Funktion $A\exp(-b_i|t|)$ an den differentiellen Proton-dissoziativen Wirkungsquerschnitt im gleichen t-Intervall ergibt die Steigung $b_i = 4.3 \pm 0.2$ (stat.)$^{+0.7}_{-0.6}$ (syst.) GeV^{-2}. Der Proton-dissoziative Wirkungsquerschnitt wurde außerdem im Bereich $0 < |t| < 2$ GeV^2 gemessen und durch eine Exponentialfunktion der Form $A\exp(-b_i|t| + c_i t^2)$ angepaßt. Das Ergebnis ist $b_i = 4.7 \pm 0.2$ (stat.) GeV^{-2} und $c_i = 1.0 \pm 0.1\,(\text{stat.})$ GeV^{-4}. Das Verhältnis zwischen elastischem und Proton-dissoziativem Wirkungsquerschnitt im Bereich $0 < |t| < 0.5$ GeV^2 ist 2.2 ± 0.1 (stat.) $^{+0.4}_{-0.1}$ (syst.), und im gesamten t-Bereich ist das Verhältnis 2.0 ± 0.1 (stat.) $^{+0.4}_{-0.1}$ (syst.). Dieses Ergebnis führt, unter Verwendung des veröffentlichten elastischen Wirkungsquerschnittes von 11.2 μb bei 71.7 GeV, zum totalen Wirkungsquerschnitt der Proton-dissoziativen Reaktion bei 90 GeV von $\sigma_{\text{pdiss}} = 6.0 \pm 0.4$ (stat.) $^{+0.7}_{-1.3}$ (syst.) μb.

Die Ergebnisse wurden mit elastischen und Proton-dissoziativen Reaktionen mit Protonen und Antiprotonen verglichen, die mit dem ISR und dem Proton-Antiproton Speicherring am CERN und dem TEVATRON am Fermilab gewonnen wurden. Es wurde die Faktorisierung diffraktiver Reaktionen untersucht und eine zufriedenstellende Übereinstimmung gefunden.

Contents

List of Figures

List of Tables

Chapter 1

Introduction

The HERA[1] electron-proton collider at Deutsches Elektronen-Synchrotron (DESY) in Hamburg, Germany, is the only facility of its kind in the world. It was commissioned in 1992 together with the large particle detectors H1 and ZEUS. Originally designed to collide 30 GeV electrons on 820 GeV protons, a main purpose of HERA was to get more insight into the structure of the proton via deep inelastic scattering (DIS). At these reactions the virtuality Q^2 of the photon γ which mediates the interaction between the proton and the electron is very high. Typically, in DIS the proton breaks up and the signature of these events is characterized by hadron jets in the final state and an electron which is scattered under a large angle. An other physics topic which was intensively studied with the HERA experiments is photoproduction, where $Q^2 \simeq 0$, i. e. the exchanged photon is a quasi-real particle, and the electron is scattered under a very small angle. For this class of events HERA can be viewed as a unique γp collider.

Elastic photoproduction of ρ^0 mesons in the reaction $\gamma p \to \rho^0 p$ has been studied extensively in the past [4, 27, 32] and also during the last years at HERA energies [22, 44, 47, 48]. At the high center of mass energy provided by the HERA collider this reaction shows all the characteristics of a soft diffractive process, namely a weak energy dependence of the differential cross section, which is approximately of the form $d\sigma/d|t| \approx A \exp(-b|t|)$ at small $|t|$, where t is the squared four-momentum transfer between the photon and the ρ^0 meson, and A and b, a positive number, depend only weakly on the center of mass energy.

The vector meson dominance model (VMD) [6] has been quite successful in providing a good description of the photoproduction of vector mesons. It assumes that the

[1] Hadronen-Elektronen-Ringanlage

incoming photon can fluctuate during a short time t_f into a quark-antiquark ($q\overline{q}$) state before interacting with the proton: The physical photon $|\gamma\rangle$ can be seen as a superposition of a bare photon $|\gamma_B\rangle$ and an admixture of a hadronic component $\sqrt{\alpha}|h\rangle$:

$$|\gamma\rangle = \sqrt{Z_3}|\gamma_B\rangle + \sqrt{\alpha}|h\rangle, \tag{1.1}$$

where $\sqrt{Z_3}$ is introduced to normalize $|\gamma\rangle$. The quantum numbers of $|\gamma\rangle$ and $|h\rangle$ have to be identical. VMD assumes that the only contributions to $|h\rangle$ are given by the light vector mesons ρ^0, ω and ϕ and that the bare photon $|\gamma_B\rangle$ cannot interact with hadrons. A less restrictive model, the generalized vector dominance (GVD) model, assumes that other additional constituents contribute to $|h\rangle$. In the case of photoproduction, where the photon virtuality $Q^2 \simeq 0$, the fluctuation time is given by

$$t_f = \frac{2\nu}{Q^2 + M_V^2} \simeq \frac{2\nu}{M_V^2}, \tag{1.2}$$

where ν is the energy of the photon in the proton rest frame and M_V the mass of the $q\overline{q}$ state. The $q\overline{q}$ states have to have the quantum numbers of the photon, $J^{PC} = 1^{--}$. The lightest mass states with these quantum numbers are the light vector mesons ρ, ω and ϕ. In this model the vector meson V interacts with the proton and the reaction $\gamma p \to \rho^0 p$ represents then the elastic scattering $\rho^0 p \to \rho^0 p$. HERA, at a center of mass energy of about 100 GeV for the $\rho^0 p$ system, provides therefore a case of meson nucleon scattering at the highest center of mass energies observed so far.

In addition to the reactions studied with pp- and $p\bar{p}$-colliders, elastic ρ^0 photoproduction at HERA allows the study of elastic hadron-hadron cross sections at the highest energies, providing insight into their asymptotic behavior.

Since these processes show the characteristic slow dependence on center of mass energy, accurate measurements are required in order to check the theory. With the increased luminosity of HERA, statistical accuracy becomes less of a problem, and it is then essential to reduce systematic errors.

One of the largest systematic errors in previous analyses of elastic ρ^0 photoproduction [44, 48, 47] was a background of diffractive reactions where the incoming proton dissociates into a higher mass state N. Like the elastic reaction $\gamma p \to \rho^0 p$ the proton-dissociative (or inelastic) reaction $\gamma p \to \rho^0 N$ is characterized by a weak dependence on center of mass energy and a steep, approximately exponential dependence of the differential cross section on the four-momentum transfer squared, showing the characteristics of diffractive scattering. [21, 50] Another diffractive reaction is photon dissociation where the incoming photon dissociates into a higher mass state X. The

three diagrams in Fig. 1.1 show proton dissociation, $\gamma p \to \rho^0 N$ (a), photon dissociation, $\gamma p \to Xp$ (b) and double dissociation, $\gamma p \to XN$ (c). Of these three reactions only proton dissociation is a non-trivial background for elastic ρ^0 production and will therefore be studied in this analysis.

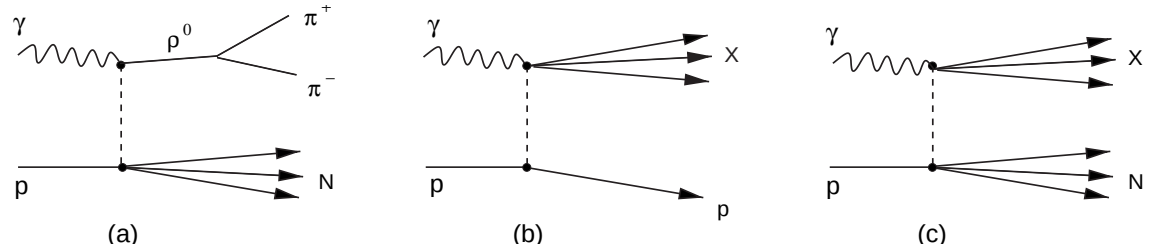

Figure 1.1: *Diffractive photoproduction reactions with proton dissociation, $\gamma p \to \rho^0 N$ (a), photon dissociation, $\gamma p \to Xp$ (b) and double dissociation, $\gamma p \to XN$ (c).*

The state N may escape detection, since the acceptance of the central ZEUS detector is limited: Though the solid angle coverage is 99.8% in the forward hemisphere, the ZEUS calorimeter does not detect particles emerging from the interaction point (IP) under polar angles $\theta < 2.5°$ and may therefore miss all particles from the state N. In such cases distinction between elastic and proton dissociative reactions becomes impossible.

To detect particles from diffractive reactions at very small angles we installed the Proton Remnant Tagger (PRT) in the ZEUS proton forward region. It consists of seven pairs of scintillation counters surrounding the beam line at two positions in the proton forward direction.

The PRT extends the angular acceptance of the ZEUS main detector in the forward region since particles can be detected down to polar angles angles $\theta = 1.5 - 26$ mrad, and can therefore detect proton dissociation with a large efficiency. Apart from being a background for elastic ρ^0 photoproduction, the proton dissociative reaction $\gamma p \to \rho^0 N$ is very interesting in its own right. Measurement of the slope of its differential cross section and of the ratio of elastic to proton diffractive cross section yields insight into proton diffraction, which is particularly interesting because of the high center of mass energy of HERA which is comparable to that of hadron colliders. A comparison with hadron-hadron collisions allows a test of factorization, predicted by the Pomeron exchange model of high energy diffraction.

This thesis is organized as follows: In chapter 2 an overview of the ZEUS detector and detailed description of the components relevant for this analysis is given. The physics of elastic and proton-dissociative ρ^0 photoproduction is discussed in chapter 3. chapter 4 describes the experimental procedure of this analysis, the trigger logic and the event selection cuts with emphasis on the identification of proton-dissociative events. The tagging efficiency of the Proton Remnant Tagger is determined in chapter 5 from physics data. In chapter 6 the combined acceptance of the ρ^0 trigger and the selection cuts is calculated with Monte Carlo simulations. In chapter 7 the systematic errors of the analysis are discussed and the results are presented. In chapter 8 the results of this analysis are compared with results obtained with the results of experiments with very high energetic protons and antiprotons at Fermilab and CERN.

Chapter 2

The ZEUS Detector

In this chapter a description of the experimental setup of the ZEUS detector is given, with emphasis on the components used in this analysis, namely the high resolution calorimeter (CAL), the Central Tracking Detector (CTD), the Photoproduction Tagger (PT), and the Proton Remnant Tagger (PRT).

The entire ZEUS detector has been described in detail elsewhere [25]. Throughout this thesis the right handed ZEUS coordinate system, shown in Fig. 2.1, will be used. The origin is at the nominal interaction point (IP) and the coordinate system is defined as follows: The z axis is given by the proton beam direction, the y axis points upwards and the x axis points horizontally to the center of HERA. The *azimuth angle* ϕ is measured with respect to the positive x axis. The *polar angle* θ is measured with respect to the positive z axis, consequently the polar angle of incoming protons is $\theta = 0°$, while the polar angle of the electron beam is $\theta = 180°$. Another useful variable is the *pseudo-rapidity* η which is defined as $\eta = -\ln(\tan(\theta/2))$. Particles scattered under 90° at the interaction point have pseudo-rapidity $\eta = 0$. The ZEUS coordinate can be split into two hemispheres with positive and negative pseudo-rapidity given by the proton and electron direction, respectively.

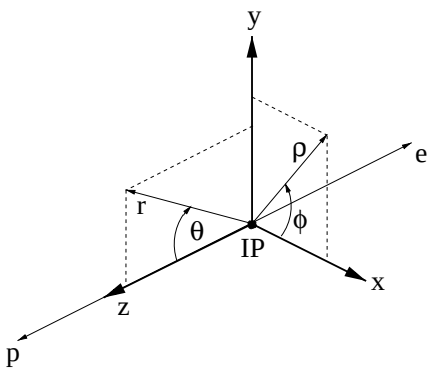

Figure 2.1: *The right handed ZEUS coordinate system.*

2.1 Overview

The ZEUS detector was commissioned in June 1992 and is operated since by about 450 physicists of 50 research institutes from 12 countries to study interactions between electrons[1] and protons at HERA.

Figs. 2.2 and 2.3 show sections of the detector along and perpendicular to the beam direction. The components of the inner detector are the following: The beam pipe is surrounded by a cylindrical multilayer wire chamber (CTD), and planar wire chambers in the forward (FTD) and rear (RTD) directions. The tracking chambers are situated inside a thin superconducting coil providing a magnetic field of 1.43 T that allows determination of particle charge and momentum. The inner detector is surrounded by the uranium-scintillator calorimeter (CAL) which absorbs high energetic particles and measures their energy. CAL consists of three main components, namely the forward (FCAL), barrel (BCAL) and rear (RCAL) calorimeter. A return path for the solenoid magnetic field flux is provided by the iron yoke which surrounds CAL and is instrumented with limited streamer tubes that measure energy leaking out of CAL, thus serving as a backing calorimeter (BAC). The momentum of muons is measured by limited streamer tubes inside and outside the barrel region of the yoke (BMUO), and in the forward direction by limited streamer tubes and drift chambers inside a toroidal magnetic field of 1.7 T.

2.2 The Calorimeter

The ZEUS calorimeter (CAL) is a sampling calorimeter consisting of depleted uranium ^{238}U tiles as absorbers and interleaved plastic scintillator (SCSN 38) which are read out by wavelength shifters and attached photomultipliers. The thickness of the two materials was chosen such that the calorimeter is *compensating*, i. e. the calorimeter response for electrons and hadrons of the same energy is equal. This is achieved by using 3.3 mm thick absorbers (one radiation length) and 2.6 mm thick scintillators. The relative energy resolution of CAL is under test beam conditions $\sigma(E)/E = 18\%/\sqrt{E} \oplus 1\%$ for electrons and $\sigma(E)/E = 35\%/\sqrt{E} \oplus 2\%$ for hadrons. The timing resolution of CAL is better than 1 ns for energy deposits above 4.5 GeV.

The FCAL and RCAL modules are rectangular shaped. The modules of BCAL are

[1] HERA was operated with positrons instead of electrons during the analyzed run period. However, the term *electron* will be used throughout this thesis.

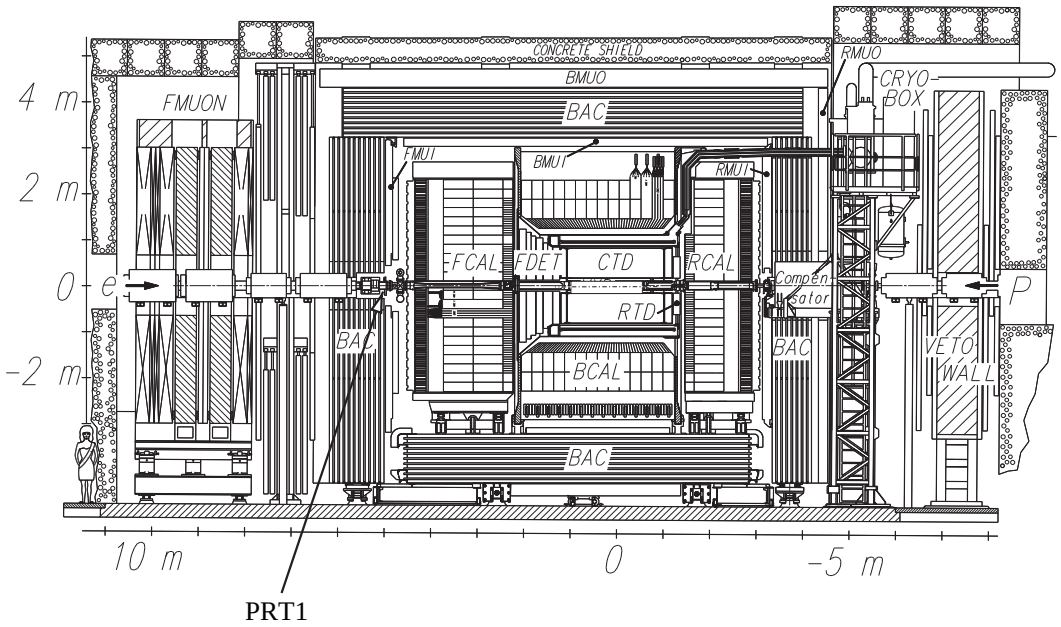

Figure 2.2: *Section of the ZEUS detector along the beam line.*

wedge-shaped to achieve the barrel shape of this calorimeter part. The solid angular coverage of CAL is 99.8% in the proton forward direction and 99.5% is the backward direction. The modules are segmented into electromagnetic (EMC) and hadronic (HAC) sections (see Fig. 2.2).

FCAL consists of 24 modules which cover the polar angular range $2.2° < \theta < 39.9°$. The modules are subdivided into towers with an area of 20×20 cm^2. The towers are longitudinally subdivided into an electromagnetic section (EMC) and two hadronic sections (HAC). The EMC section is vertically subdivided into four 20×5 cm^2 cells.

BCAL consists of 32 wedge-shaped modules which cover the polar angular range $36.7° < \theta < 129.1°$ and 360° in ϕ (see Fig. 2.3). The modules are subdivided into an EMC and a HAC section along the z-axis. The EMC and HAC sections consist of 53 and 14 towers, respectively.

RCAL, constructed similar to FCAL, consists of 24 modules which cover the polar angular range $128.1° < \theta < 176.5°$. RCAL towers consist of 20×10 cm^2 EMC cells and one HAC cell.

Each cell is read out via plastic wavelength shifters attached to the scintillators on both sides with a photomultiplier tube (PMT). In total 11836 CAL channels are being

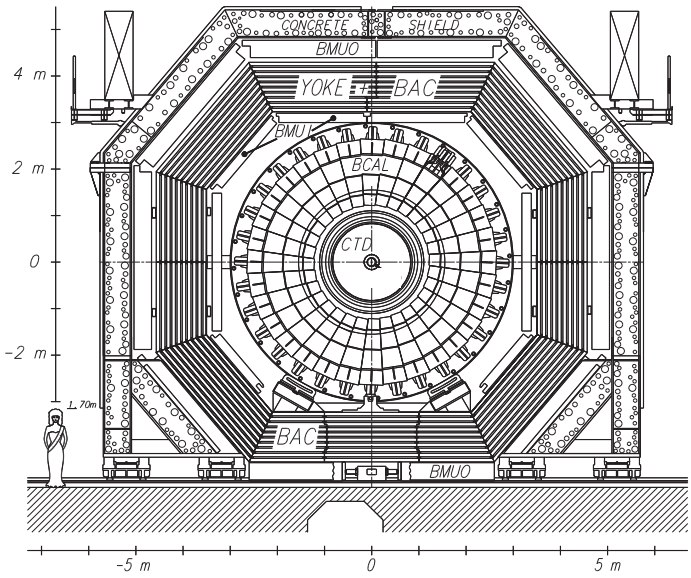

Figure 2.3: *Cross section of the ZEUS detector.*

read out.

The radioactivity of the depleted uranium provides an extremely stable reference signal used for calibration of the readout channels. The achieved precision of the calibration is better than 1%. In addition test pulses are used to check and calibrate the readout electronics. The performance of the photomultiplier tubes is monitored by LEDs and a laser system.

2.3 The Central Tracking Detector

Direction and momentum of charged particles are measured to a high precision with the central tracking detector (CTD). The CTD is a multi-cell stereo superlayer cylindrical drift chamber filled with a mixture of argon, CO_2 and ethane. The polar angular coverage of CTD is $15° < \theta < 164°$ while the full azimuthal angle ϕ is covered. In total CTD consists of 4608 sense wires and 24192 field wires organized in 9 super layers. A subset of the sense wires is equipped with a z-by-timing system which is used for trigger purposes. The spatial resolution of CTD in $r - \phi$ is about 230 μm for long

tracks, the momentum resolution is $\sigma_p/p = 0.005 \times p\,(\mathrm{GeV/c}) \oplus 0.0016$. The position of the interaction vertex can be measured by CTD with a typical resolution along (transverse to) the beam of 0.4 (0.1) cm.

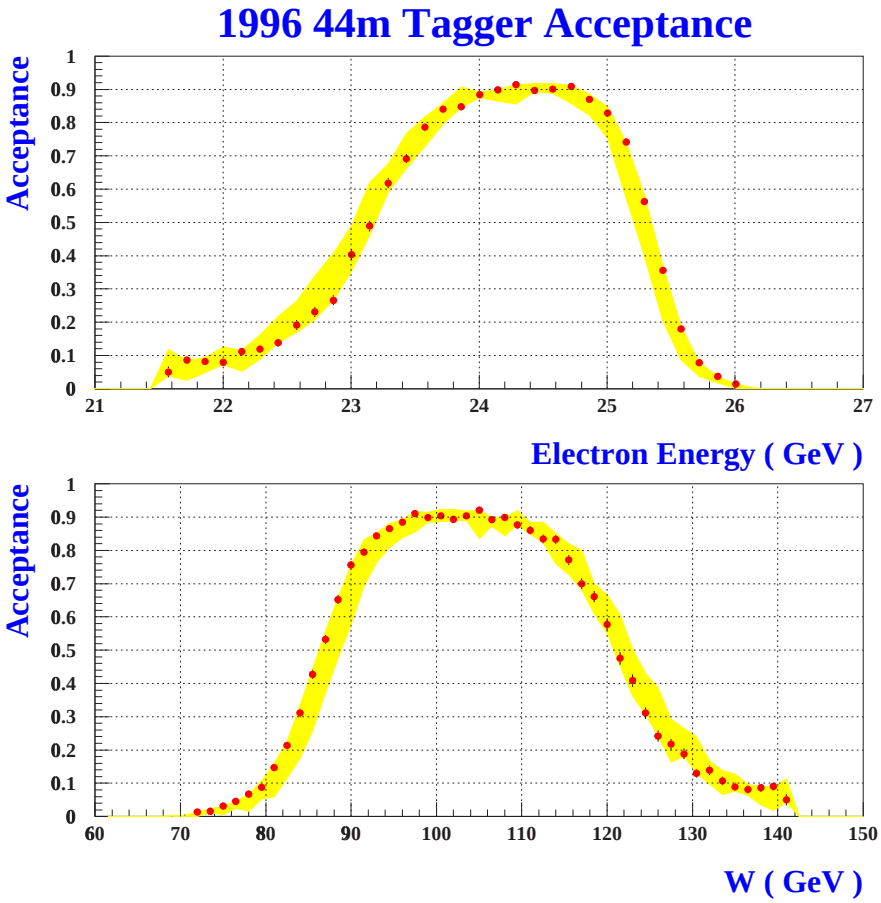

Figure 2.4: *Acceptance of the Photoproduction Tagger in electron energy E'_e and W. Gray bands show the statistical error of the acceptance.[30]*

2.4 The Photoproduction Tagger

The Photoproduction Tagger (PT) [33] is situated upstream the ZEUS detector at $z = -44$ m next to the HERA electron beam pipe to detect electrons with energy E' from ep interactions scattered under angles smaller than a few mrad. Due to this geometry the detector is sensitive to electrons in the energy range $21 < E'_e < 26$ GeV. For this purpose a segment of the electron is equipped with an inclined 1 mm thick

copper exit window. The PT is a small tungsten-scintillator sandwich calorimeter with an overall depth of 24 radiation lengths X_0 consisting of 12 scintillator plates (3 mm thick) and interleaved 7 mm thick tungsten absorber plates of size 70×90 mm^2. Additional scintillator strips are inserted at three different z-positions to allow a simple position measurement. The detector is sensitive to electrons at a distance of $x = 28$ mm from the beam which corresponds to a maximum scattering angle $\theta_{\max}$ such that $Q^2 \approx 4E_e E_{e'} \sin^2(\theta_{\max}/2) < 0.01$ GeV^2 and issues a trigger whenever energy above approximately 1 GeV is deposited. For electrons with energies up to 5 GeV the relative energy resolution is $0.25/\sqrt{E(GeV)}$, and the linearity is better than 1%. Fig. 2.4 shows the acceptance of the Photoproduction Tagger in terms of the energy of the scattered electron E'_e and the γp center of mass energy W.

2.5 The Veto Counters

To reject background events where protons interact with residual gas molecules in the HERA beam pipe the following detector components are used at the ZEUS first level trigger.

Veto Wall The Veto Wall, centered at $z = -7.27$ m, consists of a 87 cm thick iron wall perpendicular to the beam with scintillation counters on both sides. The iron wall helps to absorb background particles which would otherwise hit the central detector while the scintillators provide timing signals that are used to reject events with timing inconsistent with an ep interaction. The Veto Wall has a 80×80 cm^2 hole in its center for the HERA beam pipe and quadrupole magnets.

C5 counter The C5 counter is a small setup of four scintillation counters surrounding the beam pipe at $z = -3.15$ m. Its timing information is used to reject proton beam gas events that were not detected by the Veto Wall.

Small Angle Rear Tracking Detector The Small Angle Rear Tracking Detector (SRTD) is a two-plane scintillator strip detector in front of RCAL at $z = -1.50$ m covering a 68×68 cm^2 area around the beam pipe hole. In this analysis the SRTD signal is used to reject events out of time with ep interactions.

2.6 The Proton Remnant Tagger (PRT)

In this section a detailed description of the Proton Remnant Tagger (PRT) is given. The construction and installation of this component was part of this dissertation project, as well as the calibration of the counters and the integration into the ZEUS data acquisition system. The calibration of the counters and how they are used to tag minimum ionizing particles (MIP) is discussed (see also [14, 15, 16]). The PRT is used in this analysis (see Chap. 4) to identify proton-dissociative events which cannot be detected with CAL.

PRT consists of two scintillation counter setups at $z = 5.15$ m (PRT1) and $z \approx 24$ m (PRT2) that can detect particles escaping detection by CTD and CAL. The location of PRT1 and PRT2 in the HERA and ZEUS environment is shown in Fig. 2.5.

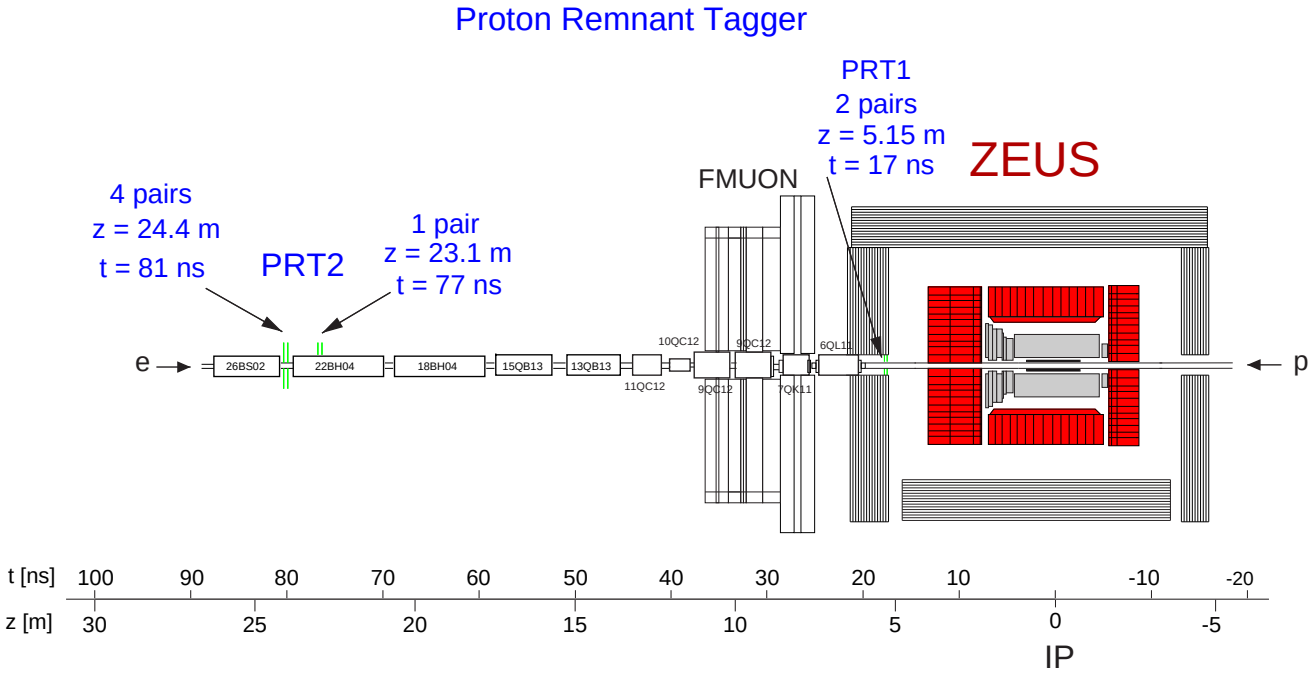

Figure 2.5: *The location of PRT1 and PRT2 in the HERA tunnel and in ZEUS.*

2.6.1 PRT1

On the interaction point side of collimator C3, at $z = 5.15$ m, two pairs of scintillation counters, referred to as PRT1 in the following, were installed around the beam pipe.

PRT1 consists of two rectangular counter pairs of identical shape with a small cutout to accommodate the HERA beam pipe (see Fig. 2.6). The counters of each pair are stacked on top of each other covering the same area to allow requiring coinciding signals to detect high energetic particles, while suppressing backgrounds due to soft particles, including synchrotron radiation photons. Each counter consists of a 26 × 15 cm^2 sized scintillator (SCSN-38, 2.6 mm thick) with an attached plastic light guide and photomultiplier tube. The counters are separated by 1 mm thick layers of lead and the whole structure is shielded by layers of lead. The 6 to 26 mrad coverage of the counters slightly extends the FCAL beam pipe hole. Fig. 2.7 shows the overall layout and the lead-scintillator sandwich structure.

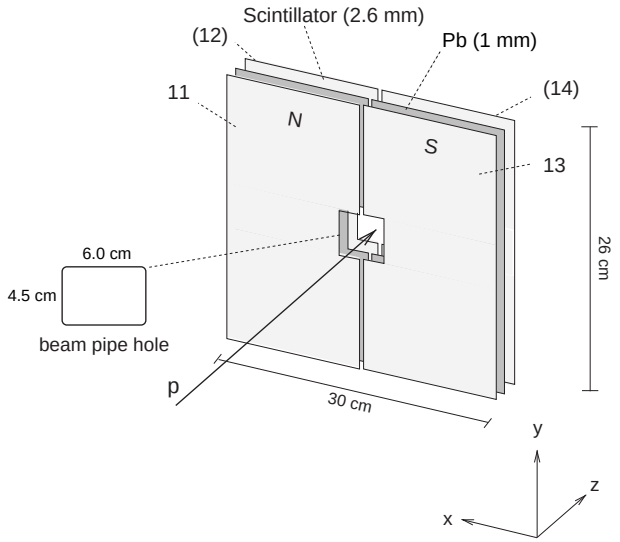

Figure 2.6: *PRT1 setup of the four scintillator tiles 11, 12 (north side) and 13, 14 (south side). A photomultiplier is attached to each scintillator via a light guide (see Fig. 2.7).*

2.6.2 PRT2

PRT2 consists of five counter pairs which are set up in the HERA tunnel at $z \approx 24$ m. At this position the beam line is separated into the proton and the electron beam pipe. Four counter pairs surround the beam pipes ($z = 24.4$ m), roughly covering individual quadrants of the ZEUS xy plane. A gap in acceptance due to a HERA flange attached to the proton beam pipe is covered by a fifth counter pair in the open side of dipole magnet SL22 at $z = 23.1$ m (see Fig. 2.8). We refer to those five counter pairs as PRT2

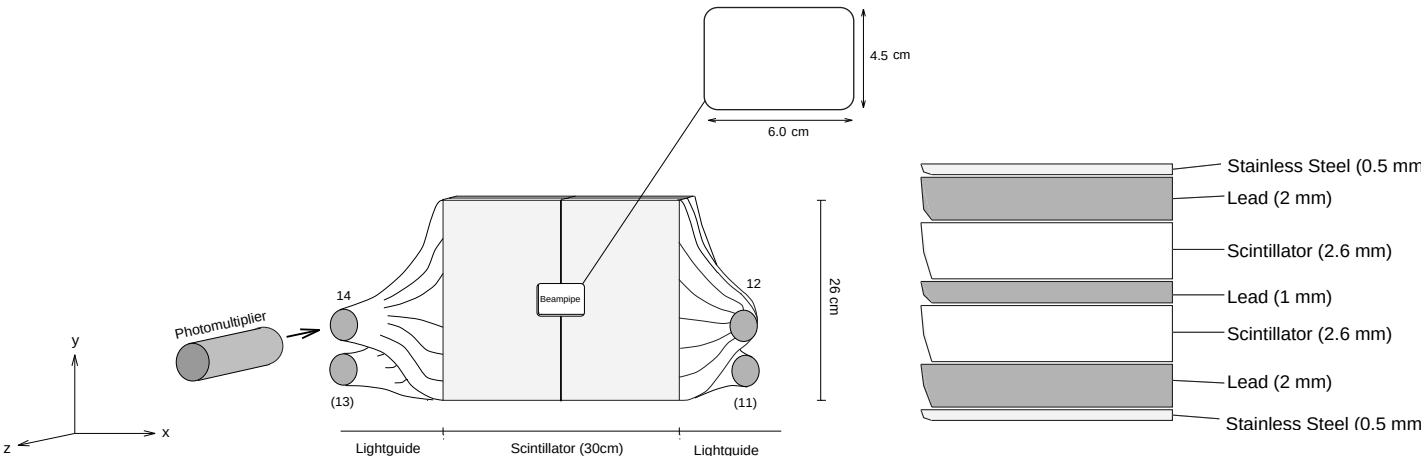

Figure 2.7: *Setup of the two PRT1 counter pairs (channel 11–14) at position* $z = 5.15$ *m.*

in the following. The set of counters around and next to the HERA proton beam pipe will be referred to as PRT2p below. Each counter consists of a 20×25 cm^2 sized scintillator of 4 mm thickness with an attached plastic light guide and photomultiplier tube. The acceptance of PRT2 is about 1.5 to 8 mrad.

Fig. 2.9 shows the position of the PRT1 and PRT2 counters with respect to the HERA beam line elements and their angular coverage. PRT1 is partially obstructed by FCAL and a 5 cm thick tungsten collimator (C4) (see Fig. 2.10). The PRT2 counters are obstructed by HERA magnets.

2.6.3 Calibration of the PRT Counters

Before installation in the ZEUS experiment we calibrated each PRT scintillation counter with radioactive sources to find correct high voltage settings that allow separating signals from high energetic particles hitting the scintillators from noise of the photomultiplier tubes and readout electronics. Additionally, we analyzed data taken during the 1996 run period to calibrate the counters for this analysis.

The PRT readout is attached to the ZEUS calorimeter (CAL) readout electronics which records pulse heights in pC and timing in ns. Figs. 2.11, 2.12 show the pulse height spectra of the two pairs of PRT1 counters (11,12 and 13,14). All spectra show

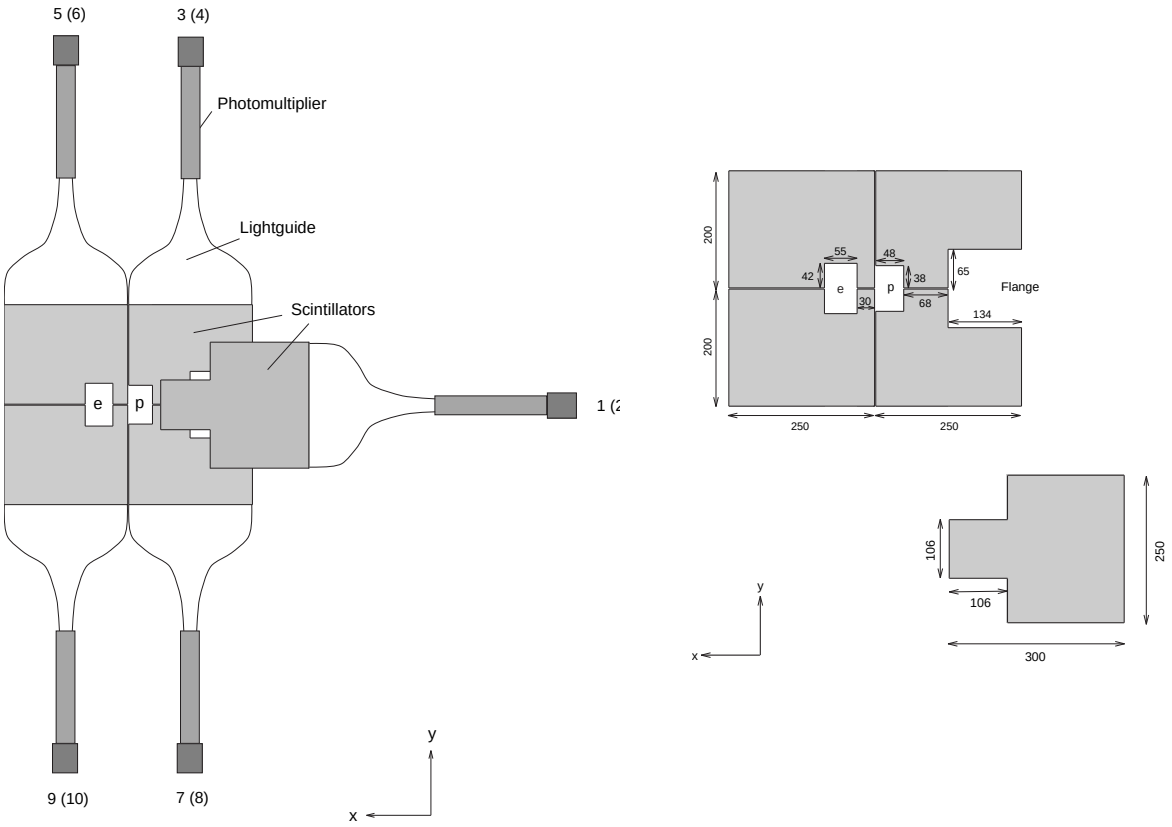

Figure 2.8: *Setup of the PRT2 counter pair at $z = 23$ m (channel 1, 2) and the 4 pairs at $z = 24.4$ m (channel 3 – 10) as seen from the interaction point. Numbers in parentheses indicate counters covered by the adjacent odd numbered counters.*

a clear peak due to minimum ionizing particles (MIP peak), which can serve as a calibration.

The plots in Fig. 2.13 show the pulse height spectra of the ten PRT2 counters. MIP peaks can be seen in counters (1,2) and (9,10), but are less apparent in (3,4) and (5,6). In the spectra of counters (7,8) MIP peaks cannot be seen, and the pulse height cut was chosen just above the noise level.

The plots in Fig. 2.14 show the full scale pulse height spectra of the four PRT1 counters. The peak at $\sim$ 150 pC results from overflow of the readout electronics. Fig. 2.15 shows the pulse height spectra of the PRT2 counters (1,2) for tagged events.

The stability of the positions of the MIP peaks was studied over the entire run period using runs taken with 820 GeV protons in HERA, but no electrons. These runs (FNC neutron runs) were taken on a daily basis by the ZEUS shift crew to test the Forward

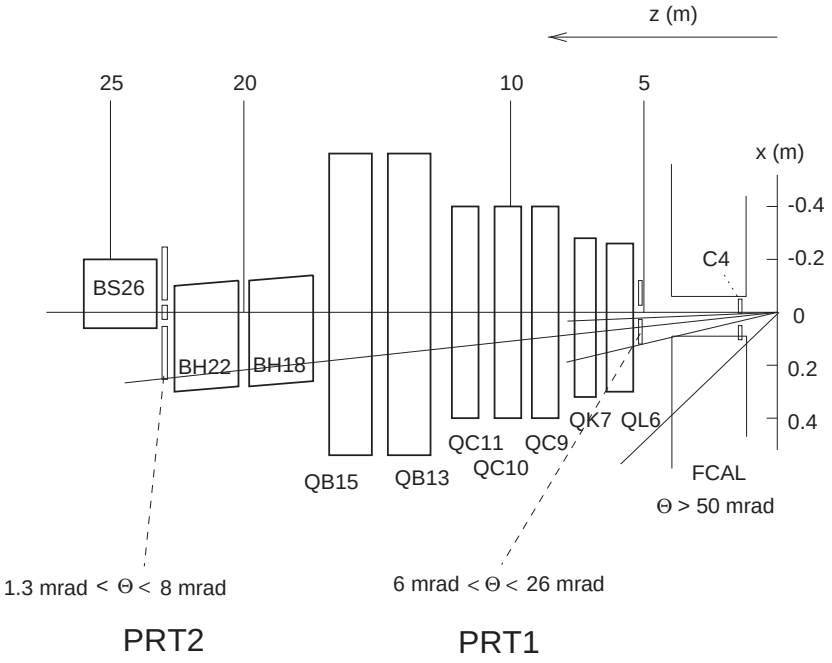

Figure 2.9: *The position of PRT1 and PRT2 counters with respect to the HERA magnets and their angular coverage.*

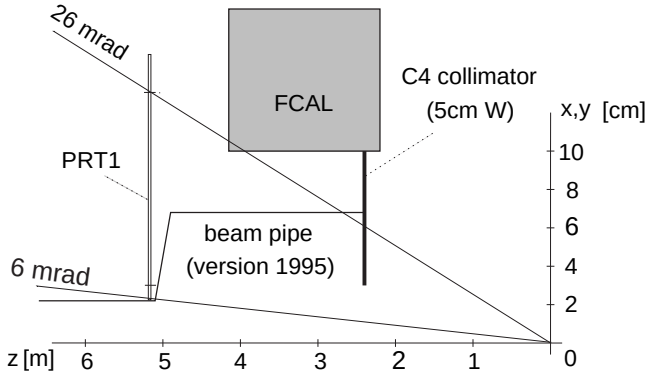

Figure 2.10: *Dead material in front of PRT1 which is partially obstructed by the Forward Calorimeter (FCAL) and a 5 cm thick tungsten collimator.*

Neutron Calorimeter (FNC). Fig. 2.16 shows an example of a pulse height distribution after the coincidence cut was applied. Figs. 2.17 and 2.18 show the position of the MIP peaks versus run number for a sample of 43 runs for PRT1. A dashed line in each plot shows the pulse height cut in pC used to identify signals induced by minimum ionizing particles. In the run range of interest for the physics analysis (see Chap. 4), marked by vertical dotted lines in Figs. 2.17, 2.18, the PRT1 signals are stable and the pulse

height cut can be used to select events with a tag in PRT1.

2.6.4 Timing

PRT1 is located at $z = 5.15$ m, and consequently protons leaving the interaction point at $t_0 = 0$ ns arrive at PRT1 at $t_1 = 17$ ns. Positrons pass PRT1 17 ns before they reach the interaction point. PRT2 is located at $z \approx 24$ m where protons arrive at $t_2 = 80$ ns. In order to be able to use the existing CAL data acquisition chain, the timing of both components had been adjusted by means of signal cables of different lengths which compensate for this effect. Consequently the different timing of PRT1 and PRT2 is not reflected in the data.

Figs. 2.19 and 2.20 show PRT timing spectra from runs taken with only protons of $E_p = 820$ GeV in HERA. Protons arrive at PRT1 at a mean time of $t_1 = -10$ ns. In order to select signals of particles coming from the interaction point only, a timing cut of -20 ns$< t < 10$ ns is applied to the data of PRT1 and of PRT2 in this analysis.

2.6.5 Tagging

After calibration, cuts on the pulse heights can be chosen just below the MIP peak. With reference to the results of the calibration presented in Sec. 2.6.3 the cuts shown in Tab. 2.1 were chosen for the four PRT1 counters (11, 12, 13, 14) and the ten PRT2 counters (1–10).

The counters are organized in pairs of counters which have identical shape and cover the same area. Both counters i, j of a pair have to have a pulse above threshold in order to be considered hit by at least one minimum ionizing particle:

$$(E_i > E_i^{min} \text{ .and. } E_j > E_j^{min}). \tag{2.1}$$

A tag in PRT1 is then defined as follows:

$$(E_{11} > E_{11}^{min} \text{ .and. } E_{12} > E_{12}^{min}) \text{ .or. } (E_{13} > E_{13}^{min} \text{ .and. } E_{14} > E_{14}^{min}). \tag{2.2}$$

The condition for a tag in PRT2 is analogously defined.

	channel	cut [pC]
PRT1	11	1.5
	12	2.0
	13	2.0
	14	2.5
PRT2	1	10.0
	2	10.0
	3	7.0
	4	8.0
	5	8.0
	6	10.0
	7	10.0
	8	11.0
	9	13.0
	10	12.0

Table 2.1: *Pulse height threshold in pC for PRT1 and PRT2.*

2.6.6 Occupancy

Particles hitting a ZEUS subcomponent do not necessarily come from *ep* interactions, but can also be caused by particles accompanying the particle bunches as a halo or by protons hitting residual gas molecules in the HERA beam pipe. These hits must not mistakenly be treated as physics events but as background that has to be subtracted from any studied physics data sample. Studying the rate of background events is especially important in the case of the PRT counters because they are located very close to the HERA beam line. To detect proton-dissociative events with the PRT, background in these counters should be small compared to the rate of the studied physics events. The rate of background events of the individual counters is calculated in the following using events that are randomly triggered.

Random triggers, unlike the triggers that are used to record physics events, are fired at random times without any requirements on the signals in the subcomponents or the HERA bunch crossing number. Their rate is chosen such that one event in about every 200 physics events is a random trigger event. In the following the number of random triggers is denoted N^{rand} and the number of random trigger events with a PRT tag is

$N_{\text{tag}}^{\text{rand}}$. The fraction of random trigger events with an accidental tag $N_{\text{tag}}^{\text{rand}}/N^{\text{rand}}$ in a given counter is called its occupancy.

In order to correct a measured number of tagged events $N_{\text{tag}}^{\text{meas}}$ for accidental tags the occupancy has to be subtracted:

$$N_{\text{tag}}^{\text{corr}} = N^{\text{meas}} \left(\frac{N_{\text{tag}}}{N^{\text{meas}}} - \frac{N_{\text{tag}}^{\text{rand}}}{N^{\text{rand}}} \right),$$

where	N^{meas}	:	number of events in physics data sample
	N_{tag}	:	number of events with a tag in sample
	N^{rand}	:	number of random trigger events
	$N_{\text{tag}}^{\text{rand}}$	:	number of random trigger events with a tag
	$N_{\text{tag}}^{\text{corr}}$	:	corrected number of events with a tag

In the 1996 run period 35897 random trigger events with paired bunches have been recorded in those runs where PRT1 and PRT2 were operational. In order to study their occupancy the same pulse height and timing cuts that are to be used in the physics analysis have been applied to the data (see Tab. 2.1). Tab. 2.2 shows the occupancy of each counter pair using the coincidence requirement. The occupancy of PRT1 and PRT2 using Eq. 2.2 is also given.

The pairs (E_5, E_6) and (E_9, E_{10}), which surround the electron beam pipe, have a very high occupancy. The rates of randomly triggered events with electron pilot bunches which fulfill the pulse height cuts are significantly higher than the rates taken with proton pilot bunches for those two counter pairs. The high occupancy is therefore caused by the electron beam and these counters are excluded from this analysis.

The remaining pairs (E_1, E_2), (E_3, E_4) and (E_7, E_8), which are all located on the proton side of the setup (see Fig. 2.8) were combined and are referred to as PRT2p. The requirement for a tag is analogous to Eq. 2.2 except that the pairs (E_5, E_6) and (E_9, E_{10}) are excluded.

	without timing cut [%]	with timing cut [%]
$E_{11} \wedge E_{12}$	0.54 ± 0.04	0.29 ± 0.03
$E_{13} \wedge E_{14}$	0.55 ± 0.04	0.24 ± 0.03
PRT1		0.41 ± 0.03
$E_1 \wedge E_2$	0.97 ± 0.05	0.31 ± 0.03
$E_3 \wedge E_4$	3.12 ± 0.09	1.68 ± 0.07
$E_5 \wedge E_6$	15.98 ± 0.21	9.42 ± 0.16
$E_7 \wedge E_8$	4.16 ± 0.11	2.42 ± 0.08
$E_9 \wedge E_{10}$	15.94 ± 0.21	9.73 ± 0.16
PRT2		16.74 ± 0.22
PRT2p		3.32 ± 0.10
PRT1.or.PRT2p		3.64 ± 0.10
FCAL		0.50 ± 0.04
PRT1.or.PRT2p.or.FCAL		3.92 ± 0.10

Table 2.2: *Occupancies* $N^{\text{rand}}_{\text{tag}}/N^{\text{rand}}$ *for each pair of counters* $E_i \wedge E_j$ *with the cuts given in Tab. 2.1. For PRT1 the condition given by Eq. 2.2 was used.*

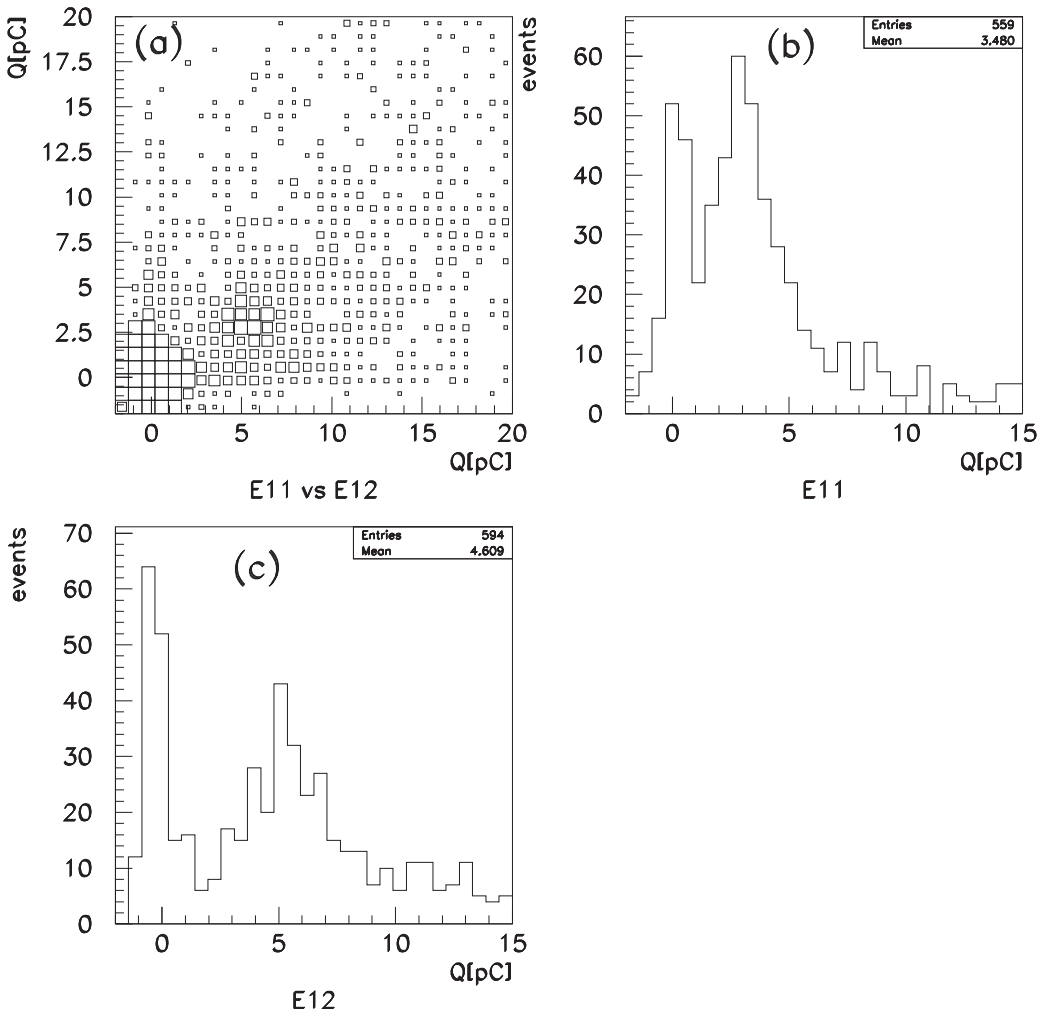

Figure 2.11: *(a) Pulse height spectra of PRT1 channels 11 and 12, plotted versus each other. The data shown were taken during a run with protons of energy* $E_p = 820$ *GeV but no electrons in HERA. (b) Pulse height spectrum of channel 11 using the same data. In order to make the MIP peak visible, coincidence with channel 12 was required by imposing the cut* $2.0 < E_{12} < 8.0$ *pC. (c) Pulse height spectrum of channel 12 with coincidence cut* $2.2 < E_{11} < 6.0$ *pC applied.*

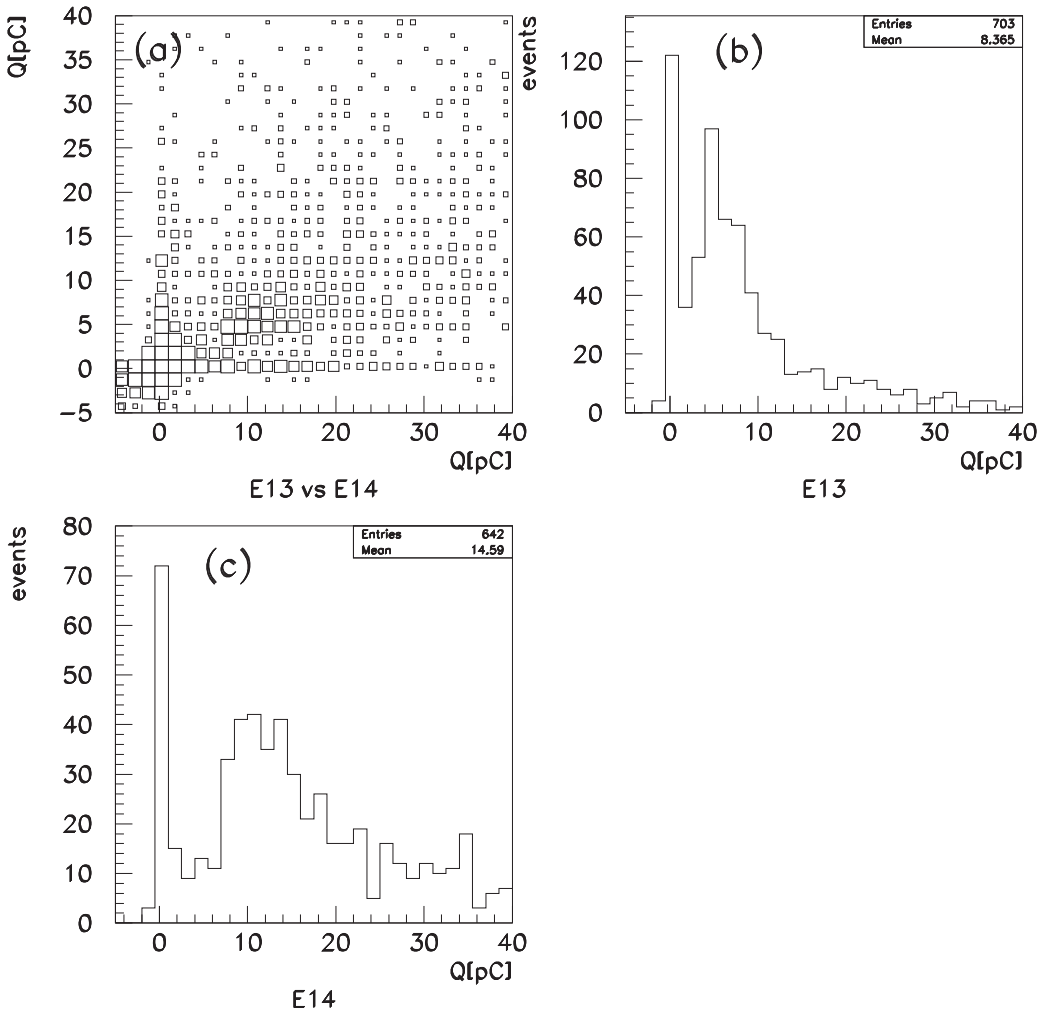

Figure 2.12: *(a) Pulse height spectra of PRT1 channels 13 and 14, plotted versus each other. The data shown were taken during a run with protons of energy* $E_p = 820$ *GeV but no electrons in HERA. (b) Pulse height spectrum of channel 13 using the same data. In order to make the MIP peak visible, coincidence with channel 14 was required by imposing the cut* $4.0 < E_{14} < 20.0$ *pC. (c) Pulse height spectrum of channel 14 with coincidence cut* $4.0 < E_{13} < 12.0$ *pC applied.*

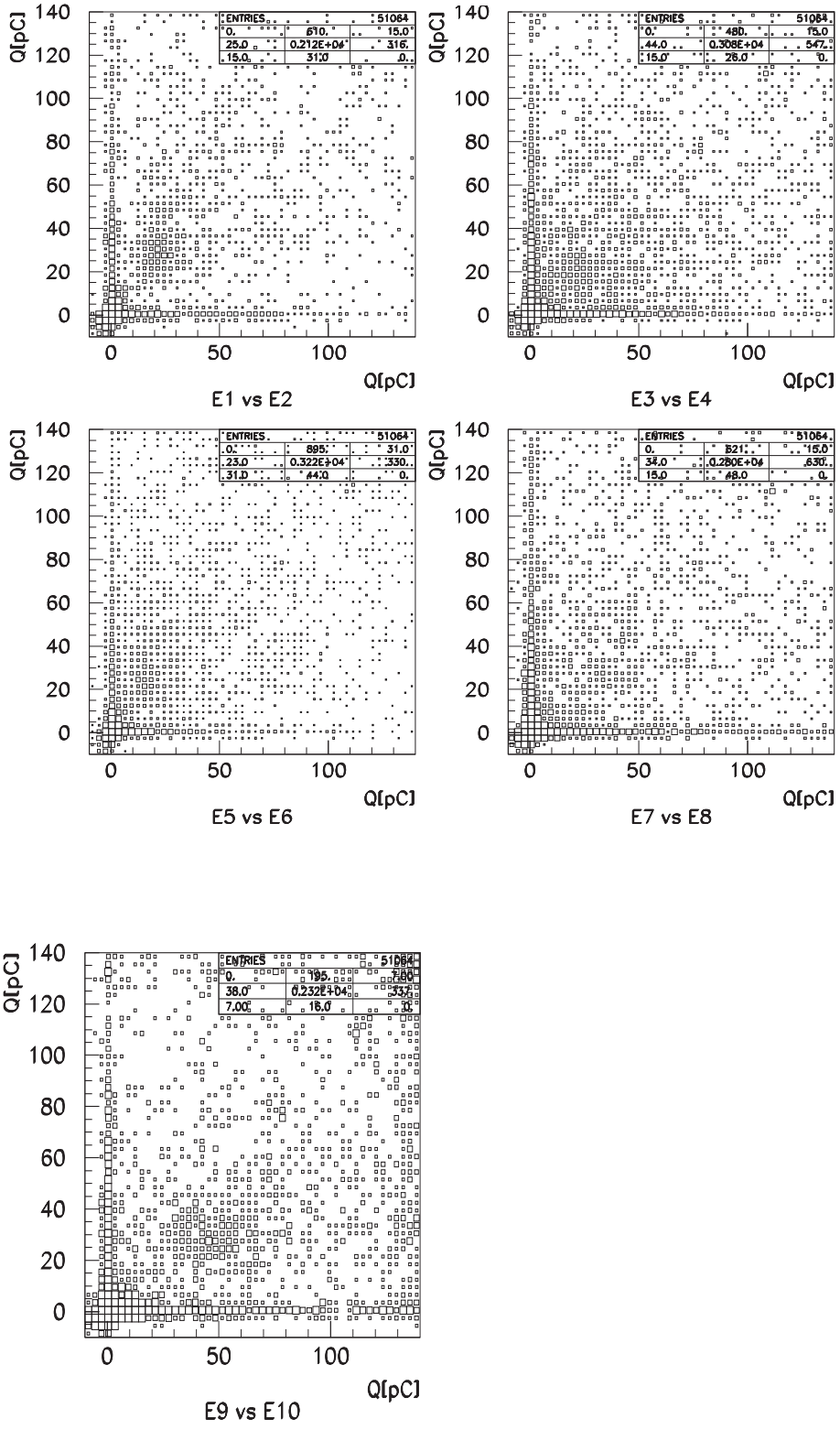

Figure 2.13: *Pulse height spectra of the PRT2 counters; spectra of counters in a pair are plotted against each other.*

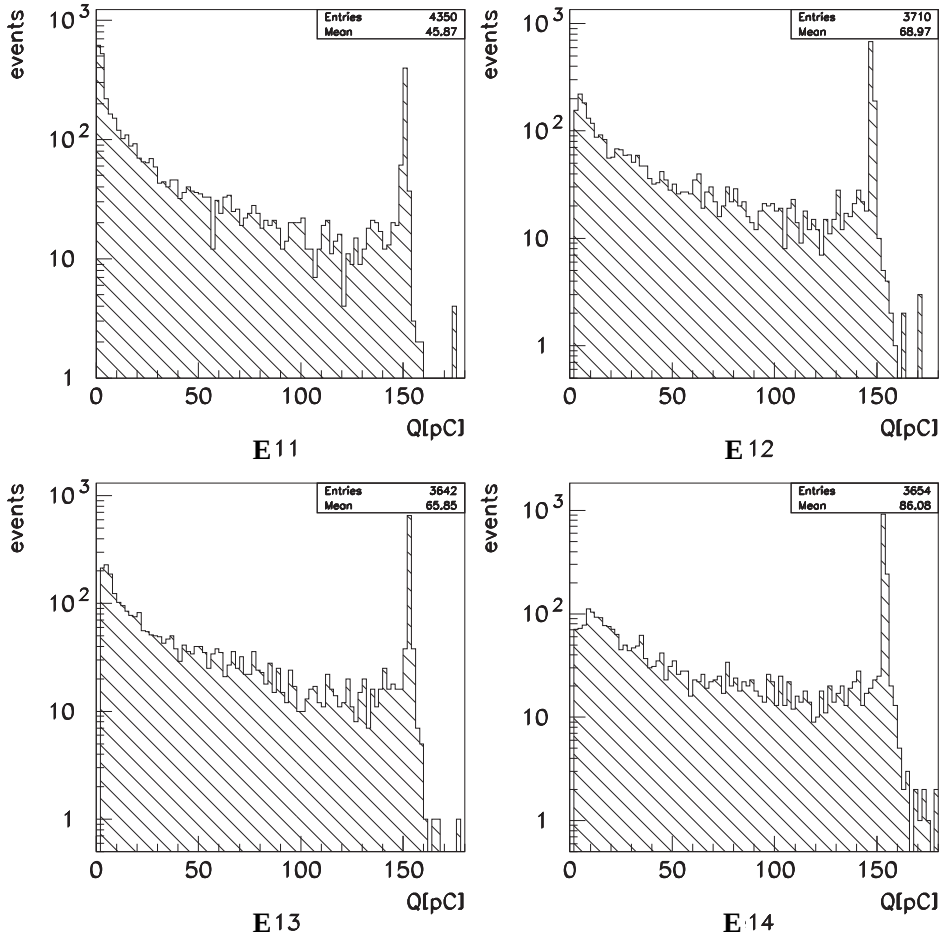

Figure 2.14: *PRT1 full scale pulse height spectra.*

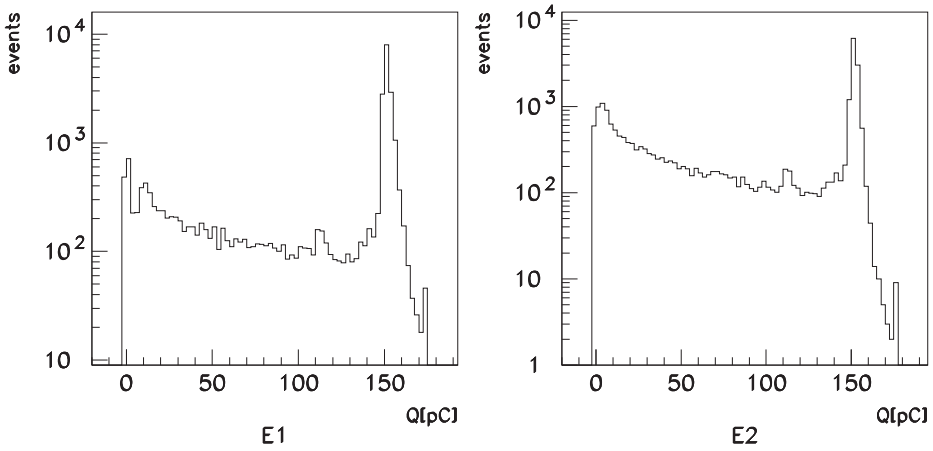

Figure 2.15: *PRT2 channel 1 and 2 full scale pulse height spectra.*

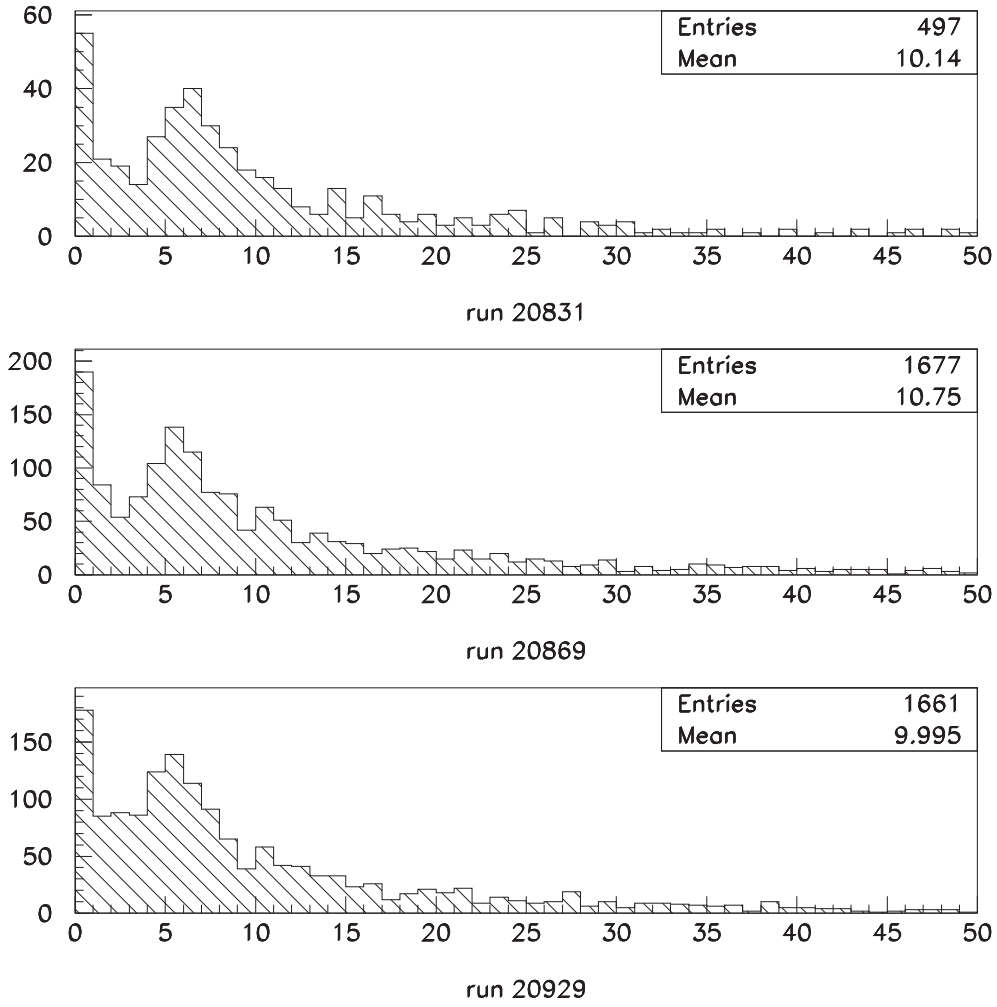

Figure 2.16: *Examples of pulse height spectra of PRT1, channel 13 for three different runs. A sample of 43 runs was analyzed in order to study the stability of the calibration.*

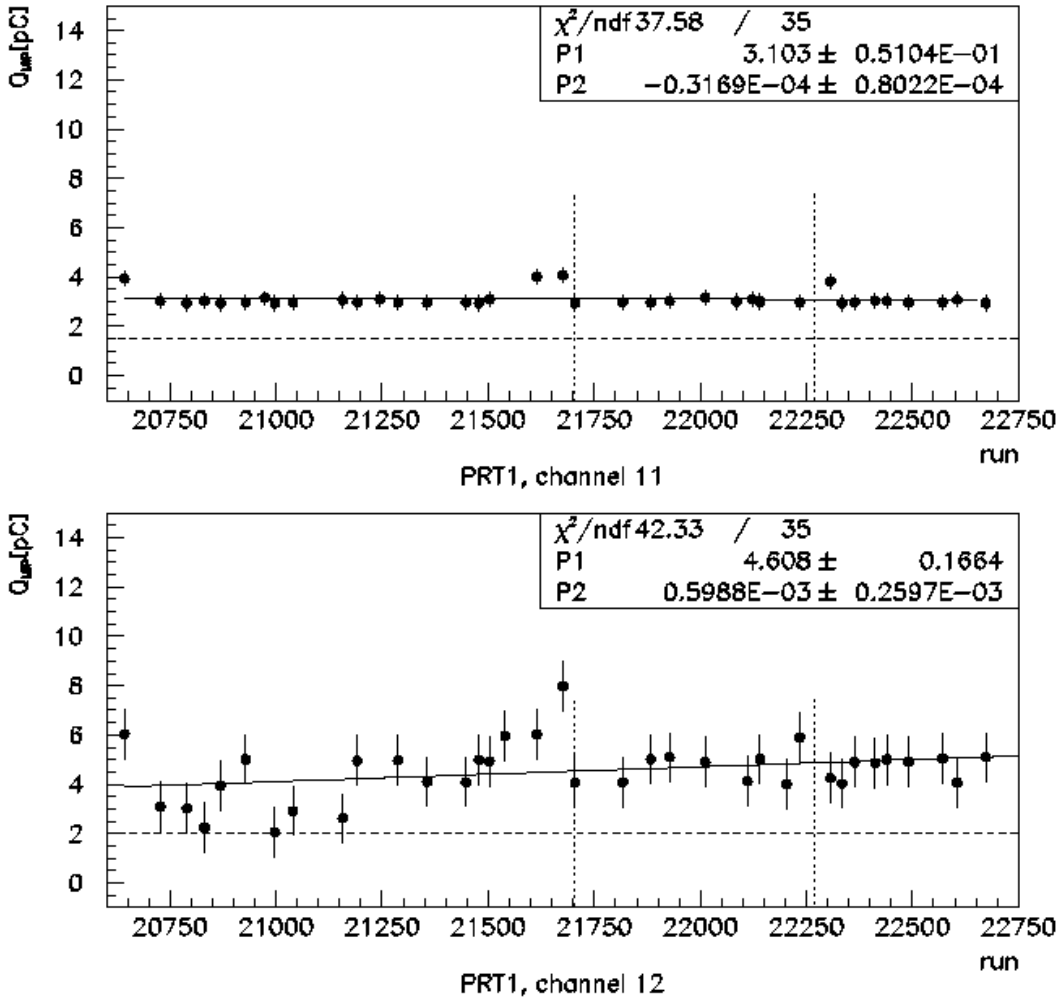

Figure 2.17: *Gain stability of PRT1, channels 11 and 12. Black dots indicate the MIP peak position for individual runs. Superimposed solid lines are fits of the form* $P_1 + P_2 \times N_r$ *with run number* N_r *and dashed lines indicate the MIP cuts used. The two vertical dotted lines in each plot indicate the range of runs that are used in the physics analysis (see Chap. 4).*

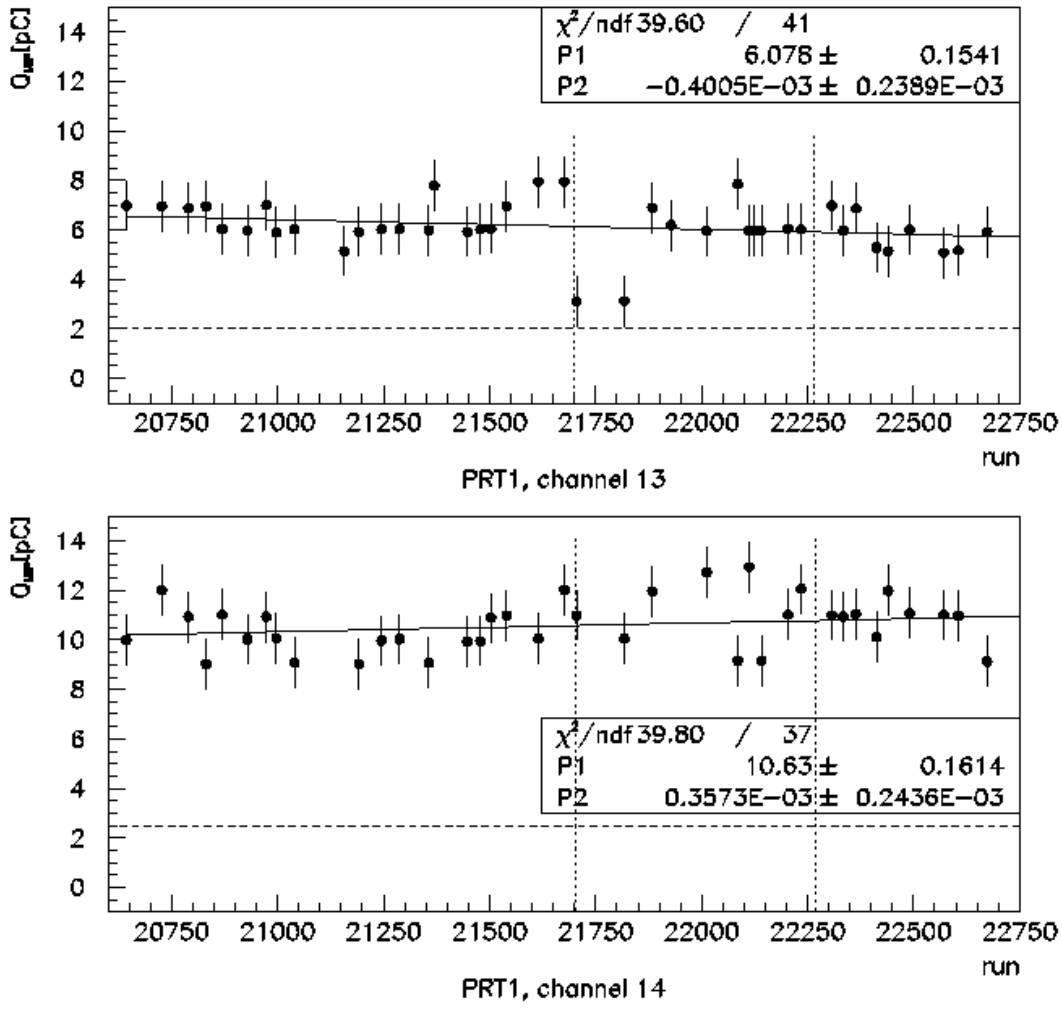

Figure 2.18: *Gain stability of PRT1, channels 13 and 14, explanation see Fig. 2.17.*

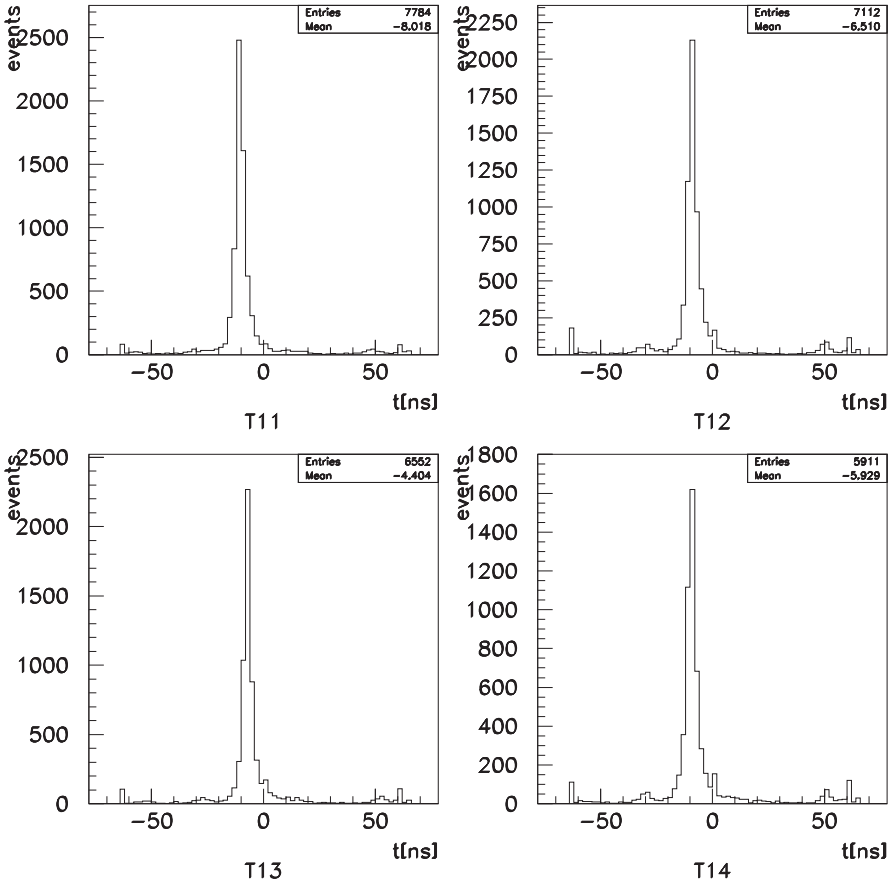

Figure 2.19: *PRT1 timing spectra from runs with only protons in HERA.*

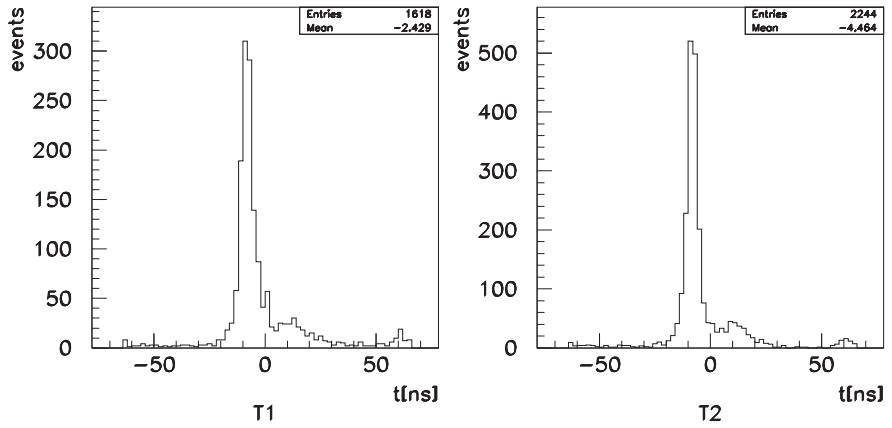

Figure 2.20: *PRT2 timing spectra from runs with only protons in HERA.*

This chapter provided a detailed description of the experimental setup of the Proton Remnant Tagger and the integration into the ZEUS environment. We reported results of the calibration which are necessary for the interpretation of the experimental data collected during ZEUS physics runs.

Chapter 3

Elastic and Proton-Dissociative ρ^0 Photoproduction

Having explained the experimental setup, this chapter comprises the description of the ρ^0 photoproduction reactions which will be analyzed in detail in chapter 4.

Two reactions are studied in this analysis:

$$\begin{aligned} \text{elastic:} \quad & ep \rightarrow ep\rho^0 \quad \text{and} \\ \text{proton-dissociative:} \quad & ep \rightarrow eN\rho^0, \end{aligned} \tag{3.1}$$

where N is a low mass proton-dissociative state with mass M_N. The respective schematic diagrams are shown in Fig. 3.1. In these reactions the incoming electron is scattered under very small angles and can be detected at $z = -44$ m from the interaction point by the Photoproduction Tagger. The small scattering angle fixes the photon virtuality Q^2 to very small values, and the photoproduction cross sections can be accurately computed from the directly measured reactions 3.1. The ρ^0 meson decays into a $\pi^+\pi^-$ pair with a branching ratio of BR $\approx 100\%$. The signature of the elastic reaction is given by the tracks of the two decay pions and their energy deposition in CAL. The proton remains within the beam pipe and is not detected. In proton-dissociative (or inelastic) reactions the decay particles of the diffractive state N can deposit energy in FCAL or the PRT. Nevertheless, diffractive states N of very low mass may still escape detection and then cannot be distinguished from the elastic reaction.

The variables describing the ep interaction are the following. The square s of the ep center of mass energy is given by

$$s = (p + k)^2 \simeq 4E_eE_p \tag{3.2}$$

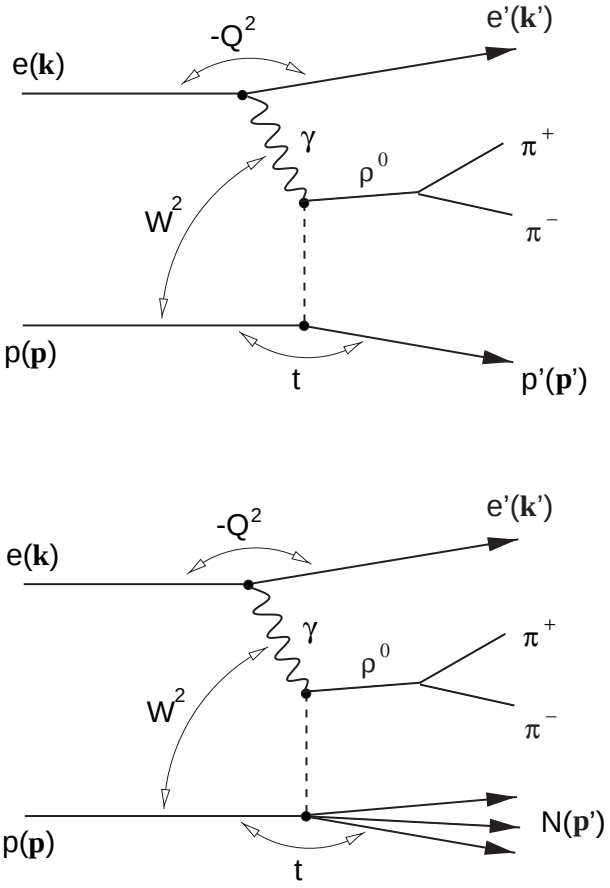

Figure 3.1: *Quasi-real ρ^0 photoproduction in ep collisions. The upper diagram shows the elastic reaction $ep \to ep\rho^0$ and the subsequent decay $\rho^0 \to \pi^+\pi^-$. The lower diagram shows the proton-dissociative or inelastic reaction where the proton breaks up and turns into a diffractive state N with mass M_N.*

with the electron and proton beam energy E_e and E_p. The negative square of the four-momentum of the photon is defined as

$$Q^2 = -q^2 = -(k - k')^2 \simeq 2E_e E_{e'}(1 - \cos\theta_{e'}) \tag{3.3}$$

where $\theta_{e'}$ is the scattering angle of the electron with respect to the direction of motion of the incoming proton and $E_{e'}$ the energy of the scattered electron. The minimum value of Q^2 is given by

$$Q^2_{\min} \approx \frac{m_e^2 y^2}{1 - y} \approx 10^{-9}\ \text{GeV}^2 \tag{3.4}$$

with the electron mass m_e, and the relative energy transfer y from the electron to the

proton in the initial state proton rest frame is given by

$$y = \frac{pq}{pk} \simeq 1 - \frac{E_{e'}}{E_e}\frac{1-\cos\theta_{e'}}{2}. \tag{3.5}$$

The square of the center of mass energy W of the γp system is defined as

$$W^2 = (q+p)^2 \simeq sy - Q^2 \tag{3.6}$$

and for small values of Q^2

$$W^2 \simeq sy. \tag{3.7}$$

The x scaling variable is given by

$$x = \frac{Q^2}{2pq} \simeq \frac{Q^2}{sy}, \qquad 0 \leq x \leq 1. \tag{3.8}$$

In the proton rest frame the energy transfer from the electron to the proton is defined as

$$\nu = \frac{pq}{m_p} \simeq \frac{ys}{2m_p}. \tag{3.9}$$

To describe exclusive ρ^0 production one has to introduce the additional variable t, the square of the four-momentum transfer at the proton vertex:

$$t = (p - p')^2. \tag{3.10}$$

The differential electroproduction cross section is given by

$$\frac{d^2\sigma}{dydQ^2} = \frac{4\pi\alpha^2}{Q^4}\left[xyF_1(y,Q^2) + \frac{1}{y}(1-y)F_2(y,Q^2)\right], \tag{3.11}$$

where α is the fine structure constant and $F_1(y,Q^2)$ and $F_2(y,Q^2)$ are the proton structure functions.

Eq. 3.11 can also be expressed in terms of F_2 and the longitudinal structure function $F_L = F_2 - 2xF_1$:

$$\frac{d^2\sigma}{dydQ^2} = \frac{4\pi\alpha^2}{Q^4}\left[\frac{y}{2}\left(F_2(y,Q^2) - F_L(y,Q^2)\right) + \frac{1}{y}(1-y)F_2(y,Q^2)\right]. \tag{3.12}$$

The transverse and longitudinal cross sections are in the case of very small Q^2

$$\sigma_T^{\gamma p} = \frac{4\pi^2\alpha}{m_p\nu}F_1(\nu,Q^2), \tag{3.13}$$

$$\sigma_L^{\gamma p} = \frac{4\pi^2\alpha}{Q^2}F_2(\nu,Q^2) - \frac{4\pi^2\alpha}{m_p\nu}F_1(\nu,Q^2) = \frac{4\pi^2\alpha}{m_p\nu}\left(\frac{F_2(\nu,Q^2)m_p\nu}{Q^2} - F_1(\nu,Q^2)\right).$$

Finally

$$\frac{d^2\sigma}{dydQ^2} = \frac{\alpha}{2\pi}\frac{1}{Q^2}\left[\left(\frac{1+(1-y)^2}{y} - \frac{2(1-y)}{y}\frac{Q^2_{\min}}{Q^2}\right)\sigma_T(y,Q^2) + \frac{2(1-y)}{y}\sigma_L(y,Q^2)\right]. \tag{3.14}$$

Photoproduction of light vector mesons employs the characteristics of hadronic interactions, namely

- weak dependence of the cross section with center of mass energy (see Fig. 3.2);
- exponential fall-off of the differential cross section $d\sigma/d|t| \propto e^{-b|t|}$.

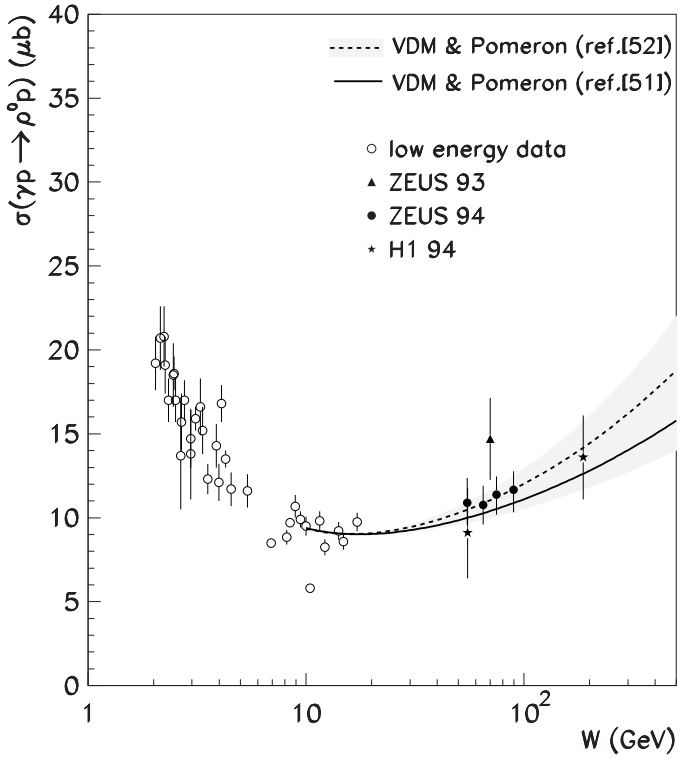

Figure 3.2: *Cross section of ρ^0 photoproduction as a function of the center of mass energy W in fixed target experiments and at HERA [47].*

To study ρ^0 production by quasi-real photons, events with low $Q^2 \ll m_\rho^2$ have to be selected. This is done by requiring the electron to be detected by the Photoproduction

Tagger, which limits the kinematical range to $Q^2 < 0.01$ GeV^2 [33] and we have, to a very good approximation,

$$p_T^2 \approx |t|, \tag{3.15}$$

where p_T is the transverse momentum of the ρ^0 with respect to the beam direction.

The kinematical quantities of ρ^0 photoproduction can be explained with Fig. 3.1. The kinematic variables characterizing the reaction are transverse momentum p_T and γp center of mass energy W. They are determined from the decay pions of the ρ^0 meson. The ρ^0 meson is reconstructed from the two oppositely charged tracks in the CTD. Its transverse momentum is computed from the transverse momenta of the two decay pions:

$$p_T^2 = (p_{x\pi^+} + p_{x\pi^-})^2 + (p_{y\pi^+} + p_{y\pi^-})^2, \tag{3.16}$$

where p_x, p_y are the x and y components of the pion three-momenta measured with the CTD. The photon-proton center of mass energy W is computed by:

$$W = \sqrt{2E_p(E_{\rho^0} - p_{z\rho^0})}, \tag{3.17}$$

where E_p is the energy of the incoming proton and E_{ρ^0}, p_{ρ^0} are energy and z component of the three-momentum of the ρ^0 respectively. E_{ρ^0} is given by the sum of the energies of the two pions, which are calculated from the three-momenta measured in the CTD assuming the two charged particles are pions.

$$\begin{aligned} E_{\rho^0} &= E_{\pi^+} + E_{\pi^-} \\ \text{where} \quad E_\pi &= \sqrt{m_\pi^2 + |p_\pi|^2}. \end{aligned} \tag{3.18}$$

Then the mass of the $\pi^+\pi^-$ state is calculated as:

$$m_{\pi^+\pi^-} = \sqrt{(E_{\pi^+} + E_{\pi^-})^2 - (p_{x\pi^+} + p_{x\pi^-})^2 - (p_{y\pi^+} + p_{y\pi^-})^2 - (p_{z\pi^+} + p_{z\pi^-})^2}. \tag{3.19}$$

The proton dissociative-reaction is characterized by one more variable, the mass M_N of the proton-dissociative system. This variable is not measured directly in this experiment. However, trigger and selection cuts limit the values of M_N to $M_N^2/W^2 \lesssim 0.09$.

Chapter 4

Experimental Procedure

The data sample used in this analysis consists of events taken during the 1996 running period. During this period HERA was running with 820 GeV protons and 27.5 GeV positrons. Runs in which either the Photoproduction Tagger or the PRTs were not fully operational had to be excluded, leaving runs in the range 21704 – 22263 which corresponds to an integrated luminosity of 1.8 pb^{-1}. To select ρ^0 photoproduction events from all events taken during this run period, selection cuts had to be applied. The main requirements are exactly two tracks in CTD and an electron hit in the Photoproduction Tagger.

4.1 Trigger and ρ^0 Selection Cuts

In the following a detailed description of this trigger will be given. It consists of three different levels, namely the first level trigger (FLT), second level trigger (SLT) and third level trigger (TLT).

FLT

- a trigger issued by the Photoproduction Tagger, energy threshold $E_{PT} \gtrsim 1$ GeV;
- Lumi veto: no energy above thresholds ($E_\gamma < 0.847$ GeV, $E_e < 1.049$ GeV) in Lumi calorimeters;
- less than six tracks in CTD;
- less than 3.750 GeV energy deposited in the calorimeter towers around the beam pipe in FCAL;

- track quality cuts;
- timing cuts on signals in C5 counter, veto wall and SRTD to exclude events with particles not coming from the interaction point.

SLT
- less than four tracks measured by CTD;
- a reconstructed vertex with $|z_v| < 0.60$ m or no reconstructed vertex but less than 15 unmatched track segments;

TLT
- exactly one reconstructed vertex with $|z_v| < 0.66$ m;
- exactly two reconstructed tracks in CTD pointing to the vertex;
- $W > 40$ GeV.

The events which survived the requirements of the three trigger levels are fed into the ZEUS data stream which is then written to tape. They are flagged with a unique trigger bit (DST bit 52) which is used to select the data. A separate offline analysis code is used to retrieve the events of interest from the tapes and impose the following tighter standard cuts to the data to select ρ^0 events [44]. Accept events with:

- one reconstructed vertex only,
- z–position of vertex -40 cm $< z < 40$ cm,
- less than six tracks and exactly two vertex tracks,
- the particles assigned to the two vertex tracks be oppositely charged,
- pseudo-rapidity of both tracks $|\eta| < 2.2$,
- transverse momentum p_T of both tracks $p_T > 0.15$ GeV,
- mass of the two-pion system $0.55 < m_{\pi^+\pi^-} < 1.0$ GeV, to exclude other reactions which leave a similar signature in the detector (e. g. $\Phi \to K^+K^-$),
- γp center of mass energy in the range $75 < W < 105$ GeV,

In addition to these cuts, a procedure referred to as *CAL track matching* is performed which rejects events with energy in CAL above noise level in regions inconsistent with the extrapolated two vertex tracks. The following cuts were applied on the different CAL sections:

RCAL: $E_{RCAL} < 160$ MeV (200 MeV) outside a cone with radius $r = 40$ cm (55 cm) around extrapolated tracks in EMC (HAC);

BCAL: $E_{BCAL} < 240$ MeV outside $r = 40$ cm in EMC.

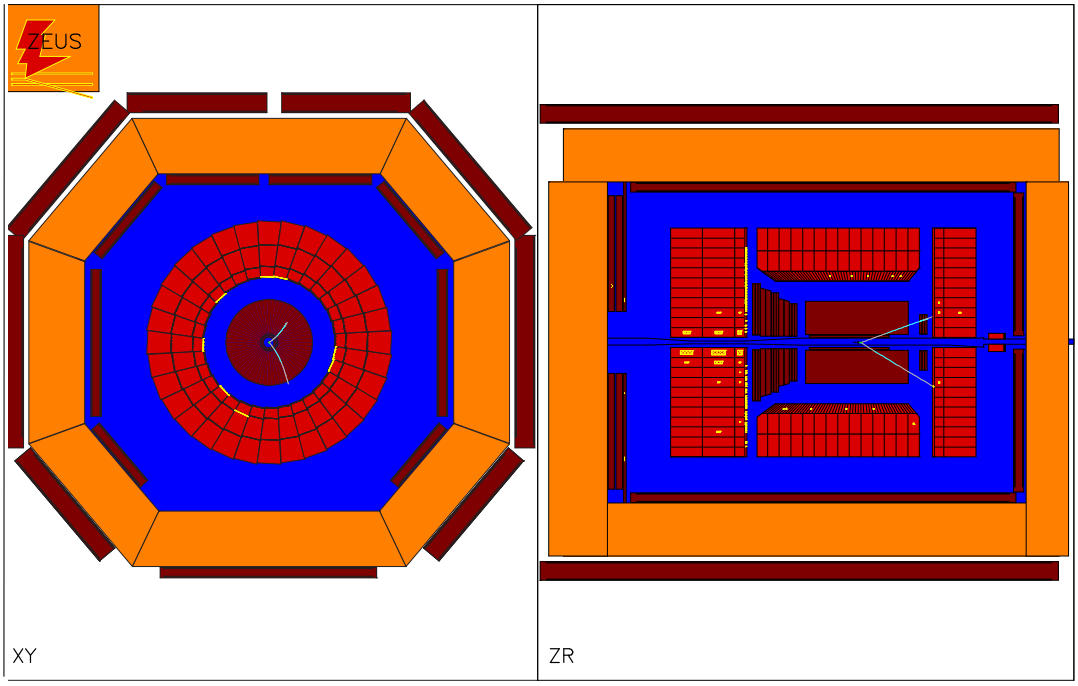

Figure 4.1: *$\gamma p \to \rho^0 N$ event in the ZEUS event display. The left diagram shows a cross section perpendicular through the ZEUS detector, i. e. the x-y plane. The diagram on the right is a section along the beamline in the z-r plane. Two tracks of oppositely charged particles are visible in CTD while the outgoing electron is not detected. The proton-dissociative mass state N deposited energy in FCAL.*

By requiring exactly two vertex tracks and excluding events with energy deposition in RCAL and BCAL which is inconsistent with those tracks, the bulk of inelastic events are already eliminated. The sample remaining after all selection cuts contains about 30000 events.

At this stage no requirements on the energy deposition in FCAL are made and the selected sample is a mixture of elastic and proton-dissociative events. Fig. 4.1 shows the ZEUS event display with a typical ρ^0 event selected by these cuts. The deposited energy in FCAL indicates that it is a proton-dissociative event.

The histogram in Fig. 4.2 shows the uncorrected invariant $\pi^+\pi^-$ mass spectrum after all cuts except the $m_{\pi^+\pi^-}$ mass cut. The peak in the mass spectrum was fitted in the range $0.55 < m_{\pi^+\pi^-} < 1.0$ GeV using a Breit-Wigner function:

$$f^{BW}(m_{\pi\pi}) = \frac{Nb}{\pi} \cdot \frac{\Gamma_\rho/2}{(m_\rho - m_{\pi\pi})^2 + (\Gamma_\rho/2)^2} \tag{4.1}$$

with the normalization factor N and the bin width of the histogram $b_i = 25$ MeV. The resulting fit parameters are the ρ^0-mass $m_\rho = 764 \pm 1$ MeV and the width of the resonant $\Gamma_\rho = 182 \pm 3$ MeV are comparable with the values given in [20]. In Chap. 7 it will be shown that this naive approach is not sufficient to extract the ρ^0 resonance from the corrected data and a more realistic fit will be done.

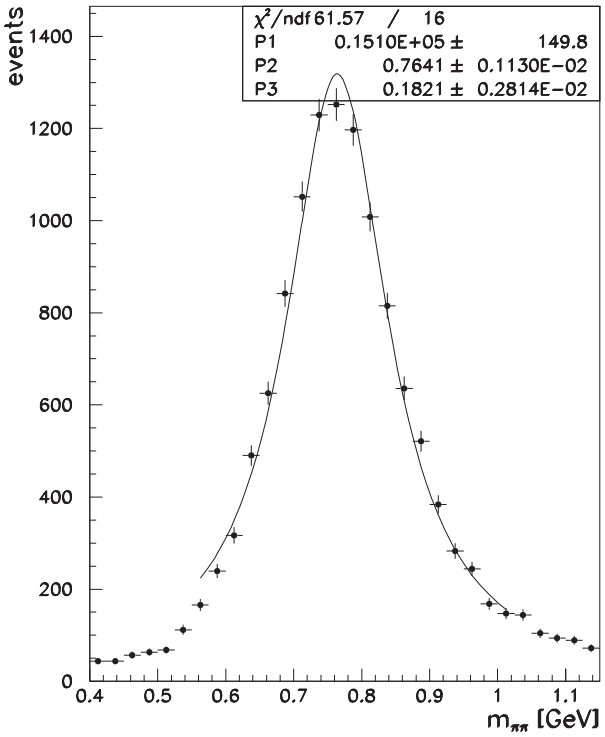

Figure 4.2: *Reconstructed invariant $\pi^+\pi^-$ mass distribution after all selection cuts (except the cut on $m_{\pi^+\pi^-}$). The continuous curve is a fit to the data using expression 4.1.*

Fig. 4.3 shows the distribution of p_T^2 and the γp center of mass energy W without acceptance corrections.

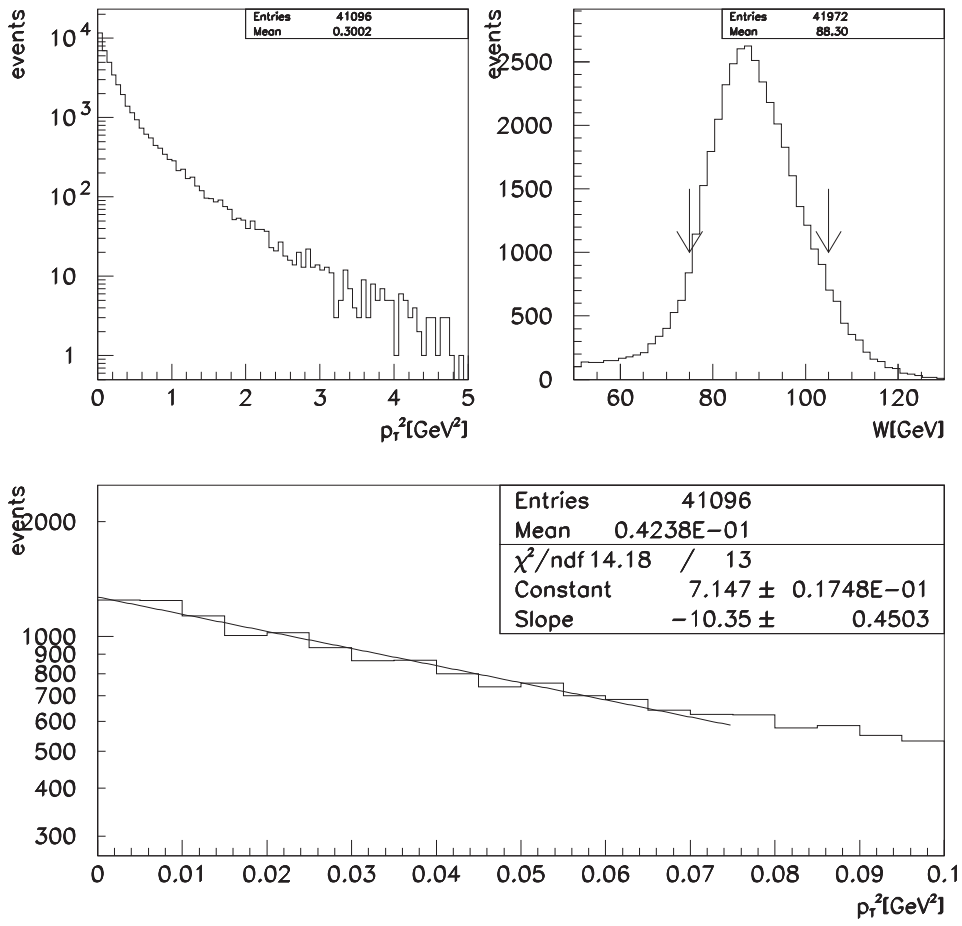

Figure 4.3: *Reconstructed transverse momentum of the $\pi^+\pi^-$ system after the selection cuts (except for the p_T^2 cut on the left plot and the W cut on the right plot). The arrows in the W plot indicate the ρ^0 selection cut $75 < W < 105$ GeV. The bottom plot shows the p_T^2 distribution in the range $0 < p_T^2 < 0.1$ GeV^2 with a superimposed single exponential fit function.*

The resolution of the $|t|$ and W measurement was studied with Monte Carlo events. For this purpose a sample of 100000 elastic events $\gamma p \rightarrow \rho^0 p$ was generated with EPSOFT [28] and passed through the simulation of the ZEUS detector, MOZART, and the simulation of the trigger, ZGANA. The resulting data were then reconstructed by the program ZEPHIR, the same code that is used to reconstruct data from ZEUS physics runs. Finally, a separate analysis code was used to applied the ρ^0 selection cuts

mentioned above. An introduction to the ZEUS analysis environment can be found in [29].

Plot (a) in Fig. 4.4 shows the correlation between generated $|t|_{\text{true}}$ and reconstructed $|t|_{\text{rec}}$. Plots (b) and (c) in Fig. 4.4 show the differences between the generated and reconstructed distributions of $|t|_{\text{rec}} - |t|_{\text{true}}$ and $W_{\text{rec}} - W_{\text{true}}$ respectively. The superimposed fits are the sum of two Gaussians:

$$f(x) = P_1 \left[\exp\left(-\frac{(x-P_2)^2}{2P_3^2} \right) + P_4 \exp\left(-\frac{(x-P_2)^2}{2P_5^2} \right) \right], \tag{4.2}$$

where x denotes $|t|_{\text{true}} - |t|_{\text{rec}}$ and $W_{\text{true}} - W_{\text{rec}}$ respectively. Fit parameter P_2 is the shift of the reconstructed with respect to the generated distribution. In the case of $|t|$ the shift is compatible with zero within the error. The reconstructed values of W are shifted by about 500 MeV towards smaller values, which is small compared to the used W range 75 – 105 GeV and can be neglected. The detector resolution for $|t|$ and W is given by fit parameters P_3 and P_5. In both fits the first term dominates and the detector resolution becomes $\sigma_{|t|} = 0.05$ GeV^2 and $\sigma_W = 4.7$ GeV.

The stability of the trigger and the described selection cuts during the data taking period was studied in terms of events per integrated luminosity versus run number, which is shown in Fig. 4.5. The significant run-to-run fluctuations are mainly caused by lateral shifts of the average ep vertex position which change the tagging efficiency of the Photoproduction Tagger.

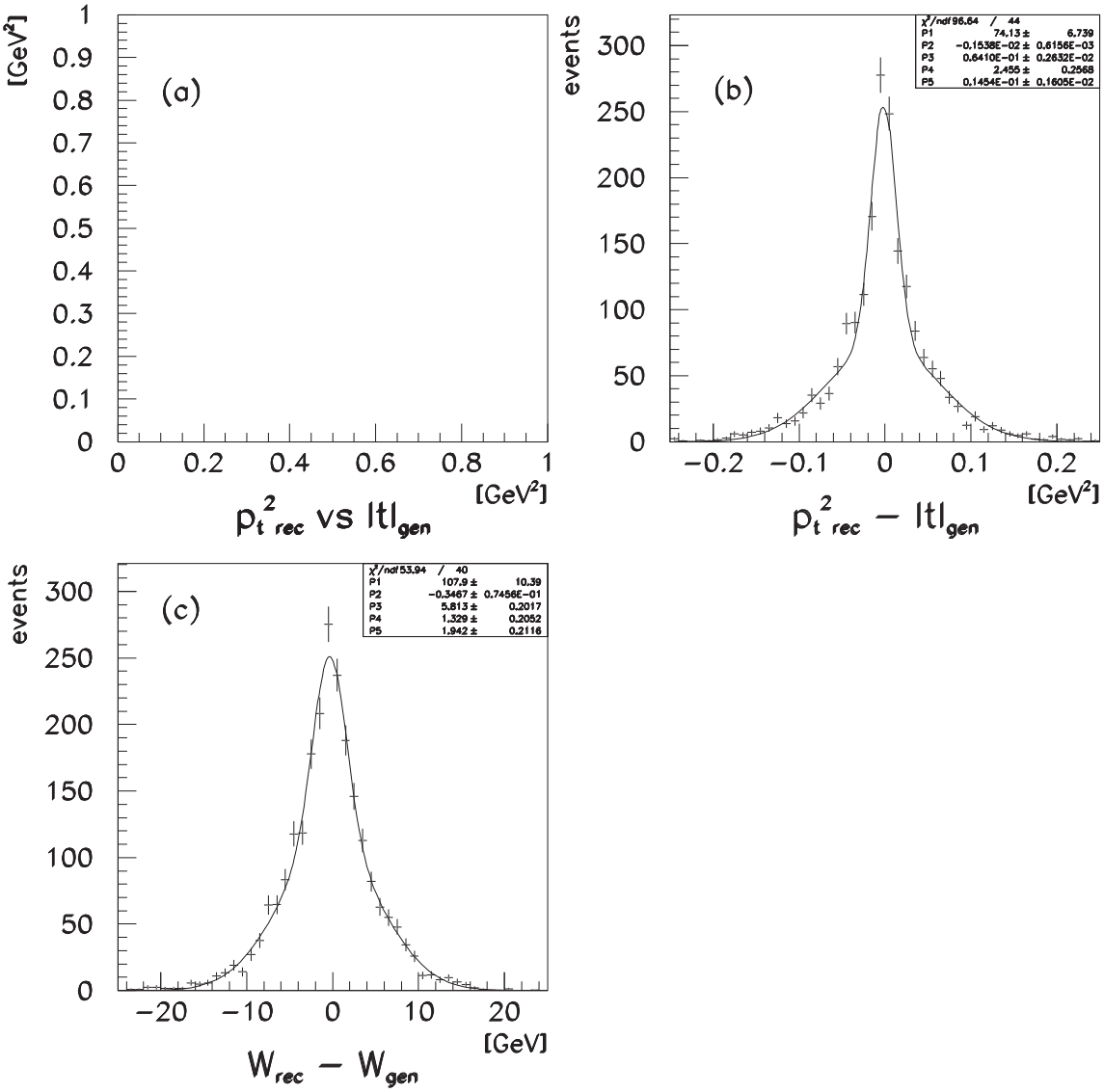

Figure 4.4: *Correlation (a) and difference (b) between generated and reconstructed $|t|$ for elastic Monte Carlo events. Plot (c) shows the difference between generated and reconstructed center of mass energy W. All ρ^0 selection cuts (see Sec. 4.1) are applied, with the exception of the cut on $|t|$ in plot (a). The superimposed fit in (b) and (c) is a double Gaussian (see Eq. 4.2).*

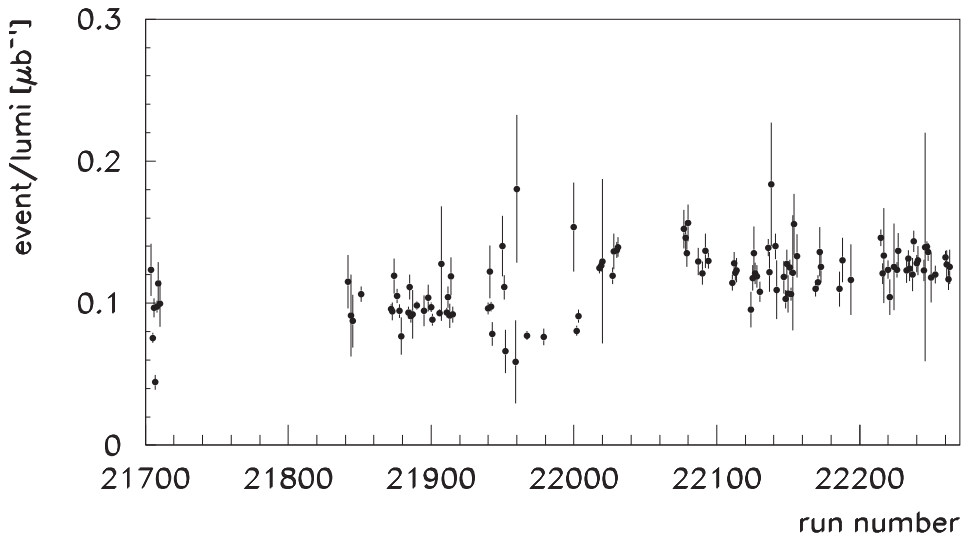

Figure 4.5: *Number of events per integrated luminosity versus run number. Plotted are all events triggered by the Photoproduction Tagger (DST bit 52) with the* ρ^0 *selection cuts applied.*

4.2 Identification of Proton-Dissociative Events

Proton-dissociative events are identified by tags in PRT or FCAL.

A PRT tag is defined as follows: At least one minimum ionizing particle must have been recorded in both counters of any pair of PRT1 or PRT2p and the arrival time of the signals must be consistent with particles coming from the interaction point. [16]

The measured counting rates of the PRT counters have been corrected for accidental coincidences as described in Sec. 2.6.6. Correction for accidentals for those counters of PRT2 which are located around the HERA electron beam pipe, namely (E_5, E_6), (E_9, E_{10}), are very large. Therefore, these counters will be excluded from this analysis. Only the PRT2p counters situated around the proton beam pipe (E_3, E_4), (E_7, E_8) and next to it (E_1, E_2) are being used.

The counting rates of the PRTs are to be used to measure the contribution of proton-dissociative events in the selected data sample. It is necessary to check whether the PRT counting rates vary with time. Fig. 4.6 shows the fraction of ρ^0 events tagged by PRT1 and PRT2p over the run period. The distributions are flat within statistical fluctuations.

It was also checked whether the PRT counting rates depend on the azimuth angle ϕ_ρ of the ρ^0, which is given by the transverse components of its momentum

$$\phi_\rho = \arctan \frac{p_y}{p_x} \tag{4.3}$$

such that for $\phi_\rho = 0$ the ρ^0 transverse momentum is along the positive x axis. Fig. 4.7 shows the azimuth angle ϕ_ρ distributions for events with a tag in PRT1 for two p_T^2 ranges. The distributions are flat within statistical fluctuations, which reflects the fact that PRT1 covers the full ϕ_ρ range effectively.

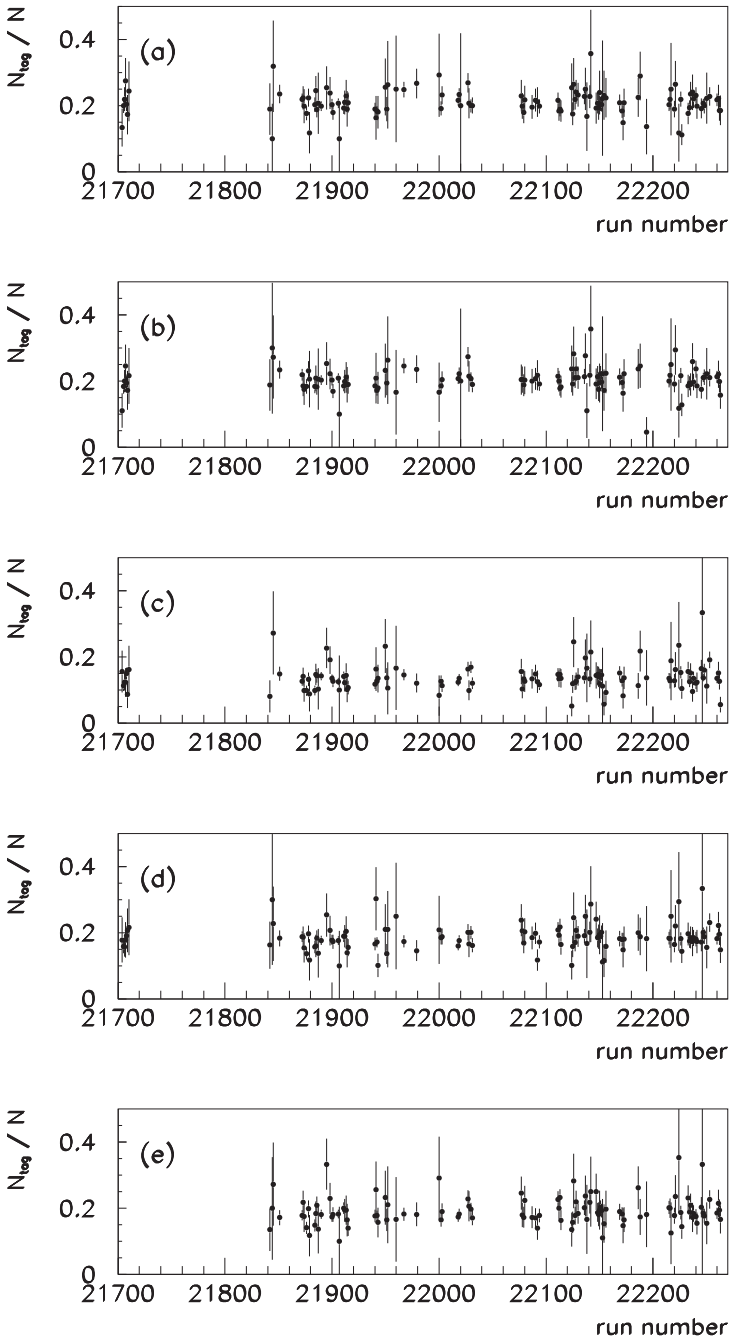

Figure 4.6: *Fraction N_{tag}/N of ρ^0 events tagged by PRT1, north half (a), PRT1, south half (b), PRT2(1,2) (c), PRT2(3,4) (d) and PRT2(7,8) (e).*

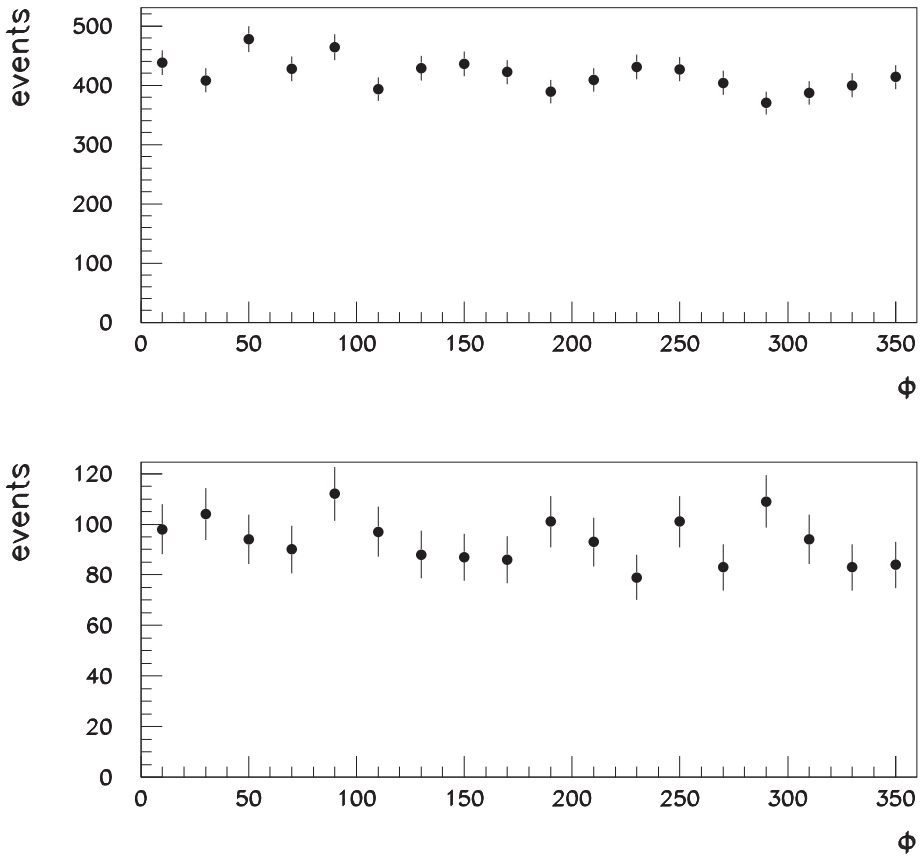

Figure 4.7: *Azimuth angle distribution of ρ^0 events with a tag in PRT1 in the range $p_T^2 < 1.0\ GeV^2$ (upper plot) and $p_T^2 \geq 1.0\ GeV^2$ (lower plot) in bins of $\Phi = 20°$.*

Since PRT2p consists of counters only located on the proton side of the accelerator, a lower acceptance is expected for events where the proton remnant points to the counters located on the electron side. This area corresponds to values of the azimuthal angle of the ρ^0 of $\phi_\rho \approx 180°$. This effect can be seen in the ϕ_ρ distribution in Fig. 4.8.

To study whether scattered protons from elastic ρ^0 production with high transverse momentum p_T can also induce hits in the PRT counters, elastic Monte Carlo events were used. In 100000 events not a single event with a tag in a PRT1 counter was found. However, the situation is different for PRT2. Fig. 4.9 shows as a function of p_T^2 the fraction of Monte Carlo events with a tag in the different PRT2 counter pairs after all selection cuts. The tagging efficiency for elastically scattered protons reaches $\sim 10\%$ at about $p_T^2 \approx 0.2$ GeV^2 with the exception of counter pair (1,2), where the tagging efficiency for those events is negligible for $p_T^2 < 0.5$ GeV^2. Therefore, for large values of p_T^2 the PRT2 counters can not be used to identify inelastic events.

Since it is possible that the very forward region of the detector including HERA beam line elements is not simulated in MOZART perfectly, the p_T^2 dependence of the PRT2 counters for elastic events has to be studied with physics data, also. FCAL and PRT1 are used to veto inelastic events with an outgoing hadronic system with high masses M_N. Fig. 4.10 shows the p_T^2 distributions of the remaining events for the PRT2p counters. For values $p_T^2 < 0.3$ GeV^2 the distributions show an exponential fall-off with a slope of -4.6 ± 0.5 GeV^{-2} (channels 1,2), -3.9 ± 0.4 GeV^{-2} (channels 3,4) and -4.1 ± 0.4 GeV^{-2} (channels 7,8). However, there is a strong deviation from this exponential fall-off for values of $p_T^2 > 0.3$ GeV^2, where an excess of events is observed. As indicated by the Monte Carlo studies, this excess can be explained by elastically scattered protons hitting the beam pipe and inducing showers which are registered by the counters. Therefore, in the following the PRT2p counters will only be used to veto inelastic events with $p_T^2 < 0.3$ GeV^2.

The cuts used to identify proton-dissociative events are then the following:

- a tag in PRT1 or
- a tag in PRT2p for $p_T^2 < 0.3$ GeV^2 or
- energy deposition in FCAL: $E_{FCAL} > 1.0$ GeV or more than 0.3 GeV in the two FCAL rings surrounding the beam pipe.

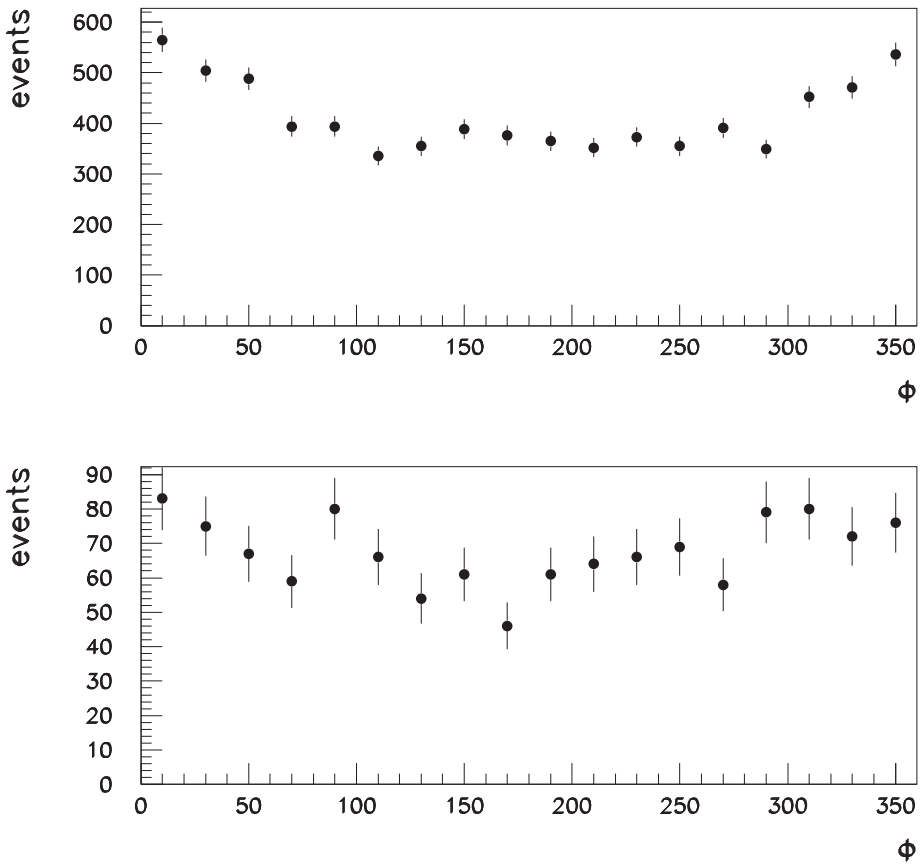

Figure 4.8: *Azimuth angle distribution of the ρ^0 for events with a tag in PRT2p in the range $p_T^2 < 1.0$ GeV^2 (upper plot) and $p_T^2 \geq 1.0$ GeV^2 (lower plot).*

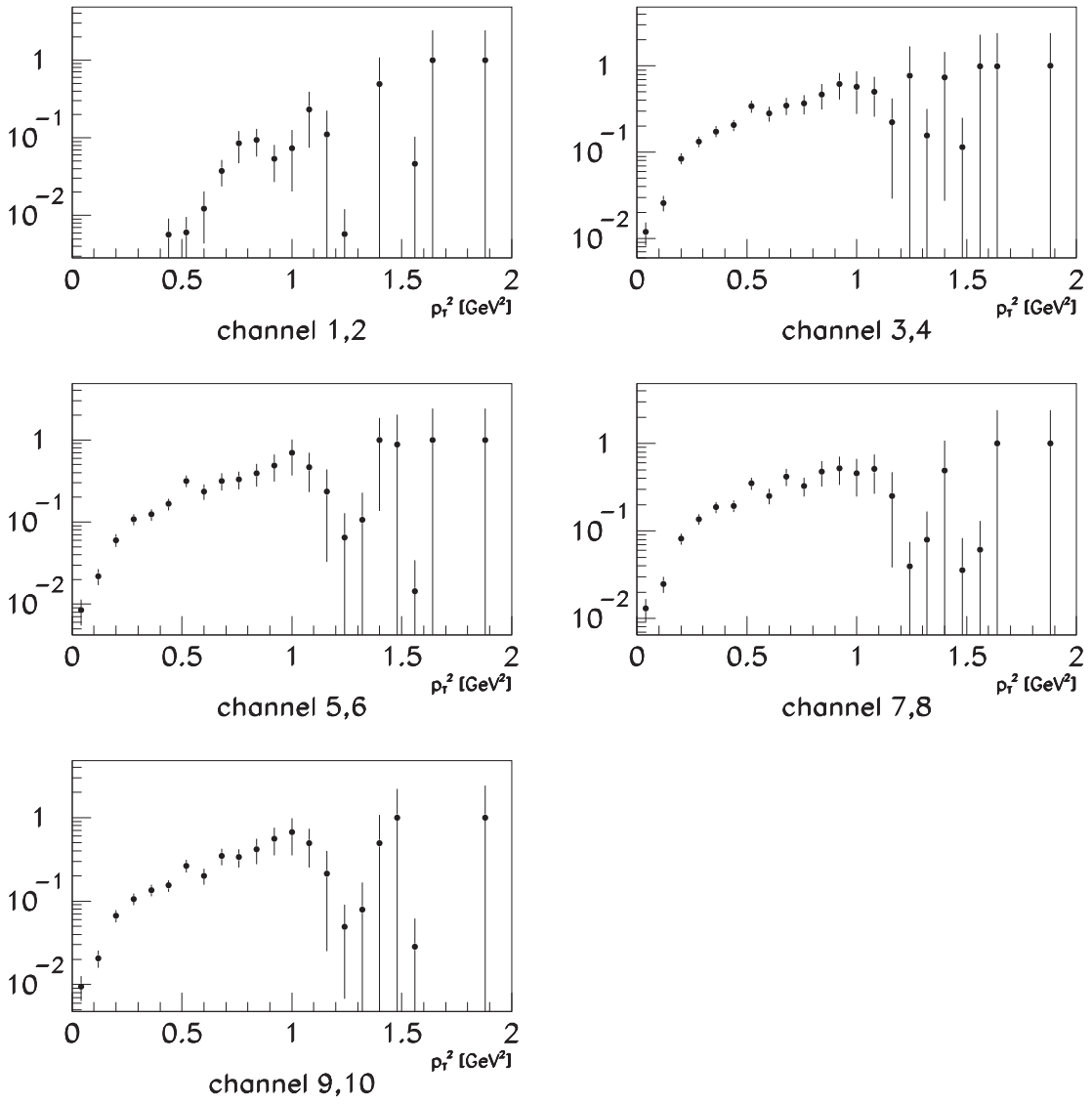

Figure 4.9: *p_T^2 acceptance of the PRT2 counters for Monte Carlo events with an elastically scattered proton. With the exception of counters (1,2) the contribution from elastic events becomes non-negligible for $p_T^2 \gtrsim 0.2\ GeV^2$.*

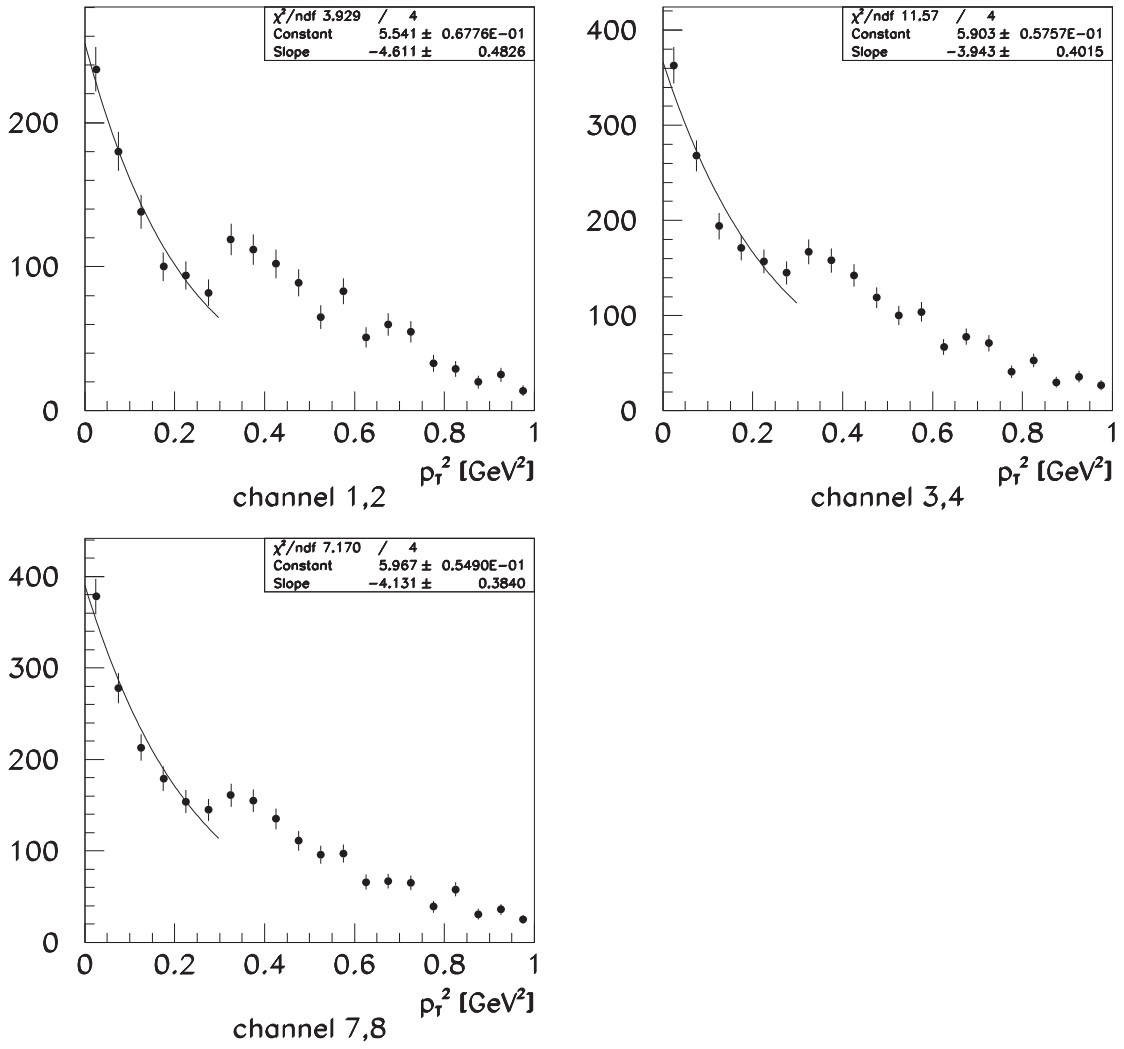

Figure 4.10: p_T^2 *distribution of physics events with applied FCAL and PRT1 veto and a hit in the PRT2p counters.*

4.3 Correction Procedures

The numbers of elastic and proton-dissociative events selected with the above described procedure have to be corrected since events may get lost due to inefficiencies of the detector and the selection cuts.

The observed reactions are $\gamma p \to \pi^+\pi^- N$ from which events $\gamma p \to p\rho^0$ have to be selected. The measured sample is contaminated with non-resonant $\pi^+\pi^-$ production which has to be subtracted.

The remaining ρ^0 events have to be corrected for inefficiencies of PRT and FCAL. This procedure is described in Chap. 5.

In addition the proton-dissociative sample tagged by PRT has to be corrected for accidental coincidences in the PRT counter pairs as described above.

Finally, the remaining samples have to be corrected for the combined acceptance of the detector and the trigger. In Chap. 6 this procedure is described in detail.

Chapter 5

Determination of the PRT Tagging Efficiency

In this analysis the PRT is used to separate proton-dissociative events from elastic events in a ρ^0 photoproduction sample selected by the cuts introduced in Chap. 4. The selection cuts require events with exactly two oppositely charged tracks and no excess energy deposition in CAL which is not consistent with these tracks. Proton-dissociative events with high mass M_N, which would cause tracks with positive rapidity in CTD and energy deposition in FCAL are excluded by these cuts from the remaining sample. However, the sample may contain an unknown number of proton dissociative events which need to be identified with the help of the PRT. It is therefore necessary to understand to which extent the PRT can serve to identify proton dissociative events in the low mass M_N region. The probability ε that a proton-dissociative ρ^0 production event will be detected is called the tagging efficiency in the following. It will be shown that the tagging efficiency ε is not a constant but is a function $\varepsilon(t)$.

In the following we determine the PRT tagging efficiency from physics data. This will be done for the individual detectors PRT1 and PRT2p and combinations with and without FCAL. It is assumed that the $|t|$ distributions of both reactions show an exponential fall-off. It has been shown in previous measurements that the elastic reaction has a much steeper t-slope than its proton-dissociative (or inelastic) counter part. [47]

To compute the tagging efficiency of a detector the following assumption is made: Elastic reactions $ep \to ep\rho^0$ do not show tags in either PRT or energy deposition in FCAL since the elastically scattered proton remains in the beam pipe. We use the

notation N_e for the number of elastic events in a given sample.

Inelastic reactions $ep \to eN\rho^0$ can be identified if particles originating from the outgoing nucleon system N hit FCAL or any PRT counter. Due to the incomplete acceptance of the counters it is possible that these particles miss the detector and in this case inelastic reactions cannot be distinguished from elastic reactions. The number of inelastic detected reactions is denoted as $N_\mathrm{i}^\mathrm{meas}$, the number of inelastic undetected reactions is $N_\mathrm{i}^\mathrm{invis}$ and the total number of inelastic events is $N_\mathrm{i} = N_\mathrm{i}^\mathrm{meas} + N_\mathrm{i}^\mathrm{invis}$.

5.1 Tagging Efficiency $\varepsilon(t)$ for $|t| < 0.6\,\mathbf{GeV}^2$

For small values of $|t|$ the differential cross section and accordingly the number of events per $|t|$ bin can be parameterized in the following way:

$$\text{elastic: } \frac{dN_\mathrm{e}}{d|t|} = N_e e^{-b_e|t|}, \tag{5.1}$$

$$\text{inelastic: } \frac{dN_\mathrm{i}}{d|t|} = N_i e^{-b_i|t|} = N_\mathrm{i}^\mathrm{meas} e^{-b_i|t|} + N_\mathrm{i}^\mathrm{invis} e^{-b_i|t|}. \tag{5.2}$$

The tagging efficiency ε for the reaction $ep \to eN\rho^0$ of a counter in a given $|t|$-interval can then be defined as the fraction of all inelastic events with a tag in this counter:

$$\varepsilon = \frac{N_\mathrm{i}^\mathrm{meas}(|t|)}{N_\mathrm{i}(|t|)} = \frac{N_\mathrm{i}^\mathrm{meas}(|t|)}{N_\mathrm{i}^\mathrm{meas}(|t|) + N_\mathrm{i}^\mathrm{invis}(|t|)}. \tag{5.3}$$

The first approach is to study the $|t|$ dependence of the ratio $f(|t|)$ of all elastic and inelastic events N_all to the number of measured inelastic events $N_\mathrm{i}^\mathrm{meas}$:

$$\begin{aligned} f(|t|) = \frac{N_\mathrm{all}(|t|)}{N_\mathrm{i}^\mathrm{meas}(|t|)} &= \frac{N_\mathrm{i}^\mathrm{meas} e^{-b_i|t|} + N_\mathrm{i}^\mathrm{invis} e^{-b_i|t|} + N_\mathrm{e} e^{-b_e|t|}}{N_\mathrm{i}^\mathrm{meas} e^{-b_i|t|}} \\ &= \frac{N_\mathrm{i}^\mathrm{meas} + N_\mathrm{i}^\mathrm{invis}}{N_\mathrm{i}^\mathrm{meas}} + \frac{N_\mathrm{e}}{N_\mathrm{i}^\mathrm{meas}} e^{-\Delta b|t|} \\ &= \frac{1}{\varepsilon} + \frac{N_\mathrm{e}}{N_\mathrm{i}^\mathrm{meas}} e^{-\Delta b|t|} \qquad \text{with } \Delta b = b_e - b_i \end{aligned} \tag{5.4}$$

The data points are fitted with the function:

$$f(|t|) = 1/P_1 + P_2 e^{-P_3|t|} \tag{5.5}$$

in the range $0 < |t| < 0.6$ GeV^2 with the fit parameters $P_1 = \varepsilon$, $P_2 = N_\mathrm{e}/N_\mathrm{i}^\mathrm{meas}$ and $P_3 = \Delta b$. In this way the difference between the elastic and the inelastic t-slope

$\Delta b = b_e - b_i$ can be determined. In Sec. 7.2 the t distributions of the elastic and the inelastic data samples are studied separately.

To determine the tagging efficiency of PRT1 and PRT2p separately, six different tagging modes are studied. Inelastic reactions of the type $ep \to eN\rho^0$ are detected by a tag either in:

(a) PRT1 only, while PRT2p and FCAL are ignored;

(b) PRT2p only, while PRT1 and FCAL are ignored;

(c) FCAL only, ignoring PRT1, PRT2p;

(d) PRT1 .or. PRT2p, ignoring FCAL;

(e) PRT1 .or. energy deposition in FCAL;

(f) PRT1 .or. PRT2p .or. FCAL, to tag as many inelastic reactions as possible.

Since PRT2p is sensitive to elastically scattered protons for $|t| > 0.3$ GeV^2, the fits to data including PRT2p are limited to $|t| < 0.3$ GeV^2. Fig. 5.1 shows the plots for the six tagging modes. Superimposed are fits according to Eq. 5.5. As a check on systematics the fits were repeated excluding the data point in the range $0 < |t| < 0.05$ GeV^2, which is the bin that may be affected by low M_N mass effects (Fig. 5.2). Tables 5.1 and 5.2 list the values of the fit parameters ε, N_e/N_i^{meas} and Δb. To check the dependence of the fit parameters on the chosen t range all fits were also repeated in the range $0 < |t| < 1.0$ GeV^2 and $0.05 < |t| < 1.0$ GeV^2 and the results are summarized in Tab. 5.3.

For $|t| = 0$ the second term in Eq. 5.4 is

$$R_{meas} = N_e/N_i^{meas} \tag{5.6}$$

and the ratio R of elastic to inelastic events is then given by

$$R = \frac{N_e \varepsilon}{N_i^{meas}} = P_1 P_2 \tag{5.7}$$

which is also shown in Tabs. 5.1, 5.2 and 5.3.

The values of R and of Δb as determined by the different tagging modes are consistent within errors for the two fit ranges. The spread of values is used to estimate the systematic errors.

tagging mode	ε	N_e/N_i^{meas}	R	Δb [GeV^{-2}]
PRT1	0.56 ± 0.06	8.0 ± 0.3	4.5 ± 0.5	5.4 ± 0.5
PRT2p	0.44 ± 0.05	8.3 ± 0.5	3.7 ± 0.5	5.2
FCAL	0.40 ± 0.04	11.7 ± 0.5	4.6 ± 0.5	5.9 ± 0.6
PRT1 .or. PRT2p	0.81 ± 0.10	6.7 ± 0.3	5.4 ± 0.7	5.2
PRT1 .or. FCAL	0.61 ± 0.06	7.1 ± 0.3	4.3 ± 0.5	5.2 ± 0.5
PRT1 .or. PRT2p .or. FCAL	0.77 ± 0.09	6.0 ± 0.3	4.7 ± 0.6	5.2

Table 5.1: *Parameters of the fit according to Eq. 5.5 in the range* $|t| < 0.6$ *GeV*^{2} *for six different tagging modes (see Fig. 5.1). The ratio between elastic and proton-dissociative events* $R = \varepsilon N_e/N_i^{meas} = N_e/N_i$ *for* $|t| = 0$ *is given. Fits to data including PRT2p are performed for* $|t| < 0.3$ *GeV*^{2}*, only, with the fit parameter* Δb *fixed to 5.2 GeV*$^{-2}$*.*

tagging mode	ε	N_e/N_i^{meas}	R	Δb [GeV^{-2}]
PRT1	0.67 ± 0.14	7.3 ± 0.4	4.9 ± 1.0	4.4 ± 0.6
PRT2p	0.47 ± 0.07	8.6 ± 0.8	4.0 ± 0.7	5.2
FCAL	0.46 ± 0.08	10.4 ± 0.6	4.8 ± 1.0	4.8 ± 0.7
PRT1 .or. PRT2p	0.76 ± 0.11	6.5 ± 0.5	5.0 ± 0.8	5.2
PRT1 .or. FCAL	0.72 ± 0.14	6.6 ± 0.3	4.7 ± 1.0	4.3 ± 0.6
PRT1 .or. PRT2p .or. FCAL	0.72 ± 0.09	5.9 ± 0.4	4.2 ± 0.6	5.2

Table 5.2: *Parameters of the fit according to Eq. 5.5 as in Tab. 5.1, but for* $|t| \geq 0.05$ *GeV*^{2} *(see Fig. 5.2).*

t range [GeV^2]	tagging mode	ε	N_e/N_i^{meas}	R	Δb [GeV^{-2}]
$0.0 < t < 1.0$	PRT1	0.66 ± 0.03	7.9 ± 0.3	5.3 ± 0.3	4.7 ± 0.3
	FCAL	0.54 ± 0.03	11.4 ± 0.5	6.2 ± 0.4	4.7 ± 0.3
	PRT1 .or. FCAL	0.73 ± 0.04	7.1 ± 0.2	5.2 ± 0.3	4.5 ± 0.3
$0.05 < t < 1.0$	PRT1	0.70 ± 0.04	7.3 ± 0.3	5.1 ± 0.4	4.2 ± 0.3
	FCAL	0.59 ± 0.05	10.2 ± 0.5	6.0 ± 0.6	4.0 ± 0.3
	PRT1 .or. FCAL	0.78 ± 0.05	6.5 ± 0.3	5.0 ± 0.4	4.0 ± 0.3

Table 5.3: *Parameters of the fit according to Eq. 5.5 as in Tab. 5.1, but for* $|t| \leq 1.0\ GeV^2$.

The best estimated values of R and Δb are determined from the tagging mode PRT1 .or. FCAL (see Tab. 5.1) and their systematic errors are obtained from fitting PRT1, PRT2p and FCAL data separately. In addition the results of the fits done in the range $0.05 < |t| < 0.6$ GeV^2 (see Tab. 5.2) are taken into account and the results are

$$\begin{aligned} R &= 4.3 \pm 0.5\,(\text{stat.}) \pm 0.6\,(\text{syst.}), \\ \Delta b &= 5.2 \pm 0.5\,(\text{stat.}) \pm 0.5\,(\text{syst.}). \end{aligned} \tag{5.8}$$

This value of Δb is used as a fixed parameter to fit the PRT2p data for $|t| < 0.3$ GeV^2.

The tagging efficiency ε in the range $|t| < 0.6$ GeV^2 using PRT1 .or. FCAL is $\varepsilon = 0.61 \pm 0.06$ (see Tab. 5.1). The fit excluding the range $|t| < 0.05$ GeV^2 yields the tagging efficiency for the same tagging mode $\varepsilon' = 0.72 \pm 0.14$. Therefore, the value $\varepsilon = 0.61 \pm 0.06$ has to be treated as a lower limit and a systematic error of +20% has to be taken into account in the analysis.

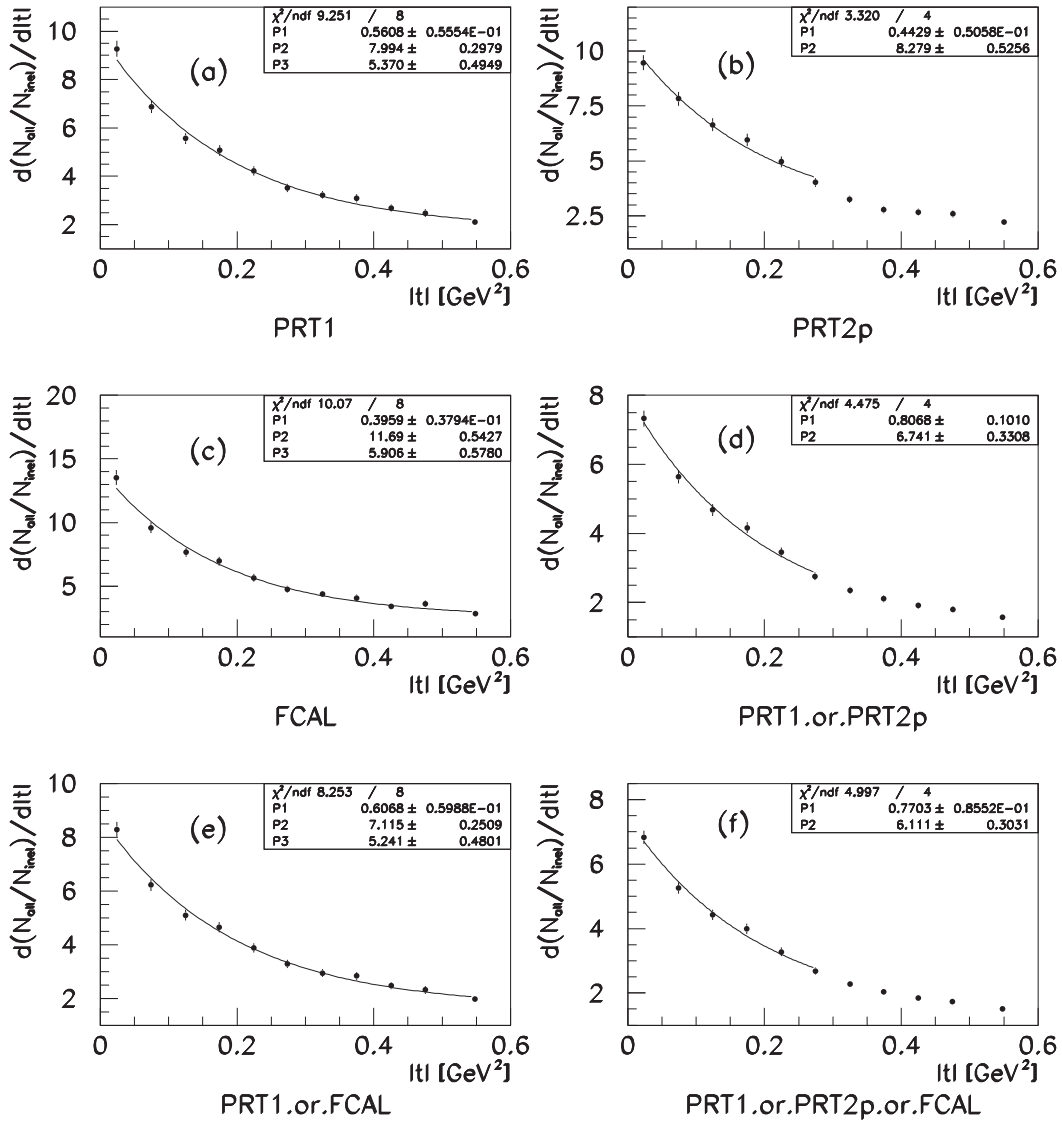

Figure 5.1: *Inverse fraction of inelastic ρ^0 events with tag in PRT1 only (a), PRT2p only (b), FCAL only (c), PRT1 .or. PRT2p (d), PRT1 .or. FCAL (e) and PRT1 .or. PRT2p .or. FCAL (f). Superimposed is a fit according to Eq. 5.5 in the range* $0 < |t| < 0.6$ *GeV*^{2}.

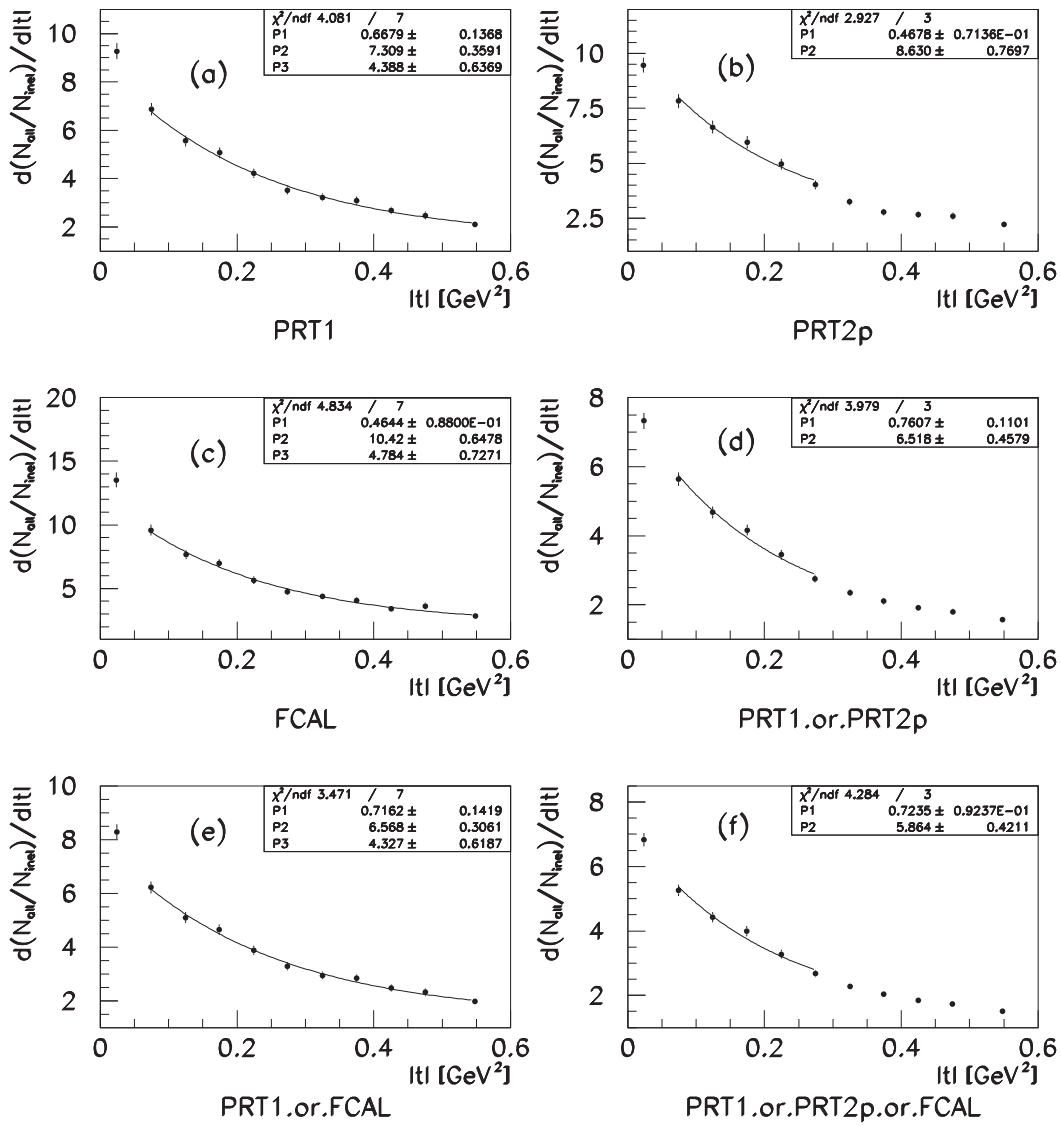

Figure 5.2: *Same plots as in Fig. 5.1, but fitted in the range* $0.05 < |t| < 0.6\ GeV^2$.

5.2 Tagging Efficiency $\varepsilon(t)$ for $|t| > 0.6\,\mathbf{GeV}^2$

In a second approach the tagging efficiencies of PRT1 and FCAL are estimated from events with large values of $|t|$. Fig. 5.3 shows the fraction $\frac{N_{\mathrm{i}}^{\mathrm{meas}}(|t|)}{N_{\mathrm{all}}(|t|)}$ of ρ^0 events with a tag in PRT1, FCAL and their combination in the range $0 < |t| < 3.5$ GeV^2. We use the fact that the differential cross section of the elastic reaction $d\sigma_{el}/d|t|$ has a much steeper $|t|$ slope than in the inelastic case. Therefore, at high values of $|t|$ inelastic reactions dominate and the tagging efficiency of a counter is approximately given by the fraction of events with a tag $N_{\mathrm{i}}^{\mathrm{meas}}/N_{\mathrm{all}}$. Using Eq. 5.4, the tagging efficiency ε can be expressed as:

$$\varepsilon = \frac{1}{\frac{N_{\mathrm{all}}(|t|)}{N_{\mathrm{i}}^{\mathrm{meas}}(|t|)} - \frac{N_{\mathrm{e}}}{N_{\mathrm{i}}^{\mathrm{meas}}} e^{-\Delta b|t|}}. \tag{5.9}$$

Consequently, the values plotted in Fig. 5.3 have to be corrected using the term $c = \frac{N_{\mathrm{e}}}{N_{\mathrm{i}}^{\mathrm{meas}}} e^{-\Delta b|t|}$ in order to be interpreted as the tagging efficiency ε. The term c is calculated using the results given in Tab. 5.1, $\Delta b = 5.2$ GeV^{-2} and $N_{\mathrm{e}}/N_{\mathrm{i}}^{\mathrm{meas}} = 7.1$. For $|t| = 1$ GeV^2 one gets $c = 0.04$ which translates into a 2% correction of ε. For values of $|t| = 1.5$ GeV^2 and higher this correction becomes much smaller than the errors. Fig. 5.4 shows the values for ε of PRT1, FCAL and their combination obtained in this way for $|t| = 1.0, 1.5$ and 2.0 GeV^2. In addition the results from Tab. 5.1 are plotted at the mean value of the studied $|t|$ interval. The tagging efficiency of PRT1 .or. FCAL rises with $|t|$ for $0 < |t| < 2.0$ GeV^2, it can be fitted to the form

$$\varepsilon(|t|) = 1.0 - 0.45 \exp\left(\frac{-0.75|t|}{\mathrm{GeV}^2}\right). \tag{5.10}$$

Table 5.4 summarizes the resulting tagging efficiencies ε of PRT1, PRT2p and FCAL obtained from the fits (Eq. 5.4) and for the high $|t|$ values.

The tagging efficiency of PRT1, FCAL and their combination PRT1 .or. FCAL was also studied with Monte Carlo events. Fig. 5.5 shows the fraction of proton-dissociative MC events that were tagged with those counters. Tab. 5.5 summarizes the efficiencies $\varepsilon_{\mathrm{MC}}$ obtained by fitting the function $\varepsilon_{\mathrm{MC}} = a + b|t|$ in the range $0 < |t| < 2.0$ GeV^2. The $\varepsilon_{\mathrm{MC}}(|t|)$-distributions are independent of $|t|$ within errors. The tagging efficiencies obtained by Monte Carlo are significantly higher than the ones given in Tab. 5.1.

$\|t\|$ range [GeV^2]	PRT1	PRT2p	FCAL	PRT1 .or. FCAL
0 – 0.3		0.44 ± 0.05		
0 – 0.6	0.56 ± 0.06		0.40 ± 0.05	0.61 ± 0.06
0 – 1.0	0.66 ± 0.03		0.54 ± 0.03	0.73 ± 0.04
0.8 – 1.2	0.67 ± 0.05		0.55 ± 0.05	0.75 ± 0.03
1.3 – 1.8	0.81 ± 0.06		0.67 ± 0.06	0.85 ± 0.05
1.8 – 3.5	0.85 ± 0.07		0.73 ± 0.07	0.92 ± 0.04

Table 5.4: *Tagging efficiencies from physics data of PRT1, PRT2p, with and without FCAL. The values for $|t| \leq 0.6$ GeV^2 are obtained from Tab. 5.1. The values for $|t| \geq 1.0$ GeV^2 are from Eq. 5.9.*

	$\varepsilon_{\mathrm{MC}}$
PRT1	0.73 ± 0.05
FCAL	0.77 ± 0.05
PRT1 .or. FCAL	0.88 ± 0.05

Table 5.5: *Tagging efficiencies ε_{MC} obtained from proton-dissociative Monte Carlo data. (see Fig. 5.5)*

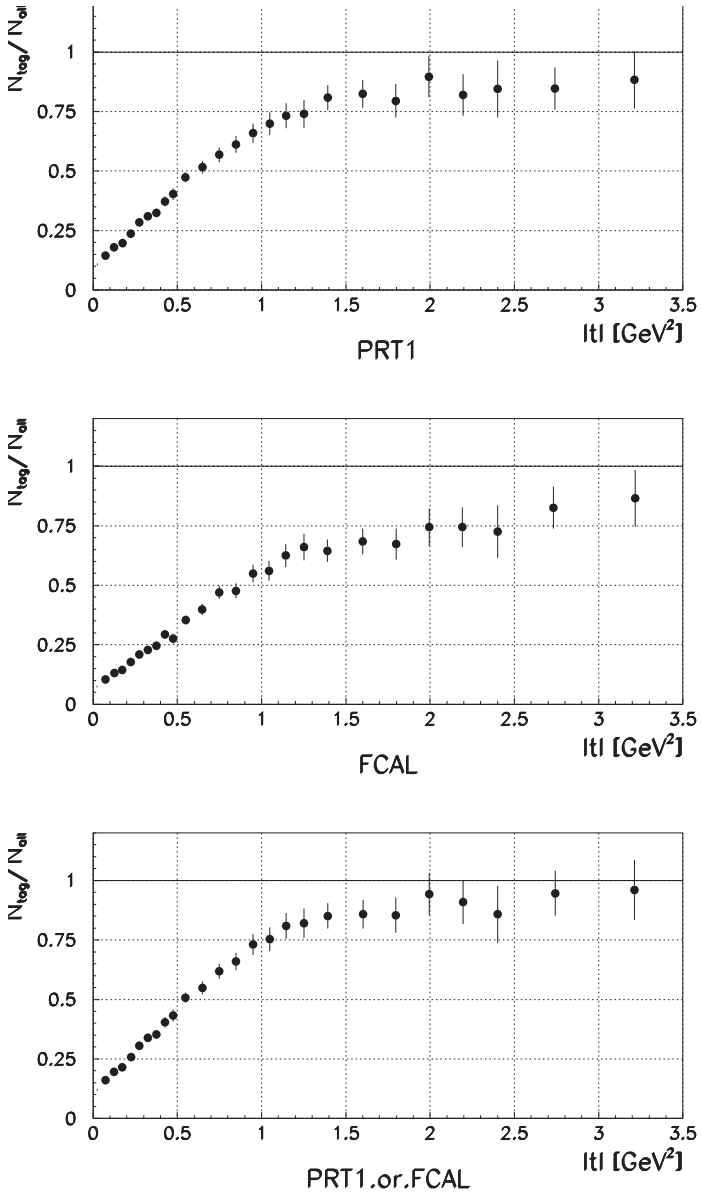

Figure 5.3: *Fraction of ρ^0 events with a tag in PRT1 (a), FCAL (b) and PRT1 .or. FCAL (c).*

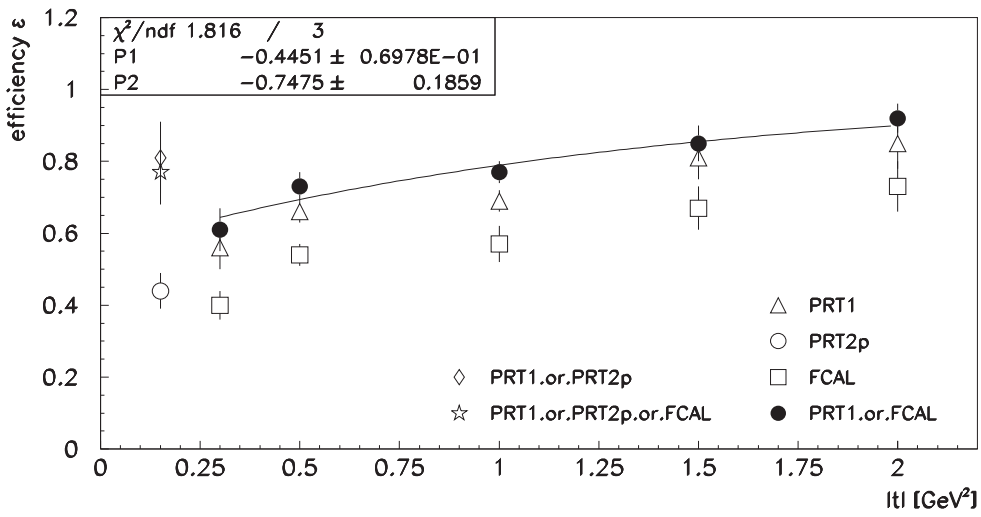

Figure 5.4: *Tagging efficiency ε of PRT1, PRT2p, FCAL and their combinations versus $|t|$. The points obtained by the fits in Fig. 5.1 are mapped at the respective mean value of the fitted $|t|$ range. Also shown is the fit to the PRT1 .or. FCAL points according to Eq. 5.10.*

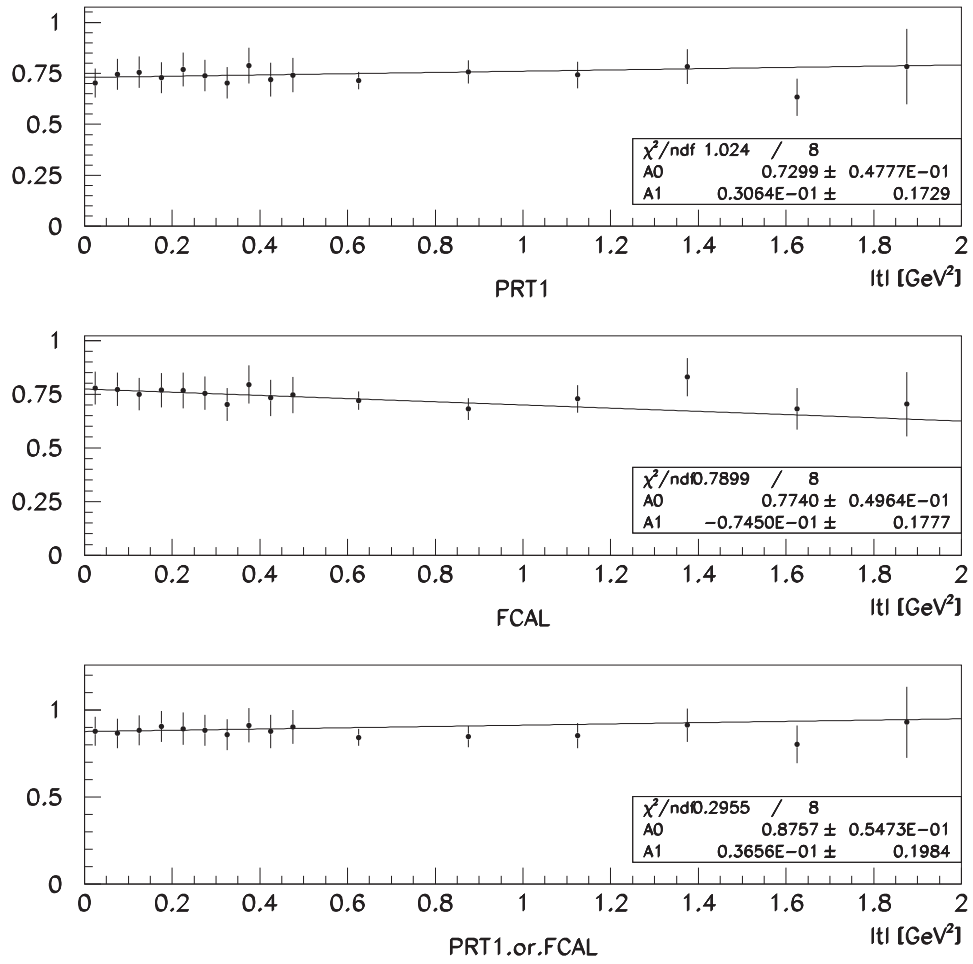

Figure 5.5: *Tagging efficiency ε_{MC} of proton-dissociative Monte Carlo events tagged with PRT1, FCAL and the combination PRT1 .or. FCAL. The solid lines are fits of the form $\varepsilon_{MC(|t|)} = a + b|t|$ in the range $0 < |t| < 2.0\ GeV^2$.*

Chapter 6

Acceptance

In this chapter the acceptance of the event selection and the reconstruction procedures is studied using Monte Carlo events. The event generator EPSOFT [28] was used to generate elastic and proton-dissociative ρ^0 photoproduction events. This program was developed within the HERWIG framework [31]; it simulates γp interactions based on VMD and Regge theory [11, 24]. The generated events were passed through the ZEUS detector and trigger simulations, MOZART and ZGANA, which perform the event reconstruction using the same code that is used to reconstruct physics data.

To compare the Monte Carlo events with data taken during physics runs they were generated in the following kinematic range: The invariant mass of the 2-pion system was generated in the range $2m_\pi \leq m_{\pi^+\pi^-} \leq 1.3$ GeV. The generated photon-proton center of mass energy was $60 < W_{\gamma p} < 140$ GeV. To reflect the properties of the Photoproduction Tagger in terms of Q^2 the events were generated in the range $0 < Q^2 < 0.02$ GeV^2. The differential cross sections in $|t|$ were generated as $d\sigma/d|t| \sim e^{-b|t|}$; to get a reasonable number of events at $|t|$ up to values ~ 1.0 GeV^2 the $|t|$ distributions were generated flatter than the measured distributions and were then reweighted to the desired shape. In the elastic case the $|t|$ distribution was reweighted to $d\sigma_{\rm el}/d|t| \sim e^{-b_e|t|+c_e t^2}$ as suggested by earlier measurements with values b_e, c_e given below.

The slope b_e and curvature c_e of the elastic reaction $ep \to ep\pi^+\pi^-$ with the $\pi^+\pi^-$ mass in the ρ^0 region were measured by ZEUS as $b_e = 11.4 \pm 0.3\,(\text{stat.})^{+0.3}_{-0.5}\,(\text{syst.})$ GeV^{-2} and $c_e = 2.8 \pm 0.7\,(\text{stat.})^{+1.2}_{-1.8}\,(\text{syst.})$ GeV^{-4}[47]. The reweighted generated and the reconstructed $|t|$ distributions are shown in plots (a, b) of Fig. 6.1 with fits of the form $dN_0/d|t| = N\exp(-b|t| + ct^2)$. The generated $|t|$ distribution was reweighted such that the parameters b_e and c_e of the reconstructed distribution are in good agreement with

the uncorrected measured $|t|$ distributions.

The slope b_i of the proton-dissociative reaction has been measured as $b_i = 5.8 \pm 0.3\,(\text{stat.}) \pm 0.5(\text{ syst.})$ GeV^{-2}[47]. The generated and reconstructed $|t|$ distributions are shown in plots (c, d) of Fig. 6.1 with single exponential fits $dN_0/d|t| = N \exp(-b_i|t|)$. In those fits the first bin $0 < |t| < 0.02$ GeV^2 is excluded since in this $|t|$ interval the distribution deviates from an exponential function. The lack of events at very small values of $|t|$ can be explained by the fact that a minimum squared four-momentum $|t|_{\text{min}}$ has to be transfered to the proton to produce an excited state N with mass M_N. It can be shown that $|t|_{\text{min}}$ is

$$|t|_{\text{min}} = \frac{|(m_\rho^2 + Q^2)(M_N^2 - M_p^2)|}{W^2} + \frac{\left(M_N^2 - M_p^2 + Q^2 + m_\rho^2\right) \cdot \left[M_p^2(Q^2 + m_\rho^2) - Q^2(M_N^2 - M_p^2)\right]}{W^4} \tag{6.1}$$

and for $M_N \approx 10$ GeV, $W = 90$ GeV, one finds $|t|_{\text{min}} \cong 0.006$ GeV^2.

Tab. 6.1 summarizes the fit parameters b_e, c_e and b_i for the generated and reconstructed Monte Carlo events.

	fit parameter	generated	reconstructed
$\gamma p \to \rho^0 p$	b_e [GeV^{-2}]	12.3 ± 0.2	9.1 ± 0.5
	c_e [GeV^{-4}]	5.4 ± 0.3	3.5 ± 1.2
$\gamma p \to \rho^0 N$	b_i [GeV^{-2}]	4.0 ± 0.1	2.4 ± 0.2

Table 6.1: *Fit parameters of the generated and reconstructed $|t|$ distributions of the elastic and proton-dissociative Monte Carlo events.*

The combined acceptance A of the ρ^0 trigger and the selection cuts described above is calculated as follows:

$$A(|t|) = \frac{N_{\text{rec}}(|t|)}{N_{\text{gen}}(|t|)}, \tag{6.2}$$

with the number of generated events N_{gen} at a given $|t|$ value and the number of reconstructed events N_{rec} in a given $|t| = p_T^2$ bin. The acceptances obtained this way are shown in Fig. 6.2, plot (a) and (b) for the elastic and the proton-dissociative reaction, respectively. The superimposed fits are exponential functions $P_1 \exp P_2|t|$, which describe the distributions well, with the exception of the first bin in the proton-dissociative case. There, the exponential correction will be used for values of $|t| > 0.02$ GeV^2 and the bin $|t| < 0.02$ GeV^2 will be corrected separately. The bottom

plot of Fig. 6.2 shows the ratio between the acceptance of the proton-dissociative and the elastic events $\varepsilon_{\text{inel}}/\varepsilon_{\text{el}}$ with a superimposed linear fit $A_0 + A_1|t|$ with parameters $A_0 = 1.10 \pm 0.12$, $A_1 = (-1.06 \pm 0.55)$ GeV^{-2}.

The upper plot of Fig. 6.3 shows the W distributions from physics data and reconstructed Monte Carlo data for the elastic reaction for $|t| < 0.5$ GeV^2. This comparison was done between physics data after applying the elastic selection cuts to the elastic Monte Carlo data sample. Here it is assumed that the remaining proton-dissociative events after applying those cuts can be neglected. The Monte Carlo simulation describes the experimental data well within the statistical errors.

In a second check the proton-dissociative events and Monte Carlo data are being compared the same way. Here, a reasonable agreement between Monte Carlo and experimental data was found.

In the next chapter the acceptance shown in Fig. 6.2 and the PRT tagging efficiency obtained in Chap. 5 are used as separate correction procedures to calculate the results from the measured data.

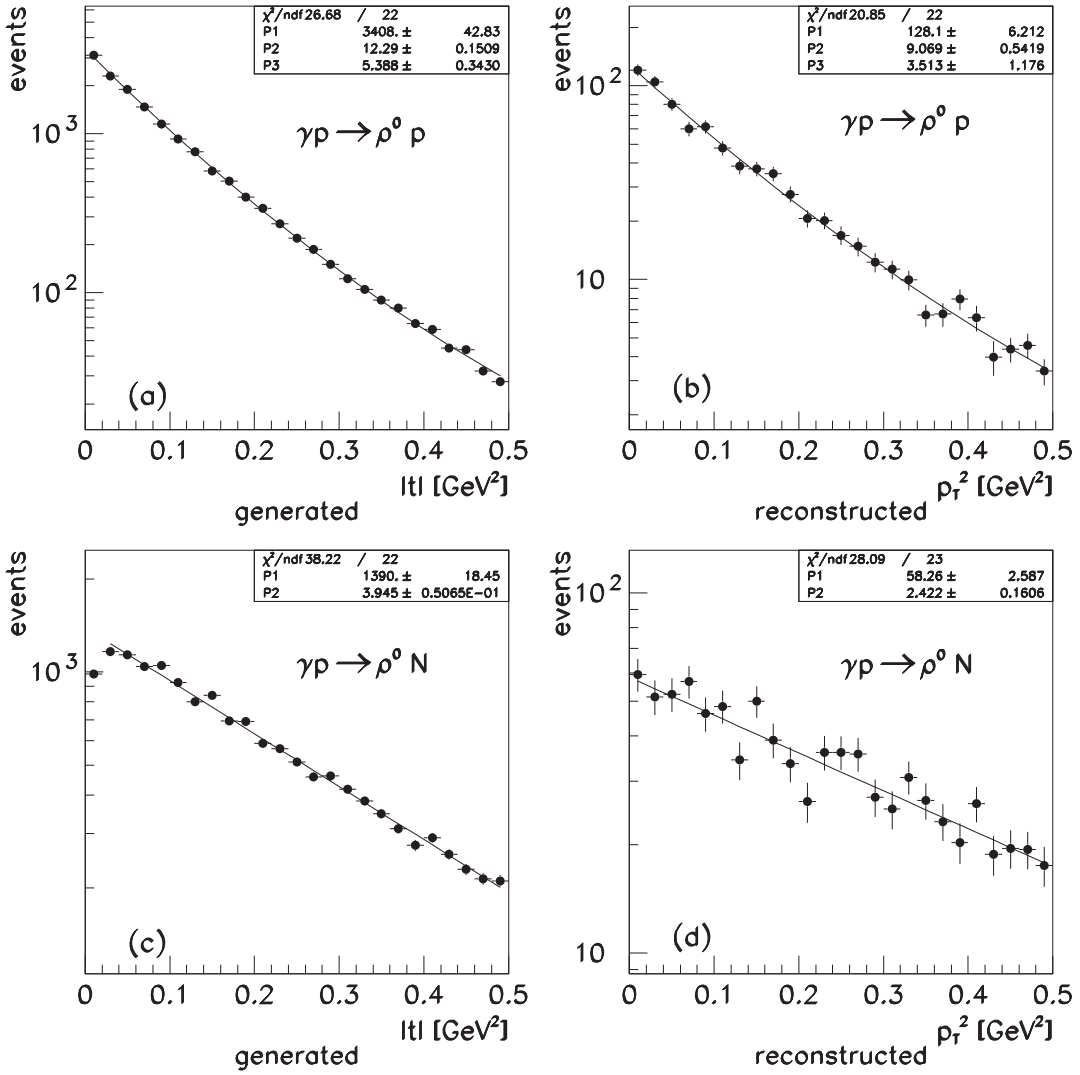

Figure 6.1: *Monte Carlo generated $|t|$ and reconstructed p_T^2 distributions for the elastic (plots a, b) and the proton-dissociative (plots c, d) Monte Carlo. The solid lines show fits of the form $N_0 e^{-b|t|+ct^2}$ (elastic) and $N_0 e^{-b|t|}$ (proton-dissociative) to the Monte Carlo data points.*

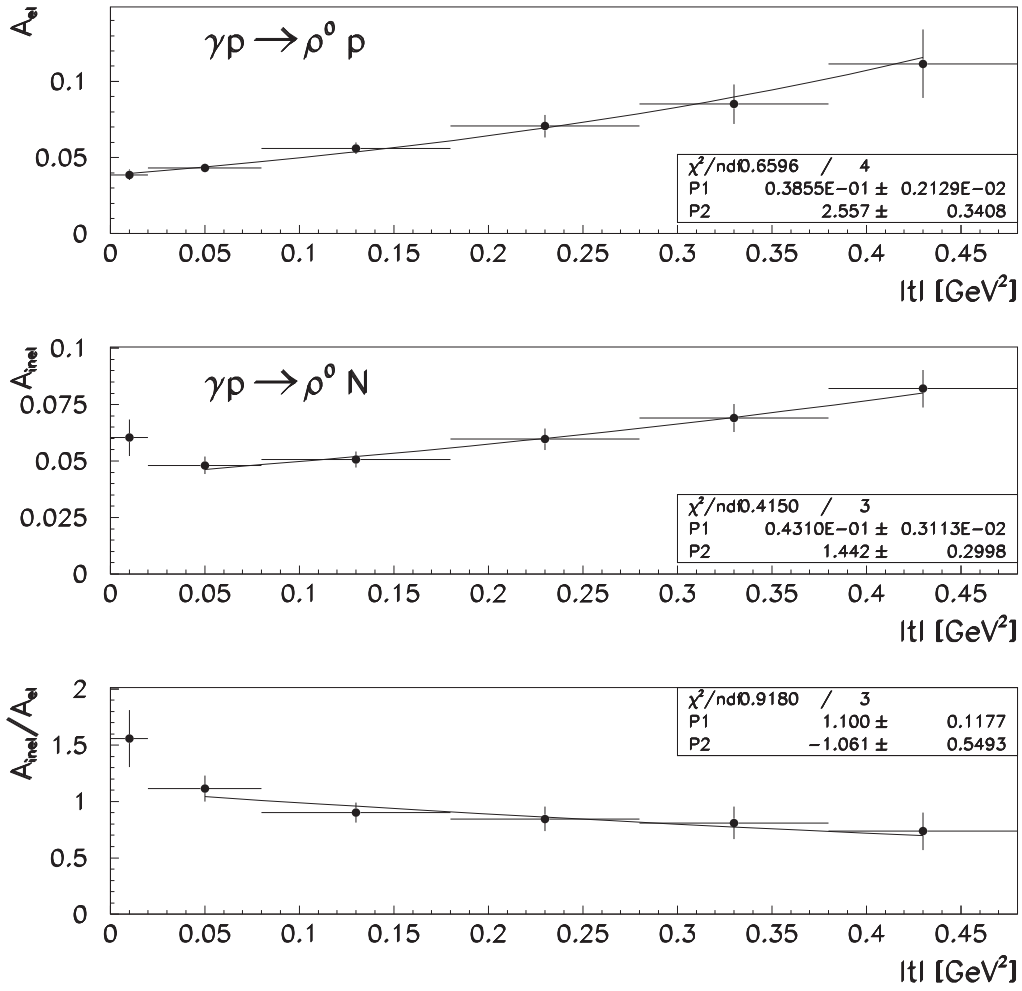

Figure 6.2: *Acceptance $A(|t|)$ of the trigger and the selection cuts for elastic (A_{el}, upper plot) and proton-dissociative (A_{inel}, middle plot) ρ^0 photoproduction events. The bottom plot shows the ratio A_{inel}/A_{el}. The superimposed fit functions are of the form $P_1 \exp P_2|t|$. A_{el} and A_{inel} are used as acceptance corrections for the measured elastic and proton-dissociative distributions, respectively.*

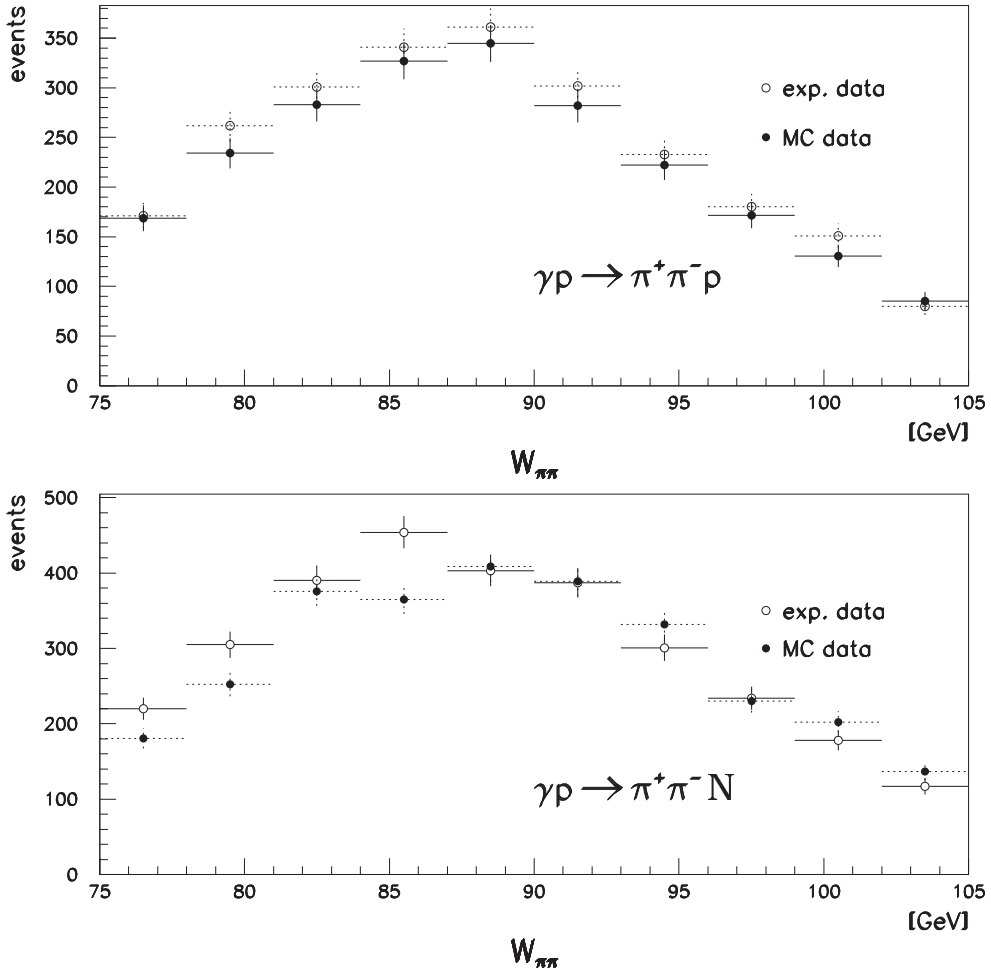

Figure 6.3: *W distributions of elastic events $\gamma p \rightarrow \rho^0 p$ (upper plot) and proton-dissociative events $\gamma p \rightarrow \rho^0 N$ (lower plot) from experimental data (bullets) and Monte Carlo (circles) for $|t| < 0.5\ GeV^2$.*

Chapter 7

Results

Using the cuts introduced in Sec. 4.1, PRT1, PRT2p and FCAL can be used to distinguish elastic from proton-dissociative events and study their differential cross sections $d\sigma/d|t|$. As mentioned in Sec. 4.1, the PRT2p counters are used to tag events with $|t| < 0.3$ GeV^2 only, while PRT1 and FCAL are used in the range $|t| < 0.5$ GeV^2. Indices e and i will be used to label parameters of elastic and proton-dissociative distributions, respectively.

7.1 Systematic Errors

The following sources of systematic errors have to be considered:

1. Influence of the cut on the minimum transverse momentum of the tracks.
2. Influence of the track $|\eta|$ cut.
3. Influence of the selected invariant $\pi^+\pi^-$ mass region.
4. Influence of the matching procedure between tracks and the energy in the calorimeter.
5. Error of the tagging efficiency.
6. Error of the acceptance due to the trigger and event selection cuts.

The errors of the first four items are small compared to those of the last two. Tab. 7.1 summarizes the variations of the the selection cuts and the resulting systematic errors

of the measured variables. Their influence partially cancels in the comparison of the elastic and the proton-dissociative reactions.

The error of the tagging efficiency was estimated in Chap. 5 by comparing the results of various approaches with different cuts. The systematic error on the tagging efficiency ε is $^{+20}_{-0}\%$.

The acceptance due to trigger and event selection is rather small and has a rather strong dependence on t, because at $W = 90$ GeV the opening angle of the ρ^0 decay pions is small and the pions tend to go into the beampipe undetected by CTD and CAL. The influence of the acceptance is therefore critical. To get an estimate, the numerical values of the acceptance at $t = 0$ and its t-dependence were changed in wide limits, and all the fits were repeated. Changing the acceptance at $t = 0$ by a factor of two gives the following estimates for the errors on the slopes and on the difference of elastic and proton-dissociative $|t|$ slopes:

$$\begin{aligned} \sigma_{b_e} &= 0.8 \text{ GeV}^{-2} \\ \sigma_{b_i} &= 0.6 \text{ GeV}^{-2} \\ \sigma_{\Delta b} &= 0.2 \text{ GeV}^{-2} \end{aligned} \tag{7.1}$$

For the error on the cross section ratio there is a partial cancellation of the influence of the acceptance, and a value of $\pm 6\%$ for the systematic error on the ratio is found.

7.2 Elastic $|t|$ Distribution

In this section the $|t|$ distribution of the elastic reaction $\gamma p \to \rho^0 p$ is studied. A double exponential function is used to obtain fits that describe the $|t|$ distributions of the $\pi^+\pi^-$ invariant mass in the ρ^0 mass region $0.55 < m_{\pi^+\pi^-} < 1.0$ GeV^{-2}:

$$\frac{dN}{d|t|} = Ne^{-b_e|t|+c_e t^2}, \tag{7.2}$$

with parameters slope b_e and curvature c_e.

cut	b_e [GeV^{-2}]	c_e [GeV^{-4}]	b_i [GeV^{-2}]	A	$\Delta b'$ [GeV^{-2}]	$b_{i,\mathrm{high}\,\lvert t\rvert}$ [GeV^{-2}]	$c_{i,\mathrm{high}\,\lvert t\rvert}$ [GeV^{-4}]
$p_T > 0.0$ GeV	11.37 ± 0.27	3.47 ± 0.68	4.08 ± 0.23	4.14 ± 0.29	5.68 ± 0.29	4.49 ± 0.18	0.94 ± 0.11
$p_T > 0.2$ GeV	12.89 ± 0.28	5.33 ± 0.74	4.54 ± 0.24	4.26 ± 0.28	5.85 ± 0.28	4.73 ± 0.19	1.13 ± 0.11
$\lvert\eta\rvert > 0.0$ GeV	12.30 ± 0.26	4.52 ± 0.67	4.52 ± 0.23	4.13 ± 0.27	5.65 ± 0.27	4.84 ± 0.18	1.12 ± 0.11
$0.60 < m_{\pi^+\pi^-} < 0.85$ GeV	12.54 ± 0.31	5.07 ± 0.80	4.45 ± 0.24	4.22 ± 0.30	5.83 ± 0.31	4.74 ± 0.19	1.08 ± 0.12
CAL-Track matching(*)	11.74 ± 0.26	3.93 ± 0.68	4.20 ± 0.22	3.98 ± 0.26	5.70 ± 0.27	4.57 ± 0.17	1.01 ± 0.11
this analysis $\pm$(stat.)	11.69 ± 0.27	3.71 ± 0.70	4.29 ± 0.22	4.14 ± 0.27	5.65 ± 0.28	4.66 ± 0.18	1.04 ± 0.11
systematic error	$^{+1.59}_{-0.32}$	$^{+2.28}_{-0.24}$	$^{+0.38}_{-0.23}$	$^{+0.14}_{-0.16}$	$^{+0.28}_{-0.0}$	$^{+0.11}_{-0.19}$	$^{+0.13}_{-0.10}$

Table 7.1: The systematic errors were studied using selection cuts modified as indicated and repeating the analysis. (*) The CAL-Track matching cuts were changed as follows: $E^{EMC}_{RCAL} < 240$ MeV, $E^{HAC}_{RCAL} < 300$ MeV and $E^{EMC}_{BCAL} < 360$ MeV. The individual deviations from the central values were added in quadrature to calculate the systematic errors of each quantity.

Plot (a) in Fig. 7.1 shows the uncorrected $|t|$ distribution of events which do not have a tag in PRT1 or energy deposition in FCAL and are therefore considered candidates for elastic events. Due to inefficiencies of PRT1 and FCAL this elastic sample is contaminated with a small fraction of proton-dissociative events, and the measured number of elastic events $N_{\mathrm{e}}^{\mathrm{meas}}$ has to be corrected according to:

$$N_{\mathrm{e}}^{\mathrm{corr}} = N_{\mathrm{e}}^{\mathrm{meas}} - \frac{(1-\varepsilon)}{\varepsilon} N_{\mathrm{i}}^{\mathrm{meas}} \tag{7.3}$$

where $N_{\mathrm{i}}^{\mathrm{meas}}$ denotes the measured number of proton-dissociative events and $N_{\mathrm{e}}^{\mathrm{corr}}$ the corrected number of elastic events. For the t-dependent tagging efficiency $\varepsilon(t)$ the result from Tab. 5.1, $\varepsilon = 0.61$, is used in the range $0 < |t| < 0.19$ GeV^2 and for $|t| > 0.19$ GeV^2 the fit according to Eq. 5.10.

Having applied the correction, the number of elastic events $dN_{\mathrm{e}}^{\mathrm{corr}}/d|t|$ can be described by a double exponential function $N \exp(-b_e|t| + c_e t^2)$ with the fit parameters $b_e = 9.1 \pm 0.3$ GeV^{-2} and $c_e = 3.7 \pm 0.7$ GeV^{-4} (see Fig. 7.2 (a)).

Next the acceptances of the trigger and the event selection according to Eq. 6.2 and as shown in Fig. 6.2 are applied. The results for the elastic reaction in the fitted range $0 < |t| < 0.5$ GeV^2 are shown in Fig. 7.3 (a). To study the influence of the tagging efficiency ε on the fit parameters b_e and c_e, its value was changed from $\varepsilon = 0.61$ to $\varepsilon' = 0.72$, as suggested by Tab. 5.2. Then the fit parameters found are

$$\begin{aligned} b'_e &= 11.4 \pm 0.2 \text{ GeV}^{-2} \\ c'_e &= 4.2 \pm 0.6 \text{ GeV}^{-4} \end{aligned}$$

The final result is then:

$$\begin{aligned} b_e &= 11.7 \pm 0.3 \text{ (stat.)}^{+1.8}_{-0.9} \text{ (syst.) GeV}^{-2} \\ c_e &= 3.7 \pm 0.7 \text{ (stat.)}^{+2.1}_{-0.2} \text{ (syst.) GeV}^{-4} \end{aligned}$$

The fit parameters are to be compared with results on the slope of the $\pi^+\pi^-$ mass state obtained earlier: $b_e = 11.4 \pm 0.3$ (stat.) $^{+0.3}_{-0.5}$ (syst.) GeV^{-2} and $c_e = 2.8 \pm 0.7$ (stat.) $^{+1.2}_{-1.8}$ (syst.) GeV^{-4} [43]. These slopes have been obtained for the $\pi^+\pi^-$ mass state in the ρ^0 mass region, and not for the ρ^0 meson properly. In principle they have to be corrected for background and interference effects to obtain the slope of ρ^0 production properly. This correction has not been done, because the effect of the correction is small, and of the same order as the uncertainty introduced by different methods of background subtraction.[43]

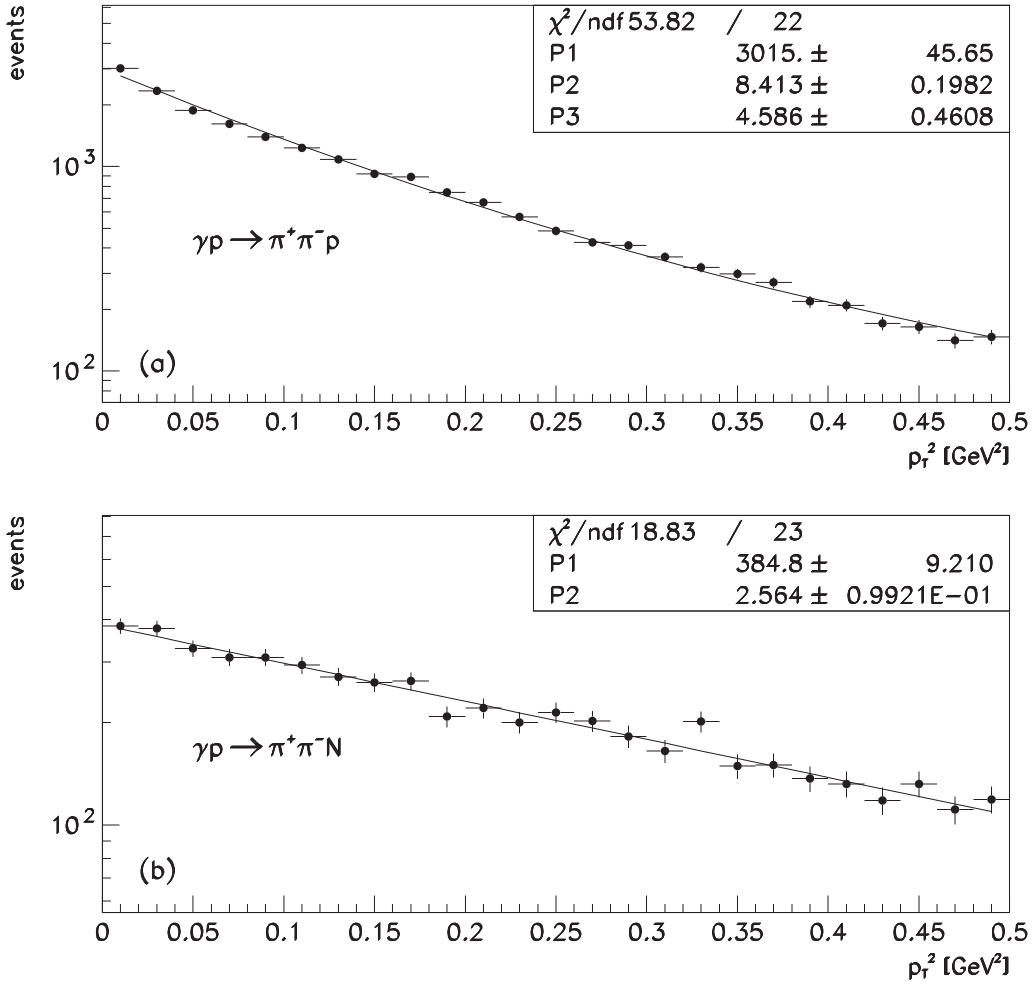

Figure 7.1: *Uncorrected differential cross sections $d\sigma/dp_T^2$ distribution of elastic candidates (plot a) and proton-dissociative (plot b) ρ^0 events in the range $0.55 < m_{\pi^+\pi^-} < 1.0$ GeV. Elastic events were selected with PRT1 and FCAL veto, proton-dissociative events with a tag in PRT1 .or. FCAL. Superimposed are the fit functions $N_{\pi\pi}e^{-bp_T^2+cp_T^{2\,4}}$ (plot a) and $N_{\pi\pi}e^{-bp_T^2}$ (plot b).*

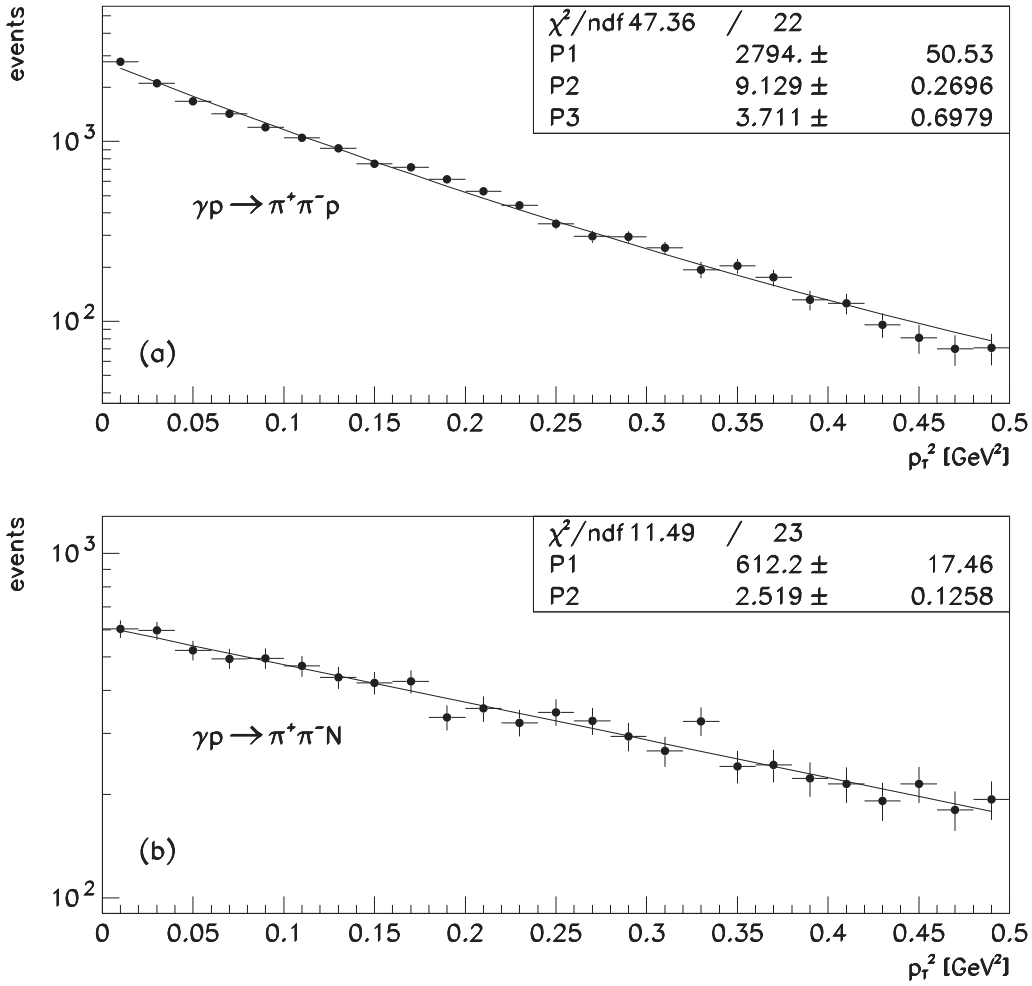

Figure 7.2: *Tagging efficiency corrected p_T^2 distributions of elastic (plot a) and proton-dissociative (plot b) $\pi^+\pi^-$ events in the ρ^0 mass region. Elastic events were selected with PRT1 and FCAL veto and the remaining contamination by proton-dissociative events was corrected according to Eq. 7.3. The superimposed fits are of the form $N_{\pi\pi}e^{-bp_T^2+cp_T^{2\,4}}$ with parameters $P_1 = N_{\pi\pi}$, $P_2 = b$, and $P_3 = c$.*

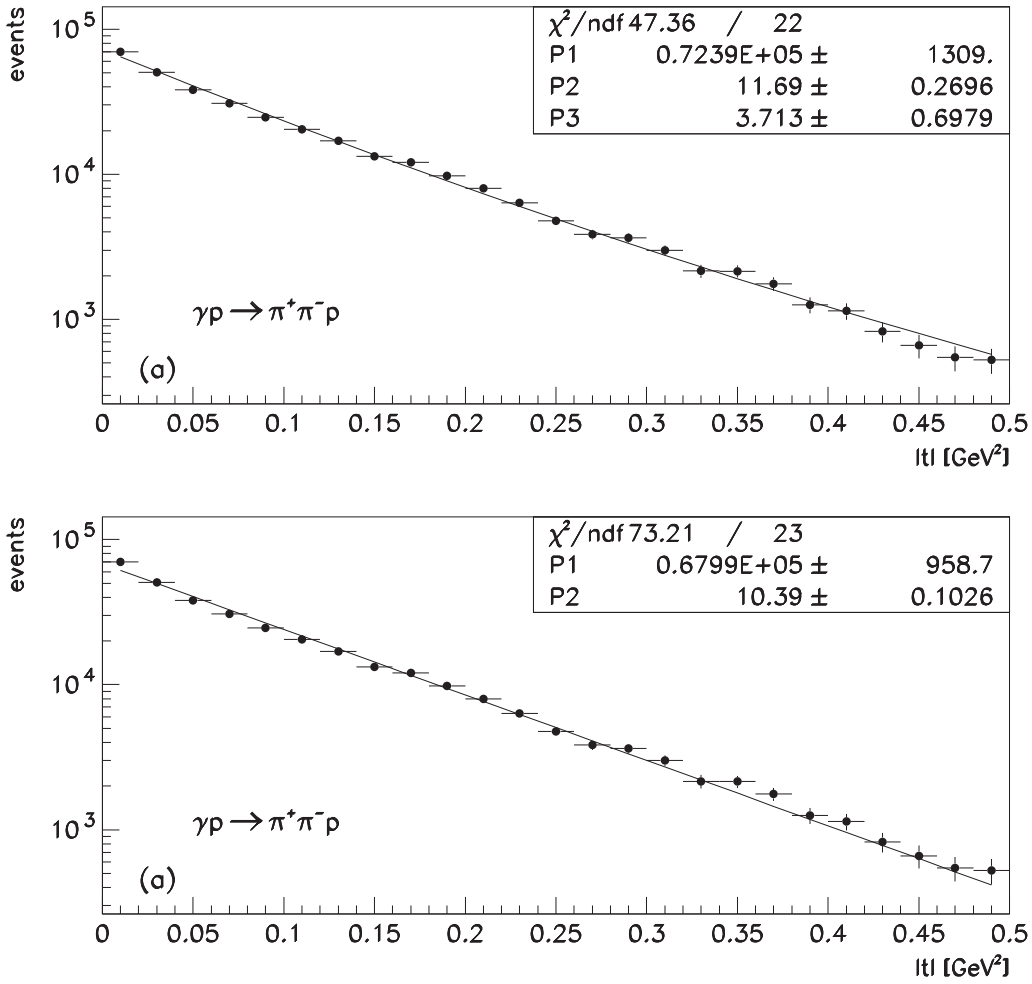

Figure 7.3: *Tagging efficiency and acceptance corrected $|t|$ distribution of the elastic reaction $\gamma p \rightarrow \rho^0 p$. In plot (a) the solid line is a fit of the form $N_{\pi\pi} e^{-b|t|+ct^2}$ with parameters $P_1 = N_{\pi\pi}$, $P_2 = b$, and $P_3 = c$. Plot (b) shows the same data points with a superimposed exponential fit $N_{\pi\pi} e^{-b|t|}$. The elastic events were selected with PRT1 and FCAL veto and the measured number of events was corrected according to Eq. 7.3.*

7.3 Proton-Dissociative $|t|$ Distribution

In this section events of type $\gamma p \to \rho^0 N$ are analyzed. The range of masses M_N of proton-dissociative events is studied with Monte Carlo events generated with EPSOFT in the range $|t| < 0.5$ GeV^2, $75 < W < 105$ GeV and $0.55 < m_{\pi^+\pi^-} < 1.0$ GeV. At the generator level a cross section of the form $d\sigma/dM_N^2 \propto 1/M_N^n$ was assumed with an exponent $n = 2.0$ as measured in [43]. Fig. 7.4 shows the generated M_N distribution and the effect of the selection cuts. Using only an FCAL tag most of the events have masses $M_N \gtrsim 5$ GeV. Using the combination PRT1 .or. FCAL to tag proton-dissociative events, the measurement can be significantly improved; proton-dissociative events down to masses of about $M_N \gtrsim 1.5$ GeV can be detected. The generated events have a mean $W \approx 90$ GeV and M_N masses up to 27 GeV. This limits the cross section to values of $M_N^2/W^2 \leq 0.09$. The ρ^0 event selection cuts limit M_N to values $\lesssim 25$ GeV.

The uncorrected $|t|$ distributions of proton-dissociative events selected by requiring a tag in PRT1 or energy deposition in FCAL is shown in plot (b) of Fig. 7.1. The data points can be fitted with a single exponential function with slope $b_i = 2.6 \pm 0.1$ GeV^{-2}. The $|t|$ distribution corrected for tagging efficiency and acceptance are shown in Fig. 7.5 with a superimposed fit in the range $0.025 < |t| < 0.5$ GeV^2 to allow for the minimum value of $|t|$, $|t|_{\min} \approx 0.01$ GeV^2. The fit is consistent with $c = 0$, and with $c = 0$ fixed, the fit yields

$$b_i = 4.3 \pm 0.2 \text{ (stat.)} \, ^{+0.7}_{-0.6} \text{ (syst.) GeV}^{-2}. \tag{7.4}$$

This value has to be compared with results from a previous analysis done in the range $0.025 < |t| < 0.5$ GeV^2: $b_i' = 5.8 \pm 0.3$ (stat.) ± 0.5 (syst.) GeV^{-2} [47].

Fig. 7.6 shows the number of proton-dissociative ρ^0 events selected versus $|t|$ in the range $0 < |t| < 2$ GeV^2 corrected for tagging efficiency and acceptance. A double exponential fit function of the form $N(|t|) = N_0 \exp(-b_i|t| + c_i t^2)$ is indicated by a superimposed solid line with the fit parameters

$$\begin{aligned} b_i &= 4.7 \pm 0.2 \text{ GeV}^{-2} \quad \text{and} \\ c_i &= 1.0 \pm 0.1 \text{ GeV}^{-4}. \end{aligned} \tag{7.5}$$

An exponential fit in the range $0.4 < |t| < 1.2$ GeV^2 yields $b_i = 2.6 \pm 0.2$ GeV^{-2}, which is consistent with the result found in [48], namely 2.4 ± 0.2 (stat.) $^{+0.2}_{-0.1}$ (syst.) ± 0.3 GeV^{-2} (mod.). Here (mod.) represents the uncertainty due to the modeling of the proton-dissociation in the EPSOFT Monte Carlo.

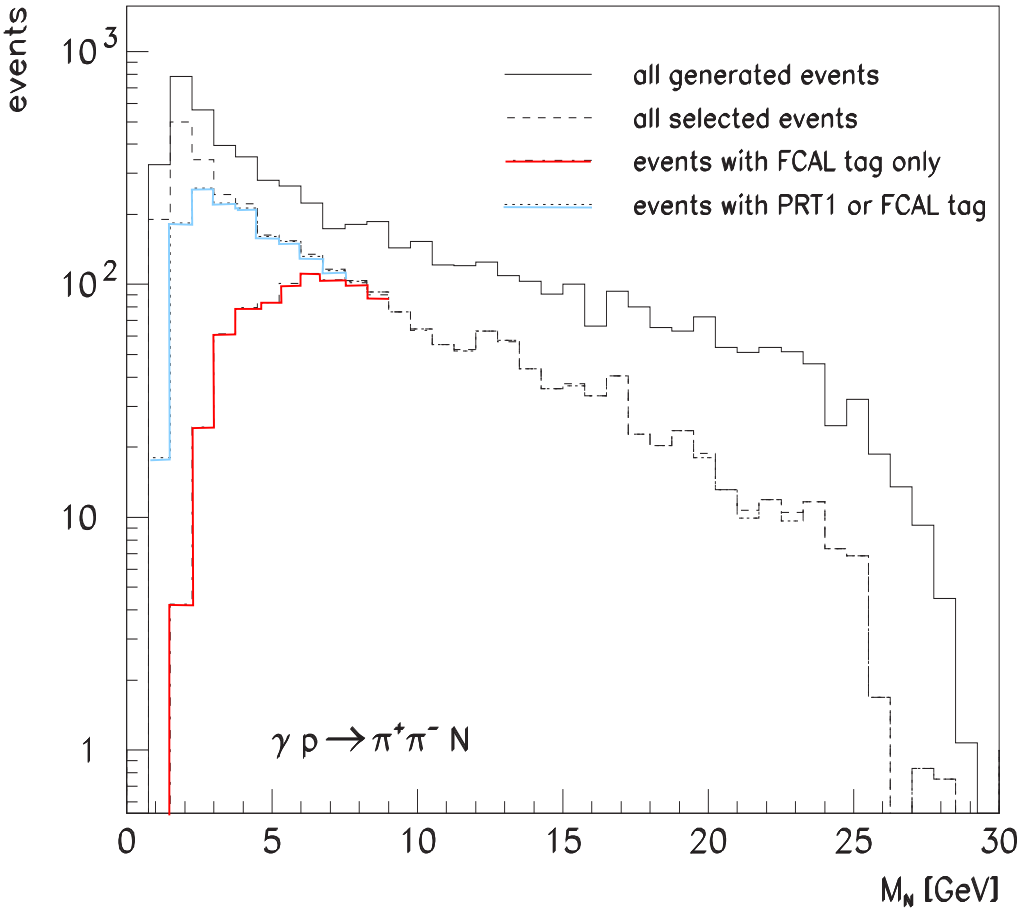

Figure 7.4: *M_N distributions of proton-dissociative Monte Carlo events. The solid curve shows the generated M_N mass distribution. The dashed curve shows the events remaining after the selection cuts described in Sec. 4.1. The dash-dotted and dotted histograms show the M_N distributions for the events remaining after requiring an FCAL tag and a tag in PRT1 .or. FCAL, respectively.*

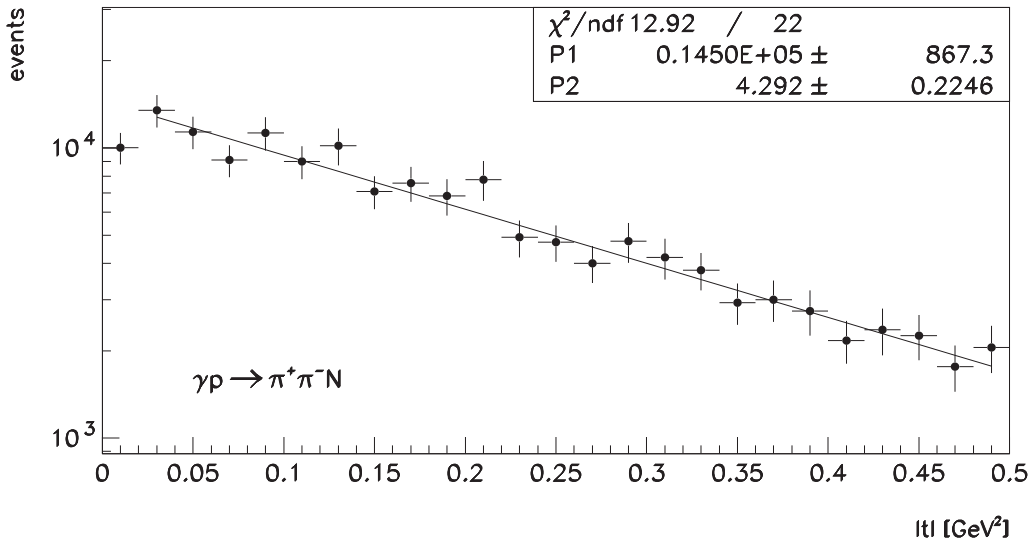

Figure 7.5: *Tagging efficiency and acceptance corrected $|t|$ distribution of proton-dissociative events in the range $0 < |t| < 0.5\ GeV^2$.*

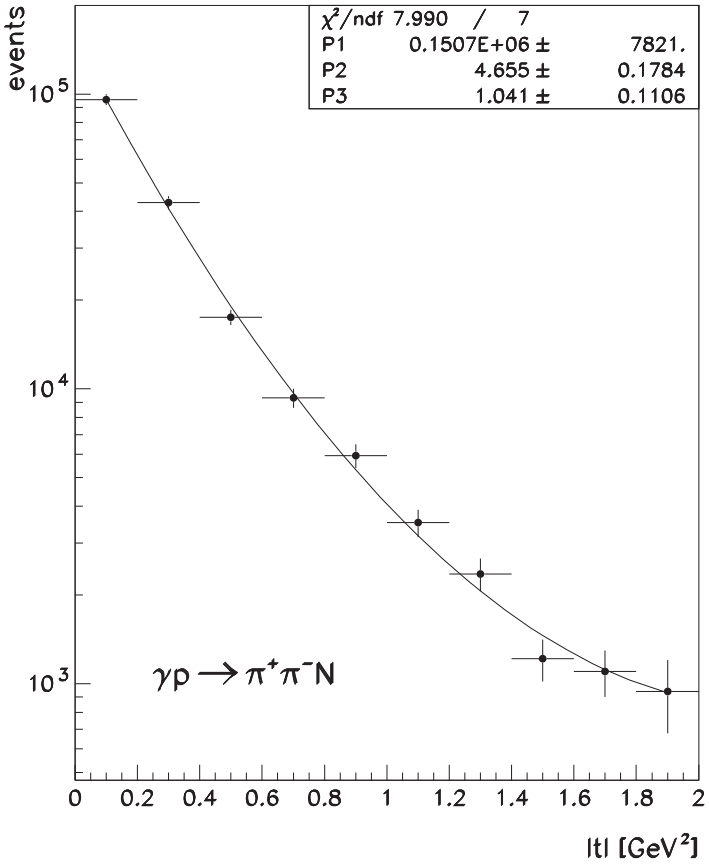

Figure 7.6: *Acceptance and tagging efficiency corrected number of proton-dissociative ρ^0 events in the range $0 < |t| < 2\ GeV^2$.*

7.4 Proton-Dissociative Cross Section

The ratio of the elastic to the proton-dissociative cross section for $|t| < 0.5$ GeV^2 is shown in Fig. 7.7. A fit of the form

$$\frac{d\sigma/dt|_{\rm el}}{d\sigma/dt|_{\rm pr.diss}} = Ae^{-\Delta b'|t|} \tag{7.6}$$

in the range $0.025 \leq |t| \leq 0.5$ GeV^2 yields $A = 4.1 \pm 0.3\,(\text{stat.})\,^{+0.3}_{-0.9}\,(\text{syst.})$ and $\Delta b' = 5.6 \pm 0.3\,(\text{stat.})\,^{+0.4}_{-0.2}\,(\text{syst.})\,\text{GeV}^{-2}$.

This agrees with the acceptance corrected value for the slope difference from Figs. 7.3 and 7.5 which is $\Delta b = 6.1 \pm 0.2$ (stat.) $^{+0.2}_{-0.3}$ (syst.) GeV^{-2}. To compare this result with Δb from Chap. 5 the values of Δb in Tab. 5.1 have to be acceptance corrected and one finds: $\Delta b_{\rm acc} = 5.9 \pm 0.5$ (stat.) ± 0.5 (syst.) GeV^{-2}.

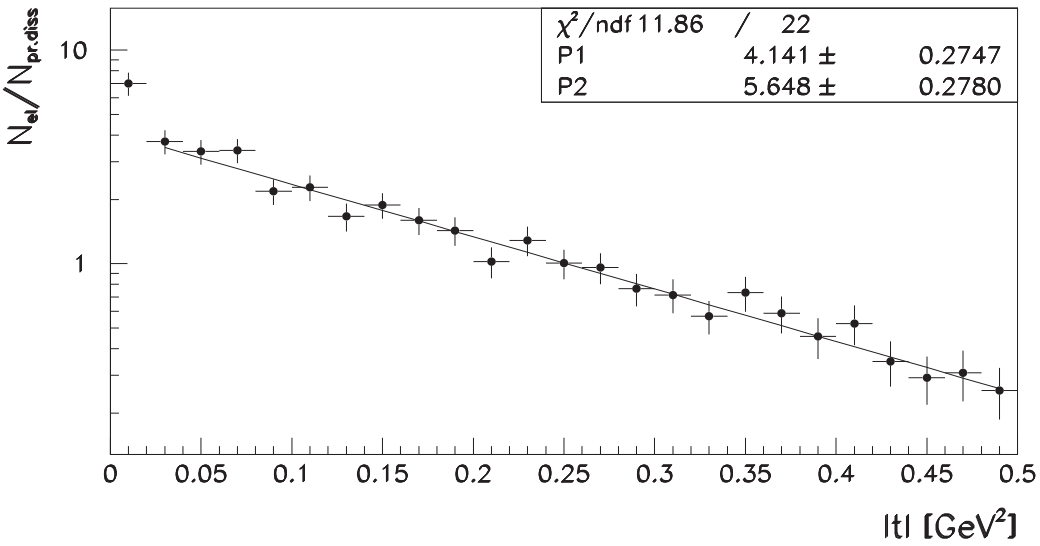

Figure 7.7: *Ratio of elastic to proton-dissociative cross sections in the range* $0 < |t| < 0.5$ *GeV*^{2}.

The ratio of the elastic to the proton-dissociative cross section in the range $0 < |t| < 0.5$ GeV^2 can now be computed from the cross sections in Sec. 7.2 and 7.3 (Figs 7.3

and 7.6). The result is

$$R_0 = \frac{\int_0^{0.5} d\sigma/dt|_{\text{el}}\, dt}{\int_0^{0.5} d\sigma/dt|_{\text{pr.diss}}\, dt} \tag{7.7}$$

$$= 2.2 \pm 0.1\ (\text{stat.})\ ^{+0.4}_{-0.1}\ (\text{syst.}) \tag{7.8}$$

This result is in agreement with the value $R_{\text{el/p-diss}} = 2.0 \pm 0.2\ (\text{stat.}) \pm 0.7\ (\text{syst.})$ given in [47].

The contribution of proton-dissociative events $C_{\text{p diss}}$ in the selected elastic candidates in the range $0 < |t| < 0.5\ \text{GeV}^2$ can be calculated as follows:

$$C_{\text{p diss}} = \frac{N_{\text{i}}(1-\varepsilon_i)}{N_{\text{e}} + N_{\text{i}}(1-\varepsilon_i)} = \frac{1-\varepsilon_i}{R_0 + 1 - \varepsilon_i}, \tag{7.9}$$

where ε_i denotes the tagging efficiency of the detector used to tag inelastic events. Using only FCAL with efficiency $\varepsilon_i^{\text{FCAL}} = 0.40 \pm 0.04$ yields $C_{\text{p diss}} = (21 \pm 2)\,\%$, which agrees with an earlier result: $(20.3^{+6.3}_{-5.1})\%$ [43]. For the combination PRT1 .or. FCAL with efficiency $\varepsilon_i^{\text{PRT1 .or. FCAL}} = 0.61 \pm 0.06$ we find a contribution of proton-dissociative events to the elastic sample of $14^{+4}_{-6}\,\%$.

The ratio of the total cross section of the elastic and the proton-dissociative reaction can be obtained from integrating the differential cross section of the elastic reaction (Fig. 7.3) and the proton-dissociative reaction shown in Fig. 7.6. The extrapolation to larger $|t|$-values (greater than 0.5 GeV^2 in the case of the elastic and greater than 2.0 GeV^2 in the case of the proton-dissociative reaction) was made and results in a small correction, yielding

$$\frac{\sigma(\gamma p \to \rho^0 p)}{\sigma(\gamma p \to \rho^0 N)} = 2.0 \pm 0.1\,(\text{stat.})^{+0.4}_{-0.1}\,(\text{syst.}) \tag{7.10}$$

From this ratio the total proton-dissociation cross section can be obtained, using the published values of the elastic reaction. At $W = 71.7$ GeV and $|t| < 0.5\ \text{GeV}^2$ the total cross section $11.2 \pm 0.1\ (\text{stat.})\ ^{+1.1}_{-1.2}\ (\text{syst.})\ \mu\text{b}$ was obtained for the elastic reaction $\gamma p \to \rho^0 p$.[44] Extrapolating this value to $W = 90$ GeV and to larger values of $|t|$ yields

$$\sigma(\gamma p \to \rho^0 p) = 11.8 \pm 0.1\,(\text{stat.})\ ^{+1.1}_{-1.2}\ (\text{syst.})\ \mu\text{b}, \tag{7.11}$$

and from this value the cross section

$$\sigma(\gamma p \to \rho^0 N) = 6.0 \pm 0.4\,(\text{stat.})\ ^{+0.7}_{-1.3}\ (\text{syst.})\ \mu\text{b} \tag{7.12}$$

at $W = 90$ GeV and for $M_N^2/W^2 < 0.09$ is obtained.

7.5 The Invariant Mass Distribution

Using the elastic Monte Carlo data sample the $m_{\pi^+\pi^-}$ acceptance was calculated in the range $70 < W < 105$ GeV. The resulting corrected mass distribution in the range $0.4 < m_{\pi^+\pi^-} < 1.2$ GeV is shown in Fig 7.8.

A method often used to describe resonances is fitting a relativistic Breit-Wigner function to the experimental data:

$$f^{BW}(m_{\pi^+\pi^-}) = \frac{m_{\pi^+\pi^-} m_\rho \Gamma_\rho}{(m^2_{\pi^+\pi^-} - m^2_\rho)^2 + m^2_\rho \Gamma^2_\rho} \tag{7.13}$$

with the nominal ρ^0 mass m_ρ. Γ_ρ is the momentum-dependent width [26]

$$\Gamma_\rho = \Gamma_0 \left(\frac{q^*}{q_0}\right)^3 \frac{m_\rho}{m_{\pi^+\pi^-}} \tag{7.14}$$

with the width Γ_0 of the ρ^0. q^* is the pion momentum in the $\pi^+\pi^-$ system rest frame:

$$q^*(m_{\pi^+\pi^-}, m_\pi) = \sqrt{\frac{m^2_{\pi^+\pi^-}}{4} - m^2_\pi} \tag{7.15}$$

and q_0 is the value of q at the nominal ρ^0 mass m_ρ.

Compared to a Breit-Wigner distribution the mass distribution in Fig. 7.8 is slightly shifted and skewed towards lower values. In the Söding model [36] the $\pi^+\pi^-$ photoproduction amplitude is a compositon of a Breit-Wigner shaped ρ^0 mass spectrum and a non-resonant Drell-type background, consisting of events where the incoming photon γ fluctuates into a $\pi^+\pi^-$ pair without forming a ρ^0 resonance [35]. Interference of both contributions results in the observed asymmetry of the invariant $\pi^+\pi^-$ mass distribution (see also [37]).

In another approach pointed out by Ross and Stodolsky the interference from the non-resonant background reaction is ingnored, and instead a mass dependence of the ρ^0 production amplitude is assumed [34]. They introduced a factor of $(m_\rho/m_{\pi^+\pi^-})^{n_{RS}}$ and found a value of $n_{RS} = 4$, which was used in other analyses (see e. g. [42]). The fit in Fig. 7.8 is done according to

$$\frac{d\sigma}{dm_{\pi^+\pi^-}} = A f^{BW}(m_{\pi^+\pi^-}) \left(\frac{m_\rho}{m_{\pi^+\pi^-}}\right)^{n_{RS}} \tag{7.16}$$

where A is a normalization factor and n_{RS} is a free parameter.

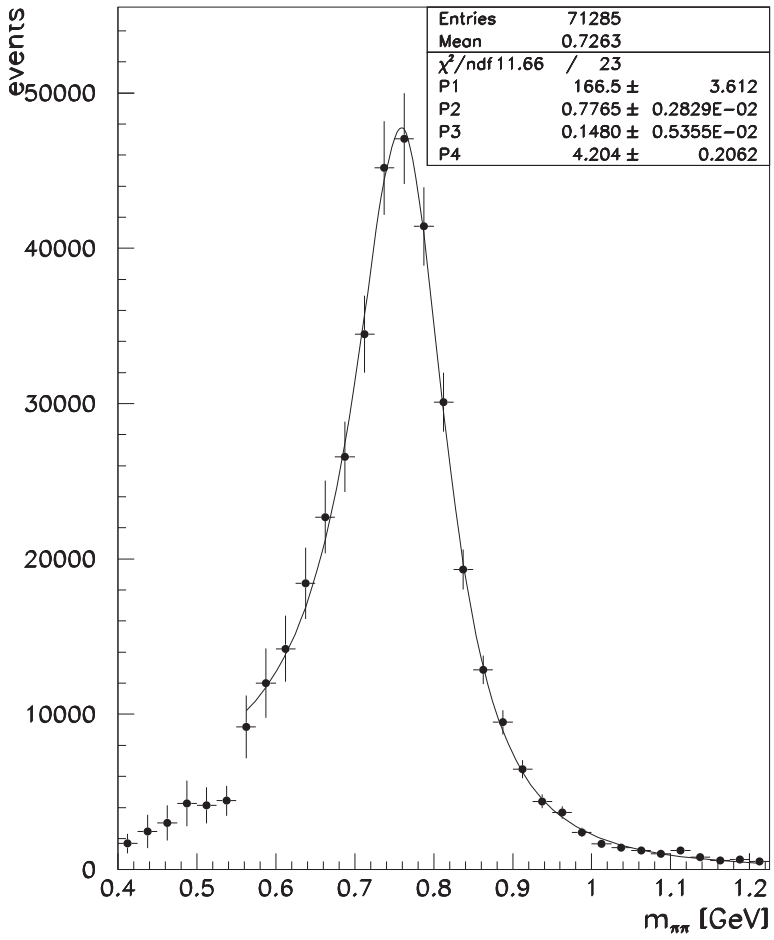

Figure 7.8: *Invariant $\pi^+\pi^-$ mass distribution of elastic events $\gamma p \to \rho^0 p$ in the range $75 < W < 105$ GeV. The solid line is a fit of a relativistic Breit-Wigner function with a Ross-Stodolsky factor (Eq. 7.16).*

For the mass m_ρ and the width Γ_0 we find

$$\begin{aligned} m_\rho &= 777 \pm 3 \text{ MeV} \\ \Gamma_0 &= 148 \pm 5 \text{ MeV} \end{aligned}$$

and a value of $n_{RS} = 4.2 \pm 0.2$. The fit is very good with $\chi^2/ndf = 0.51$, and the results for m_ρ and Γ_0 are in good agreement with the values given by the Particle Data Group [20].

Chapter 8

Test of Factorization

In this chapter the results on elastic and proton-dissociative ρ photoproduction will be compared with analogous results of hadron-hadron experiments at very high energies, where pure pomeron exchange should give a good phenomenological description of the processes. Such measurements have been made at the ISR for pp collisions and at the Fermilab and CERN $p\bar{p}$ colliders for proton–antiproton collisions. An introduction into the phenomenology of diffractive processes can be found in [3, 1]. A short summary is given in sections 8.1.1 and 8.1.2.

8.1 Phenomenology of Diffractive Processes

8.1.1 Single Diffraction Process

A generic diagram of single diffractive (SD) processes $hp \to hN$ is shown in Fig. 8.1; here h is either a proton, antiproton or a vector meson coupled to an incoming photon. The exchanged 'particle' is a phenomenological pomeron. The target proton p dissociates into an excited state N with mass M_N.

The differential cross section is approximately given by

$$\frac{d^2\sigma_{SD}}{d|t|\ dM_N^2} \sim \frac{1}{M_N^2} e^{-b_{\mathrm{SD}}(s,M_N^2)|t|} \left(\frac{s}{s_0}\right)^{\varepsilon_{\mathrm{SD}}}, \tag{8.1}$$

where s is the center of mass energy squared. Here, $\varepsilon_{\mathrm{SD}} \approx 0.1$ [5, 7], and the M_N^2–dependence holds to a good approximation (see however [5, 7]). The diffractive slope

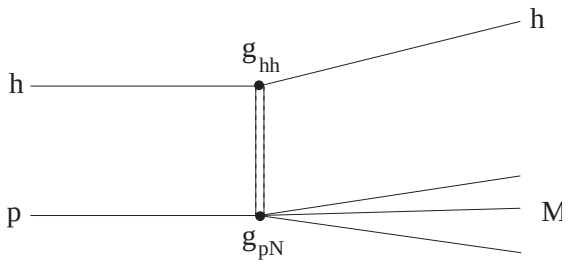

Figure 8.1: *Generic single diffraction diagram of the process $hp \to pN$, where h is a proton, antiproton or vector meson.*

b_{SD} has a weak dependence on s and M_N^2:

$$b_{\mathrm{SD}} = b_0 + 2\alpha' \ln \frac{s}{M_N^2} \ , \ \ \alpha' = 0.25\,\mathrm{GeV}^{-2}. \tag{8.2}$$

There is a minimum squared momentum transfer given by

$$|t|_{min} = M_p^2 (M_N^2 - M_p^2)^2 / s^2 \tag{8.3}$$

for proton/antiproton reactions on the proton and

$$\begin{aligned} |t|_{min} \ &= \ \frac{(m_\rho^2 + Q^2)(M_N^2 - M_p^2)}{s} \\ &+ \frac{(M_N^2 - M_p^2 + Q^2 + m_\rho^2)\left[M_p^2(Q^2 + m_\rho^2) - Q^2(M_N^2 - M_p^2)\right]}{s^2} \end{aligned} \tag{8.4}$$

for photoproduction in the general case of a photon with virtuality Q^2.

8.1.2 Elastic Scattering

Fig. 8.2 shows the generic diagram of elastic diffractive scattering $hp \to hp$. As in the case of single diffraction, the exchanged 'particle' is a phenomenological pomeron. The cross section $d\sigma/d|t|$ can be parameterized as follows:

$$\frac{d\sigma_e}{d|t|} \sim e^{-b_e(s)|t|} \left(\frac{s}{s_0}\right)^{\varepsilon_e}, \tag{8.5}$$

with slope parameter b_e depending on the square of the center of mass energy s like $b_e = b_{e,0} + 2\alpha' \ln(s/s_0)$.

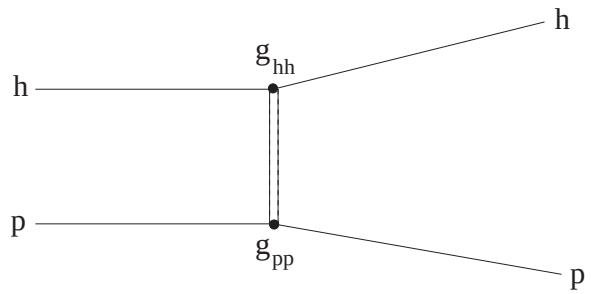

Figure 8.2: *Generic diagram of the elastic diffractive scattering process $hp \to hp$, where h is a proton, antiproton or vector meson and g_{hh} denotes the Hadron-Pomeron coupling constant.*

8.2 Factorization

The ratio $g_{\mathrm{pN}}/g_{\mathrm{pp}}$ of single diffraction to elastic scattering at very high energies can according to Figs. 8.1 and 8.2 be written as

$$\frac{\sigma_{\mathrm{SD}}(hp \to hN)}{\sigma_{\mathrm{e}}(hp \to hp)} = \left(\frac{g_{\mathrm{hh}} \cdot g_{\mathrm{pN}}}{g_{\mathrm{hh}} \cdot g_{\mathrm{pp}}}\right)^2 = C_p(s, M_N^2, t) \tag{8.6}$$

where the propagator term has cancelled and the function $C_p(s, M_N^2, t)$ depends only weakly on s and is independent of the type of incoming hadron h. Relation 8.6 has been checked for $h = \pi^{\pm}$, $K^{\pm}$ and p and $\overline{p}$ at lower energies [5]. Relation 8.6 can be integrated over M_N^2:

$$\int^{M_N^2/s} C_p(s, M_N^2, t) dM_N^2 = C_{p,i}(s, t) \tag{8.7}$$

and with $s = 0.05$ GeV^2 and the ansatz

$$\frac{d\sigma_{\mathrm{SD}}}{d|t|} = \sigma_{\mathrm{SD}} b_{\mathrm{SD}} exp(-b_{\mathrm{SD}}|t|) \tag{8.8}$$

and

$$\frac{d\sigma_e}{d|t|} = \sigma_e b_e exp(-b_e|t|) \tag{8.9}$$

we have

$$C_{p,i}(s,t) = \frac{d\sigma_{SD}/dt}{d\sigma_e/dt} = \frac{\sigma_{SD} b_{SD}}{\sigma_e b_e} exp(\Delta b|t|) = A(s) exp(\Delta b|t|) \tag{8.10}$$

with $\Delta b(s) = b_e - b_{SD}$, and

$$A(s) = \frac{\sigma_{SD} b_{SD}}{\sigma_e b_e} = \left.\frac{d\sigma_{SD}/dt}{d\sigma_e/dt}\right|_0 \quad , \tag{8.11}$$

a slowly varying function of s. Since $C_{p,i}$ is independent of the type of incoming hadron, so are $A(s)$ and Δb. The two quantities $A(s)$ and $\Delta b(s)$ offer therefore a test of factorization.

8.2.1 Test of Factorization

The results of measurements obtained at CERN and Fermilab with protons and antiprotons can be compared with ρ photoproduction and factorization for these three reactions can be checked. Fig. 8.3 summarizes the results of total cross section measurements of elastic and single diffractive reactions for protons and antiprotons described in Sec. 8.1.1 and 8.1.2.

The cross section values for single proton diffraction given in the literature refer to the sum of target and projectile diffraction; they had to be divided by 2, so that Eq. 8.10, 8.11 can be applied properly. A power law fit used to interpolate between different energies is also shown.

Fig. 8.4 shows measurements of the slopes b_{SD} and b_e for protons and antiprotons, again with power law fits superimposed.

Tab. 8.1 shows the test of factorization. The function $A(s)$ has the same value $A(s) = 0.27$ with an estimated error of 10% for protons and antiprotons. This indicates a very weak energy dependence and good agreement with factorization. For ρ photoproduction one expects the same value of $A(s)$, this is contrasted by the measured value of $0.21 \pm 0.01\,(\text{stat.})\,^{+0.02}_{-0.04}\,(\text{syst.})$.

The expected value for the slope difference $\Delta b(s)$ at the center of mass energy of ρ photoproduction has been interpolated between the proton and antiproton values, using a power law, yielding $\Delta b(s) = 5.1$ GeV^{-2} with an estimated error of 1 GeV^{-2}; the measured value 6.1 GeV^{-2} (see Sect. 7.4) for ρ^0 photoproduction is in fair agreement within the errors.

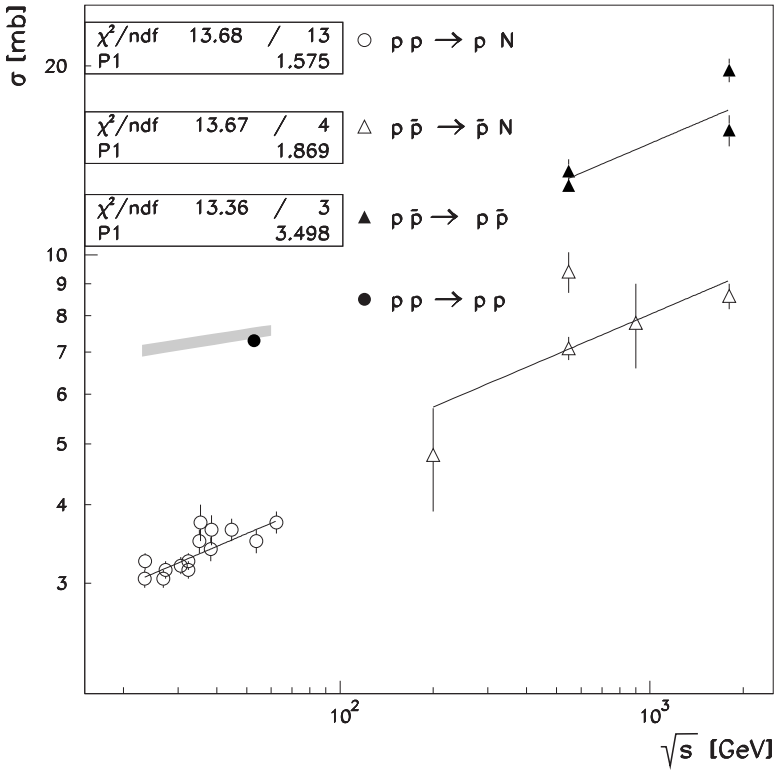

Figure 8.3: *Total cross section of elastic and single diffractive pp and $p\bar{p}$ reactions. See references [1, 2, 8, 18, 39] for the elastic and [7, 9, 38, 41] for the proton-dissociative reactions.*

pp	$p\bar{p}$	ρp		
		pred.	meas.	
30	1000	90	90	$\langle W \rangle$ [GeV]
0.45	0.53		$0.51 \pm 0.03^{+0.03}_{-0.10}$	$\sigma_{\rm SD}/\sigma_{\rm e}$
10.2	16.2		$10.4 \pm 0.1^{+1.6}_{-0.8}$	$\langle b_{\rm e} \rangle$ [GeV^{-2}]
6.1	8.2		$4.3 \pm 0.2^{+0.7}_{-0.2}$	$b_{\rm SD}$ [GeV^{-2}]
4.1	8.0	5.1	$6.1 \pm 0.2 \pm 0.2^{+0.2}_{-0.3}$	Δb [GeV^{-2}]
0.27	0.27	0.27	$0.21 \pm 0.01^{+0.02}_{-0.04}$	$A(s)$

Table 8.1: *Test of factorization*

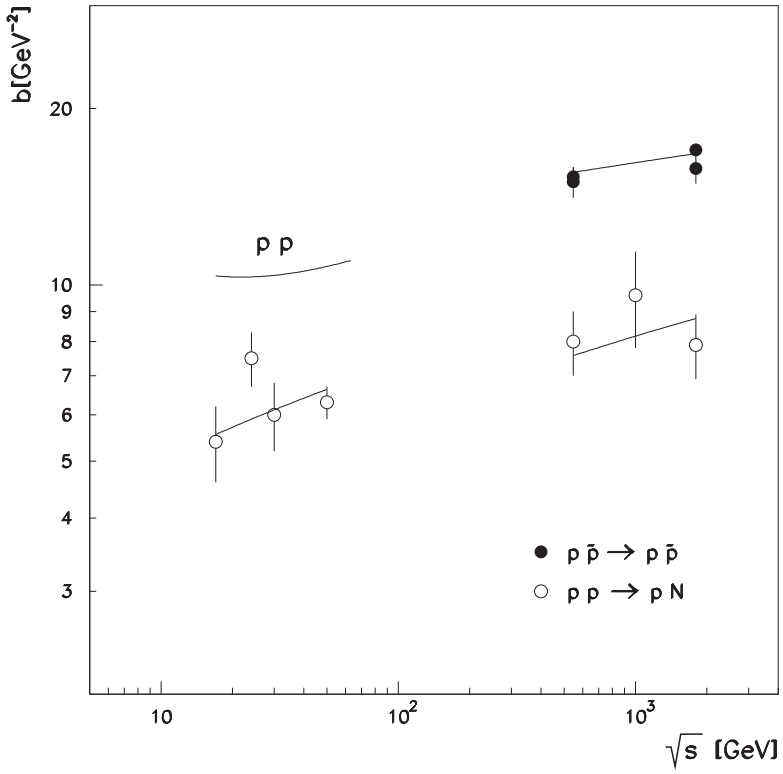

Figure 8.4: *Slopes b_{SD} and b_e for pp and $p\bar{p}$ reactions. See references [1, 8, 18, 39] for the elastic and [5, 7, 9, 10, 18, 38, 40] for the proton-dissociative reactions.*

Chapter 9

Conclusions

Elastic and proton-dissociative photoproduction of ρ^0 mesons has been studied in the reactions $\gamma p \to \rho^0 p$ and $\gamma p \to \rho^0 N$, where N is a proton-dissociative state. The average center of mass energy was 90 GeV. The proton remnant tagger, a set of scintillation counters, was designed and installed close to the HERA beam pipe to detect the proton-dissociative state N in an angular range between 6 and 26 mrad in the outgoing proton direction. With the PRT N can be identified to masses as low as $M_N \gtrsim 1.5$ GeV, which is a significant improvement of earlier measurements. The total measured range was $1.5 < M_N < 27$ GeV.

For the identification of proton-dissociative events the tagging efficiency ε of the PRT was studied using physics data. It could be shown that ε depends on square of the four-momentum transfer $|t|$. Therefore, the tagging efficiency was studied in two different t-ranges. In the range $0 < |t| < 0.6$ GeV ^{2} the combined tagging efficiency of PRT .or. FCAL was found to be $\varepsilon = 0.61 \pm 0.06$. In the t-range $|t| > 0.6$ GeV ^{2} the tagging efficiency rises with $|t|$ reaching $\varepsilon = 0.92 \pm 0.04$ $|t| = 2.0$ GeV ^{2}.

The counters were also used to improve subtraction of proton-dissociative background from elastic ρ^0 photoproduction. The results are the following:

The differential cross section of elastic ρ^0 photoproduction, if fitted to an exponential function of the form $A \exp(-b_e|t| + c_e t^2)$, where t is the square of the four-momentum transfer at the proton vertex, yields the parameters $b_e = 11.7 \pm 0.3$ (stat.) $^{+1.8}_{-0.9}$ (syst.) GeV^{-2} and $c_e = 3.7 \pm 0.7$ (stat.) $^{+2.1}_{-0.2}$ (syst.) GeV^{-4}, in the fit range $0 < |t| < 0.5$ GeV^2. A fit to the proton-dissociative cross section in the same t-range to the form $A \exp(-b_i|t|)$ yields the slope $b_i = 4.3 \pm 0.2$ (stat.)$^{+0.7}_{-0.6}$ (syst.) GeV^{-2}. The proton-dissociative cross

section has been measured in the interval $0 < |t| < 2$ GeV^2 and fitted to to an exponential function of the form $A \exp(-b_i|t| + c_i t^2)$. The result is $b_i = 4.7 \pm 0.2$ (stat.) GeV^{-2} and $c_i = 1.0 \pm 0.1$ (stat.) GeV^{-4}. The ratio of the elastic to the proton-dissociative cross section in the range $0 < |t| < 0.5$ GeV^2 is 2.2 ± 0.1 (stat.) $^{+0.4}_{-0.1}$ (syst.), and in the whole t-range this ratio is 2.0 ± 0.1 (stat.) $^{+0.4}_{-0.1}$ (syst.). Using the published elastic ρ^0 cross section of 11.2 μb at a center of mass energy of 71.7 GeV, this leads to a total cross section of the proton-dissociative reaction at 90 GeV center of mass energy of $\sigma_{\text{pdiss}} = 6.0 \pm 0.4$ (stat.) $^{+0.7}_{-1.3}$ (syst.) μb.

The data have been compared with elastic and proton-dissociative reactions of protons and antiprotons at high energies at the ISR and the proton-antiproton storage ring at CERN and at the TEVATRON at Fermilab. Factorization of diffractive reactions has been tested and a fair agreement was found.

Bibliography

[1] G. Alberi and G. Goggi,
Diffraction of Subnuclear Waves,
Phys. Rep. **74** (1981) 1

[2] N. Amos et al.,
Comparison of Small–Angle $p\overline{p}$ and pp Elastic Scattering at 52.8 GeV Center-of-Mass Energy at the CERN Intersecting Storage Rings,
Phys. Lett. **B120** (1983) 460

[3] F. Arbad, J. D. Jackson,
Factorization, Kinematic Singularities, and Conspiracies,
Phys. Rev. **176** (1968) 1796

[4] D. Aston et al.,
Photoproduction of ρ^0 and ω on Hydrogen at Photon Energies of 20 to 70 GeV,
Nucl. Phys. **B209** (1982) 56

[5] D. S. Ayres et al.,
Inelastic Diffractive Scattering at Energies of 140 to 175 GeV,
Phys. Rev. Lett. **37** (1976) 1724

[6] T. H. Bauer, R. D. Spital, D. R. Yennie, and F. M. Ripkin
The Hadronic Properties of the Photon in High Energy Interactions,
Rev. Mod. Phys. **50** (1978) 261

[7] CDF Collaboration, F. Abe et al.,
Measurement of $\overline{p}p$ Single Diffraction Dissociation at $\sqrt{546}$ and 1800 GeV,
Phys. Rev. **D50** (1994) 5535

[8] CDF Collaboration, F. Abe et al.,
Measurement of Small Angle Antiproton–Proton Elastic Scattering at $\sqrt{s} = 546$ *and 1800 GeV*,
Phys. Rev. **D50** (1994) 5518

[9] CHLM Collaboration, M. G. Albrow et al.,
Inelastic Diffractive Scattering at the CERN ISR,
Nucl. Phys. **B108** (1976) 1

[10] CHLM Collaboration, J. C. M. Armitage et al.,
Diffraction Dissociation in Proton–Proton Collisions at ISR Energies,
Nucl. Phys. **B194** (1982) 365

[11] P. D. B. Collins and A. D. Martin,
Hadron Interactions,
Graduate Student Series in Physics, Adam Hilder Ltd, Bristol

[12] J. R. Cudell et al., preprint hep-ph 9601336 (1996)

[13] F. T. Dao et al.,
pp Interactions at 303 GeV/c: Analysis of Diffraction Excitation in the Interaction $pp \to pX$,
Phys. Lett. **B45** (1973) 399

[14] K. Desler and U. Schneekloth,
The Hardware of the Proton Remnant Tagger (PRT) in 1994,
ZEUS Note 95–061 (May 1995)

[15] K. Desler,
How to use the Proton Remnant Tagger (PRT),
URL http://www.desy.de/∼desler/PRT.html

[16] K. Desler,
How to use the Proton Remnant Tagger in 1996,
ZEUS Note 97–084 (October 1997)

[17] A. Donnachie and P. V. Landshoff, Phys. Lett. **B185** (1987) 403;
A. Donnachie and P. V. Landshoff, Nucl. Phys. **B311** (1989) 509;
P. V. Landshoff, Nucl. Phys. B (Proc. Suppl.) **18C** (1990) 211.

[18] E811 Collaboration, C. Avila et al.,
A Measurement of the Proton-Antiproton Total Cross Section at $\sqrt{s} = 1.8$ *TeV*,
FERMILAB-Pub-98/313-E

[19] K. Goulianos,
Diffractive Interactions of Hadrons at High Energies,
Phys. Rep. **101** (1983) 169

[20] D. E. Groom et al.,
Review of Particle Physics
Europ. Phys. J. **C15** (2000) 1

[21] H1 Collaboration, S. Aid et al.,
Measurement of the Total Photon Proton Cross section and its Decomposition at 200 GeV Centre of Mass Energy,
Z. Phys. **C69** (1995) 27

[22] H1 Collaboration, T. Ahmed et al.,
Elastic Photoproduction of ρ^0 *Mesons at HERA*,
DESY 95–251,
Nucl. Phys. **B463** (1996) 3

[23] H1 Collaboration, C. Adloff et al.,
Diffractive Dissociation in Photoproduction at HERA,
Z. Phys. **C74** (1997) 221

[24] F. Halzen and A. D. Martin,
Quarks and Leptons: An Introductory Course in Modern Particle Physics,
John Willey and Sons, Inc.

[25] U. Holm ed.,
The ZEUS Detector,
Status Report 1993, DESY 1993

[26] J. D. Jackson,
Remarks on the Phenomenological Analysis of Resonances,
Il Nuovo Cimento **34** (1964) 1644

[27] P. Joos et al.,
Rho Production by Virtual Photons,
Nucl. Phys. **B113** (1976) 53

[28] M. Kasprzak,
Inclusive Properties of Diffractive and Non-Diffractive Properties at HERA,
DESY F35D–96–16, Warsaw University, PhD thesis, 1996

[29] L. Köpke,
The ZEUS Primer,
ZEUS Note 93–006

[30] K. Klimek,
URL http://www-zeus.desy.de/~kklimek/ZEUS_ONLY/acc/1996.html

[31] G. Marchesini et al,
HERWIG 5.1-a Monte Carlo Generator for Simulating Hadron Emission Reactions with Interfering Gluons,
Comp. Phys. Comm. **67** (1992) 465

[32] J. Park et al.,
The Reaction $\gamma p \to \rho^0 p$ at 5.5 to 18 GeV,
Nucl. Phys. **B36** (1972) 404

[33] K. Piotrzkowski,
Diffractive Photoproduction of Vector Mesons at High $|t|$
Zeus Note 97–016 (March 1997)

[34] M. Ross and L. Stodolsky,
Photon Dissociation Model for Vector-Meson Photoproduction,
Phys. Rev. **149** (1966) 1172

[35] M. G. Ryskin and Yu. M. Shabelski,
Role of the Non-Resonant Background in the ρ^0-Meson Diffractive Electro- and Photoproduction,
hep-ph/9701407

[36] P. Söding,
On the Apparent Shift of the Rho Meson Mass in Photoproduction,
Phys. Lett. **19** (1966) 702

[37] R. Spital and D. R. Yennie,
ρ^0 Shape in Photoproduction,
Phys. Rev. **D9** (1973) 126

[38] UA4 Collaboration, D. Bernard et al.,
The Cross Section of Diffraction Dissociation at the CERN SPS Collider,
Phys. Lett. **B186** (1987) 227

[39] UA4 Collaboration, M. Bozzo et al.,
Low Momentum Transfer Elastic Scattering at the CERN Proton–Antiproton Collider,
Phys. Lett. **B147** (1984) 385

[40] UA4 Collaboration, M. Bozzo et al.,
Measurement of the Proton–Antiproton Total and Elastic Cross Sections at the CERN SPS Collider
Phys. Lett. **B147** (1984) 392

[41] UA5 Collaboration, R. E. Ansorge et al.,
Diffraction Dissociation at the CERN Pulsed $p\overline{p}$ Collider at c. m. Energies of 900 and 200 GeV,
Z. Phys. **C33** (1986) 175

[42] K. Wacker,
Elektroerzeugung der Endzustände $\pi^-\Delta^{++}$, $\pi^+\Delta^0$ und $p\pi^+\pi^-$,
DESY F1–76/04 (1976)

[43] D. Westphal,
Measurement of Elastic ρ^0 Photoproduction at HERA,
Hamburg University, PhD thesis, 1997

[44] ZEUS Collaboration, M. Derrick et al.,
Measurement of Elastic ρ^0 Photoproduction at HERA,
DESY 95–143 (July 1995),
Z. Phys. **C69** (1995) 39-54

[45] ZEUS Collaboration, M. Derrick et al.,
Measurement of Elastic ϕ Photoproduction at HERA,

DESY 96–002 (January 1996),
Phys. Lett. **B377** (1996) 259-272

[46] ZEUS Collaboration, M. Derrick et al.,
Measurement of Elastic ω Photoproduction at HERA,
DESY 96–159 (August 1996),
Z. Phys. **C73** (1996) 73-84

[47] ZEUS Collaboration, J. Breitweg et al.,
Elastic and Proton-Dissociative ρ^0 Photoproduction at HERA,
DESY 97–237,
Europ. Phys. J. **C2** (1998) 2, 247

[48] ZEUS Collaboration, J. Breitweg et al.,
Measurement of Diffractive Photoproduction of Vector Mesons at Large Momentum Transfer at HERA,
DESY 99–160,
Europ. Phys. J. **C14** (2000) 2, 213

[49] ZEUS Collaboration, J. Breitweg et al.,
Measurement of the t Distribution in Diffractive Photoproduction at HERA,
DESY 97–238,
Europ. Phys. J. **C2** (1998) 2, 237

[50] ZEUS Collaboration, M. Derrick et al.,
Measurement of Total and Partial Photon Proton Cross Sections at 180 GeV Center of Mass Energy,
DESY 94–032,
Z. Phys. **C63** (1994) 391

Acknowledgments

I would like to thank all friends and colleagues at DESY who helped shaping this Ph.D. thesis:

Special thanks to Prof. Dr. Erich Lohrmann for his never-ending guidance and support. I would also like to thank him that he gave me the opportunity to work for the ZEUS collaboration.

I want to say thank you to Prof. Dr. Robert Klanner for his valuable advice and support throughout the last couple of years.

Thanks to Uwe Schneekloth who introduced me into the technical aspects of the ZEUS experiment and who let me take over responsibility for the Proton Remnant Tagger soon after I started as a graduate student. Also Burkhard Burrow was always very helpful whenever his expertise or help in general was needed.

Also to Dirk Westphal who helped getting my analysis started. I learnt a lot from his experience.

I am particularly grateful for the kind support of Dieter Notz. The discussions we had always turned out to be very valuable.

Thanks to Tancredi Carli, Ulli Fricke, Frank Göbel, and Stefan Stonjek for very useful discussions that led to the conclusion of this thesis.

Special thanks to Michele Arneodo for carefully reading the manuscript and the useful suggestions that he made.

Also to Mathias Vogt who was always available to listen when all kinds of problems needed to be discussed. Special thanks to Gudrun Hiller for useful discussions of various subjects.

I would like to thank Don and Helen Edwards for their friendship and kind support and dreaming up ideas in which direction to head next.

Special thanks to my parents for their continuous support.

And last, but by no means least, love and thanks to Gina, who never gave up encouraging me to go through this all the way.